NORTHWESTERN UNIVERSITY

Self-Assembly of Organic Semiconductors and their Mineralization into Hybrid Nanostructures

A DISSERTATION

SUBMITTED TO THE GRADUATE SCHOOL
IN PARTIAL FULFILLMENT OF THE REQUIREMENTS

for the degree

DOCTOR OF PHILOSOPHY

Field of Materials Science and Engineering

By

Marina Sofos

EVANSTON, ILLINOIS

DECEMBER 2007

ABSTRACT

Self-Assembly and Mineralization of Hybrid Nanostructures with Organic Semiconductors

Marina Sofos

This dissertation demonstrates how self-assembly can direct nanoscale ordering and optimize electronic properties of organic semiconductors, as well as organic-inorganic hybrids. In excitonic solar cells, controlling the ordering and interfaces between electron-transporting (n-type) and hole-transporting (p-type) domains is crucial. In addressing this challenge, hybrid nanostructures were designed by mineralization of an inorganic templated with amphiphilic aromatic oligomers using three strategies. In the first, non-ionic amphiphiles were studied with oligo(phenylene vinylene) (OPV) or oligothiophene asymmetrically terminated with a hydrophobic alkyl and a hydrophilic poly(ethylene glycol) (PEG). In polar solvents above 30 wt.% concentration, these amphiphiles self-organized into bilayer, lyotropic liquid crystals (LC). Enhanced photoluminescence was observed in the LC compared to the isotropic state. As shown by temperature-dependent X-ray scattering, intra-layer isolation of the chromophores appeared due to the structural configuration of the PEG. Although water trapped in the PEG hindered ZnO crystallization within the LC, the organic ordering demonstrated crucial control over molecular order and aggregation. In the next approach, electrostatic interactions were exploited by evaporation-induced self-assembly synthesis of silica using cationic bolaamphiphiles consisting of OPV or oligothiophene symmetrically terminated with hydrophilic quaternary ammoniums. Grazing-incidence X-ray scattering indicated the formation of two-dimensional hexagonally-packed cylindrical micelles of the organic molecules coated by silica. Specular X-ray reflectivity further demonstrated that long-range periodicity along the surface normal could

be achieved within a molar ratio range of silica precursor to amphiphiles. X-ray characterization of the uncharged organic analogues showed that screening of the doubly charged amphiphiles by mineralization was necessary for long-range order. In the final approach, ZnO was electrochemically deposited in the presence of anionic amphiphiles containing pyrene or oligothiophene. Electron microscopy and X-ray scattering revealed the formation of alternating p- and n-type lamellae. X-ray absorption spectroscopy identified the inorganic phase as $Zn(OH)_2$; annealing to 150 °C was necessary for conversion to ZnO. The presence of the aromatic was essential for thermal stabilization of the nanostructure because the overall ordering collapsed upon conversion with non-conjugated amphiphiles from the literature. The rigid aromatics can be chemically modified, are electronically active, and as shown here, vital to overall ordering and thermal stability of these hybrids.

Thesis Advisor: Prof. Samuel I. Stupp

For my family

ACKNOWLEDGEMENTS

I would first like to thank my advisor, Prof. Samuel Stupp, for his support throughout my graduate school career, and for encouraging and challenging me to explore and perform research that I never imagined. I also thank my committee members, Prof. Lincoln Lauhon, Prof. Ken Shull, and Prof. Michael Wasielewski, for their time and help in serving on my thesis committee.

I am extremely grateful to the experimental and intellectual contributions in this thesis of four close and talented collaborators, Joshua Goldberger, James Hulvat, David Stone, and Keisuke Tajima.

In addition, I would like to thank all my colleagues in the Stupp Group, both past and present, for their support and friendship both in and out of the lab. In particular, I have been fortunate to have overlapped with Mike Arnold, Lesley Chow, Nathan Fry, Megan Greenfield, Mustafa Guler, Lorraine Hsu, Albert Hung, Jennifer Klare, Chung-Yan Koh, Liang-shi Li, Ben Messmore, Liam Palmer, Eugene "Tommy" Pashuck, Kanya Ranjagam, Erik Spoerke, Eli Sone, Stephen Soukasene, Hannah Storrie, and Weiwen Tsai. Sharon Jacknow always provided her assistance and support on all administrative matters.

Prof. Michael Bedzyk, as well as members of his group, Dipak Goswami, John Okasinski, Hua Jin, and Leiming Li, for teaching me much of the X-ray techniques and skills that I used in my graduate work. In addition, the staff at the DND-CAT at APS for their assistance in experimental set-up and technical support on the synchrotron X-ray experiments that I performed there, in particular, Dr. Denis Keane on the GIXS and XRR measurements, and Dr. Qing Ma on the XAS measurements. I would further like to thank Jerry Carsello of the Northwestern X-ray Facility for his assistance.

To my friends in the Materials Science department and elsewhere, for their company and encouragement during these past few years. Finally, to my family, for their everlasting love and support.

LIST OF ABBREVIATIONS

2D	two dimensional
3T-CA	terthiophene carboxylic acid
5T-DCA	dicarboxylic acid 3-methyl quinquethiophene
APS	Advanced Photon Source
a.u.	arbitrary units
CCD	charge-couple device
CMC	critical micelle concentration
CTAB	cetyltrimethylammonium bromide
CV	cyclic voltammetry
DMAP	4-dimethylaminopyridine
DMF	dimethylformamide
DMSO	dimethyl sulfoxide
DSC	differential scanning calorimetry
ED	electron diffraction
EDC	ethylene dichloride
EDS	energy-dispersive X-ray spectroscopy
EISA	evaporation-induced self-assembly
EtOH	ethanol
EXAFS	extended X-ray absorption fine structure
FFT	fast fourier transform
FT-IR	fourier transform infrared spectroscopy
FTO	fluorine tin oxide
GIXS	grazing-incidence X-ray scattering
IFT	inverse fourier transform
ITO	indium tin oxide
LC	liquid crystal
MALDI-TOF MS	matrix-assisted laser desorption ionization-time-of-flight mass spectrometry
MeOH	methanol
NMR	nuclear magnetic resonance
OLED	organic light emitting diode
OPV	oligo(*p*-phenylene vinylene)
P3HT	poly-3-hexyl thiophene
PEG	poly(ethylene glycol)
PHEMA	poly(2-hydroxyethyl methacrylate)
PL	photoluminescence
PM-IRRAS	polarization modulation-infrared reflection-absorption spectroscopy
PMMA	polymethyl methacrylate

LIST OF ABBREVIATIONS (cont.)

POM	polarized optical microscopy
PV	photovoltaic
PyBA	pyrenebutyric acid
PyCA	pyrenecarboxylic acid
RT	room temperature
SAXS	small-angle X-ray scattering
SDS	sodium dodecyl sulfate
SEM	scanning electron microscopy
STEM	scanning transmission electron microscopy
T_i	isotropization temperature
TEM	transmission electron microscopy
TEOS	tetraethyl orthosilicate
TFA	trifluoroacetic acid
TGA	thermal gravimetric analysis
THF	tetrahydrofuoran
UV	ultraviolet
WAXS	wide-angle X-ray scattering
XANES	X-ray absorption near edge structure
XAS	X-ray absorption spectroscopy
XRD	X-ray diffraction
XRR	X-ray reflectivity

TABLE OF CONTENTS

LIST OF FIGURES

Chapter 2 Liquid-Crystalline Phases of Conjugated Amphiphiles

LIST OF TABLES

page

CHAPTER ONE

Introduction and Background

Chapter 1: Introduction and Background

1.1 Objective and Significance

Hybrid materials combine the physical and chemical properties of two or more distinct materials to create a composite with unique and improved properties. Biology and nature provide us with beautiful examples of organic-inorganic hybrid-based materials, including mollusk shells whose lustrous appearance is due to their inner lining, nacre.[1, 2] Although unintentionally at first, man has also been creating organic-inorganic hybrids since ancient times, with examples including that of Maya blue wall paintings that contain organic indigo dye molecules encapsulated by an inorganic host, the clay mineral palygorskite.[3] Since the industrial revolution, organic-inorganic hybrids have been made intentionally designed to improve, for example, the optical and mechanical properties of paint additives.[3, 4]

The emerging field of nanoscience, involving the design of materials on the nanoscale (1-100 nm), has offered scientists the ability to better understand the importance of interfaces and degree of organization of such hybrids materials. In so doing, novel functional materials have been attained in a host of applications, such as catalysis,[5, 6] optical and electronic behavior,[7, 8] light emission,[9-11] and photovoltaic function,[12-14] to name a few. The challenge of controlling the interfaces and organization relies heavily on the synergistic interaction of the two phases, and thus, the emergence of soft-inorganic chemistry syntheses has allowed for the mixing of components on the nanometer scale beyond the conventional physical means.[15-18]

At the same time, advances in synthetic chemistry have afforded us the power to design molecules, from simple precursors, with well-defined structural and chemical functionality. By using the principles of molecular self-assembly, designed molecules can self-organize

themselves into sophisticated and well-ordered nanostructures. This strategy is particularly useful for designing organic-based electronic materials, where molecular structure directly affects the properties and performance of resulting devices.

With these tools in hand, an especially important application of hybrid organic-inorganic materials is in the area of photovoltaics, a promising, inexpensive source of renewable energy. Hybrid photovoltaics devices combine the low-cost and mechanical flexibility of organic materials, with the improved conductivity properties of inorganic materials. The control over the interfaces and organization of such systems is especially crucial due to charge trapping and recombination effects that can significantly decrease device performance. Given the ability of electronically active amphiphiles to self-organize on the nanoscale, the incorporation of such materials into photovoltaics offers the ability to design well-ordered nanostructures and interfaces. Consequently, this thesis investigates the nanoscale ordering and enhanced luminescence achieved by self-assembling electronically active organic materials. In so doing, these organic materials have been further exploited as the structure-directing agents in the facile synthesis and design of hybrid nanostructures which exhibit long-rang ordering and can now be incorporated into photovoltaic devices.

1.2 Self-Assembling Organic Electronic Materials

1.2.1 Self-organization by molecular self-assembly

Molecular self-assembly is a bottom-up approach, inspired by nature, which involves the spontaneous organization of molecules into discrete patterns or structures without human intervention.[19, 20] Such ordering is achieved by designing molecules that are amphiphilic in character. The term amphiphile refers to a molecule with two or more physically distinct

components, with one of the segments being hydrophilic. It is the hydrophilic segment that also defines the character of the amphiphile. There are four subclasses of amphiphiles: cationic, anionic, zwitterionic, and nonionic. In the case of non-ionic amphiphiles, the hydrophile is polar in nature, but lacks any formal charge, such as poly(ethylene oxide), also known as poly(ethylene glycol), which is used in Chapter 2. Cationic amphiphiles contain positively-charged head groups, such as quaternary ammonium salts, and are used in Chapter 3 of this thesis. Anionic amphiphiles, on the other hand, contain negatively-charged head groups, such as sulfonate salts and carboxylates, and are employed in Chapter 4. The zwitterionic amphiphiles, which will not be discussed, contain both positive and negative head groups.

Amphiphiles are commonly used in molecular self-assembly to design liquid crystals through weak van der Wals interactions. Liquid crystals represent an intermediate phase between solids, which exhibit both positional and orientational ordering, and liquids, which exhibit no order.[21-23] Consequently, such mesophases exhibit a preferred orientation and possess a director which defines their average ordering. In smectic structures, for example, molecules are oriented in the same direction and are aligned as layers or planes with respect to one another. Liquid crystals can be divided into two classes. The first, thermotropic phases, are temperature-dependent and exist for molecules in their neat form over a specified temperature range.

Lyotropic phases, on the other hand, are concentration-dependent and exist at an appropriate concentration of a suitable solvent over a specified temperature range. Amphiphilic systems can form various lyotropic phases due to the balancing of competing repulsive and attractive forces between the hydrophobic and hydrophilic segments, and the resulting packing parameter of the molecules and curvature of the interface between segments.[24, 25] In dilute

solutions, amphiphiles or surfactants, will be isolated from one another. As their concentration is increased, spherical micelles form at the dilute limit, or critical micelle concentration (CMC). With further increase in concentration, these spherical micelles will transform into rod-like micelles, which will then elongate and pack into hexagonal arrays. From there, bicontinuos cubic phases, and finally lamellar phases, will form. In essence, the driving force for self-assembly is aggregation and collapse of the hydrophobic segments which shield themselves from unfavorable interactions with the solvent. Two of the structures formed, as mentioned and illustrated in Figure 1.1 from the literature,[26] are the lamellar packing, consisting of alternating layers of hydrophobic and hydrophilic layers, and the hexagonal packing, consisting of hydrophobic cores surrounding by a hexagonal hydrophilic continuum. Both of these structures will be discussed in more detail throughout this thesis. Further advances in supramolecular chemistry, have allowed researchers to design more sophisticated nanostructures through other non-covalent interactions, such as hydrogen bonding and π–π stacking.[27-33] Examples of such structures are illustrated in Figure 1.2.[34]

1.2.2 Role of molecular ordering on electronic behavior

In contrast to inorganic semiconductors, organic semiconductors exhibit highly localized electron wavefunctions.[35] As a result, increased conductivity in organic semiconductors relies on the π-orbital overlap of the conjugated segments between molecules, and enhanced luminescence relies on reducing this overlap to prevent non-radiative recombination and exciton quenching. Supramolecular chemistry can therefore be used to control the aggregation state of conjugated molecules.[36, 37]

(a)

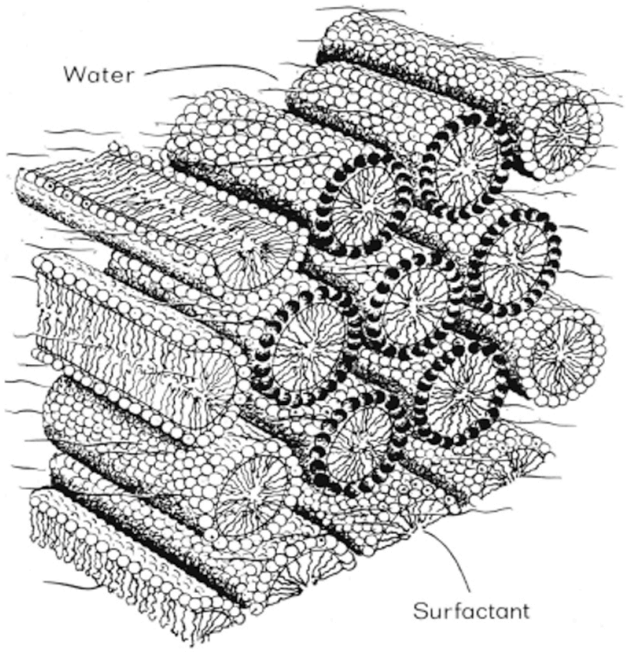

(b)

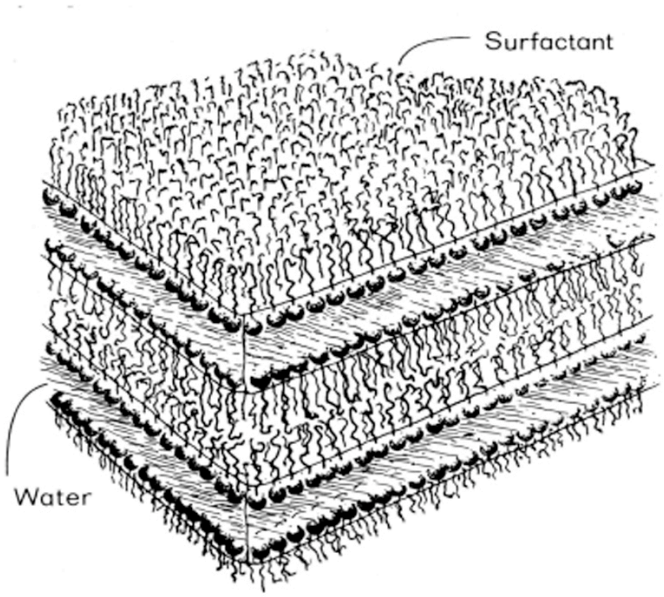

Figure 1.1. Schematic illustrations of lyotropic liquid crystalline phases of **(a)** hexagonal (H_1) and **(b)** lamellar ordering (L_α). (Reproduced from Khetrapal, C.L. *Nuclear Magnetic Resonance Studies in Lyotropic Liquid Crystals.* Spring-Verlag: New York, **1975**, 189).

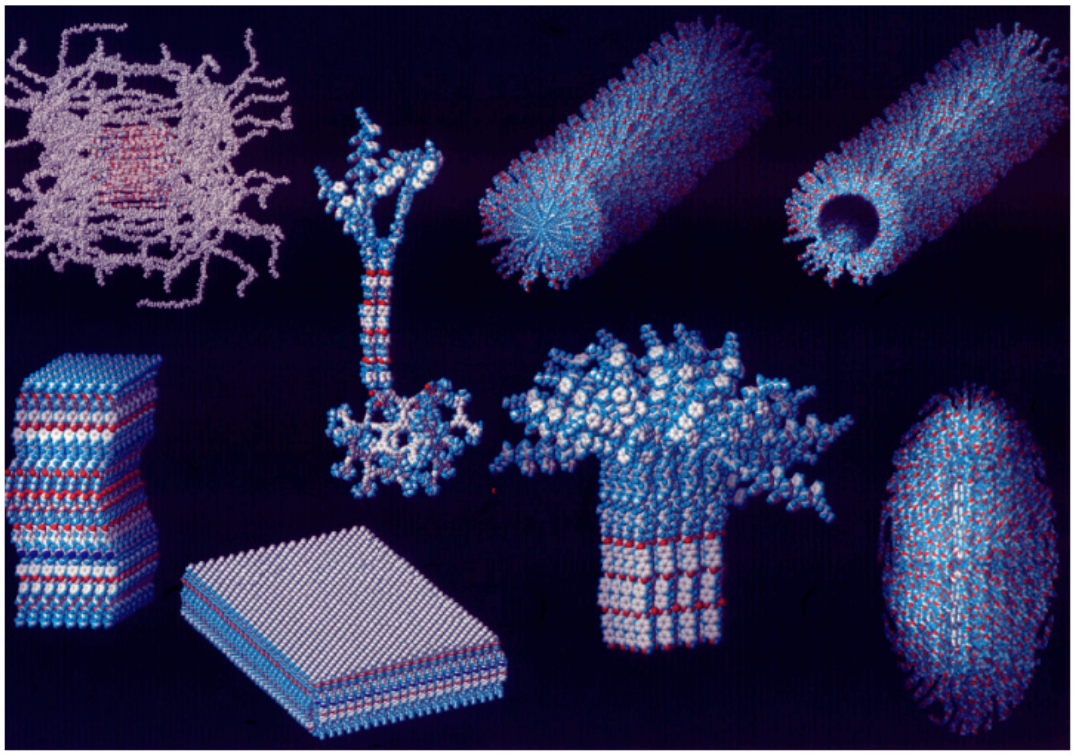

Figure 1.2. Examples of nanostructures formed by supramolecular non-covalent interactions. (Reproduced from Stupp, S.I. et al., MRS Bulletin **2000,** 25 (4), 42 with permission, copyright Materials Research Society).

Specifically, due to their ordered structures, which can allow for anisotropic transport and enhanced charge mobility, liquid crystals can be advantageous compared to amorphous polymeric networks in organic electronics.[38-40] Liquid crystals containing chromophores such as phenylene vinylene[41-45] and thiophene[46-51] have been developed. Due to more well-defined structure, the oligomeric analogues of conjugated polymers allow for better molecular ordering, reducing the density of defects which can lead to unfavorable charge trapping.[52-55] For this reason, derivatives of oligo(phenylene vinylene) (OPV)[56-58] and oligothiophene[59, 60] have found application in electronic devices. Therefore, supramolecular chemistry offers a viable means to control nanoscale morphology versus polymer blends. As is described in the following section, molecular self-assembly and supramolecular chemistry can also be exploited to design highly-ordered nanostructures of hybrid organic-inorganic materials.[61] The key challenge is synthesizing the inorganic phases under conditions and temperatures that are suitable for their organic counterparts.

1.3 Molecular Self-Assembly Strategies for Hybrid Synthesis

1.3.1 Template-driven synthesis

In one self-assembly approach in synthesizing hybrid nanostructures, the amphiphilicity of the synthetic organic molecules is used to control the resulting nanoscale ordering of the organic and inorganic domains.[62-65] This is accomplished, for example, by using the pre-ordered soft organic to guide the growth of inorganic components in hydrophilic domains and control their size, shape, and location. This particular strategy is inspired by biomineralization processes in nature,[66, 67] and therefore, template-driven synthesis of hybrids is biomimetic in character.[21] Our own group has used amphiphilic lyotropic liquid crystalline templates to synthesize

nanostructured II-VI semiconductors.[68-72] The resulting composite superlattice morphology directly copies the original organic matrix with the semiconductor forming in the hydrophilic regions and locking in the amphiphilic molecules (see Figure 1.3). More sophisticated helical nanostructures have since been designed using this methodology.[73, 74] Nanostructured films of II-VI semiconductors[75, 76] and metals[77-79] have also been electrodeposited using lyotropic liquid crystalline templates.

1.3.2 Co-assembly syntheses

The amphiphilicity of organic molecules can also be used in a dynamic co-assembly approach. In this case, the surfactants, at concentrations below their critical micelle concentration, are mixed with inorganic precursors and their electrostatic interactions lead to organization at the nanoscale. Kresge et al. pioneered this strategy in producing mesoporous silica after the organic component is removed from the pores.[5, 6] With variations to the surfactant, inorganic precursors, and processing conditions, a number of mesoporous hybrids have been developed using sol-gel chemistry.[80, 81] Such processing has since been extended to thin-film formation,[82-85] resulting in the one-step evaporation-induced self-assembly (EISA) process. EISA, as shown in the phase diagram in Figure 1.4 for cetyltrimethylammonium bromide (CTAB) and silica, relies on preferential solvent evaporation from dilute homogeneous solutions to form highly-ordered mesophases.[86-88] Instead of relying on sol-gel chemistry, the inorganic phase can also be synthesized through an electrochemical approach.[89, 90] Figure 1.5 illustrates the hybrid lamellar structures formed by electrodeposition.

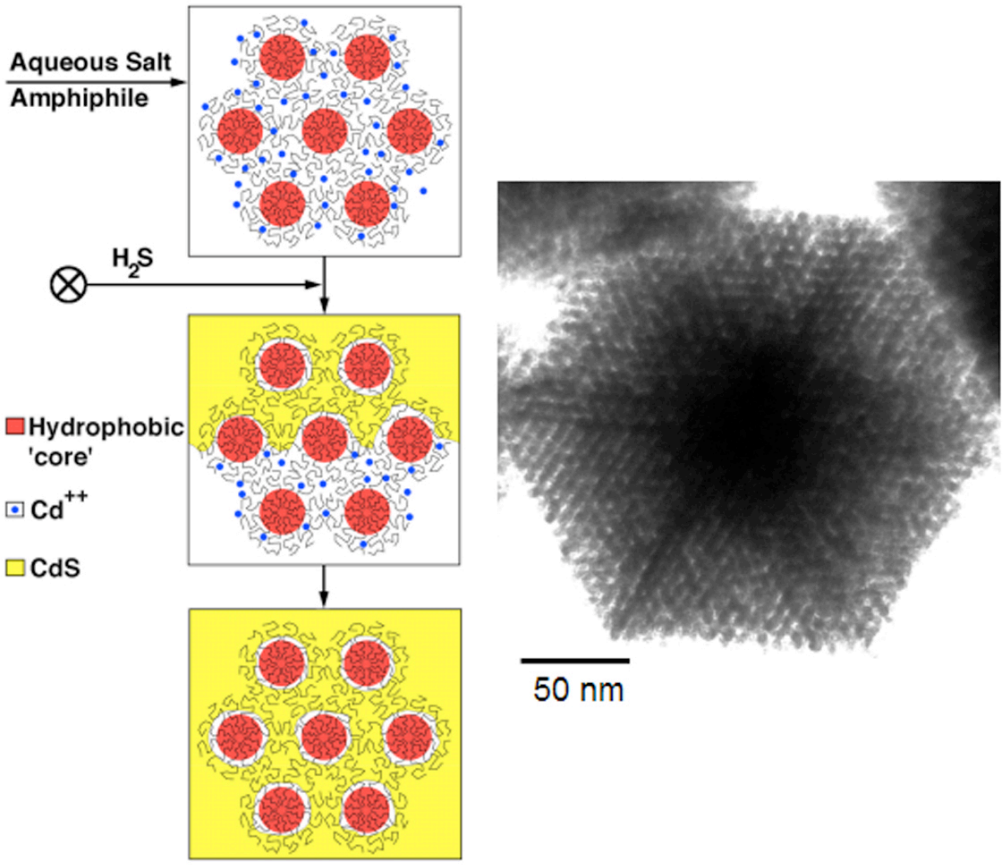

Figure 1.3. Example of direct liquid crystal templating of CdS with a schematic representation of the synthesis (left) and a TEM image of the resulting superlattice (right). (Reproduced from Stupp, S.I. et al., Chem. Mater. **1997,** 9, 1496; J. Amer. Chem. Soc. **1999,** 121, 7304 with permission, copyright American Chemical Society).

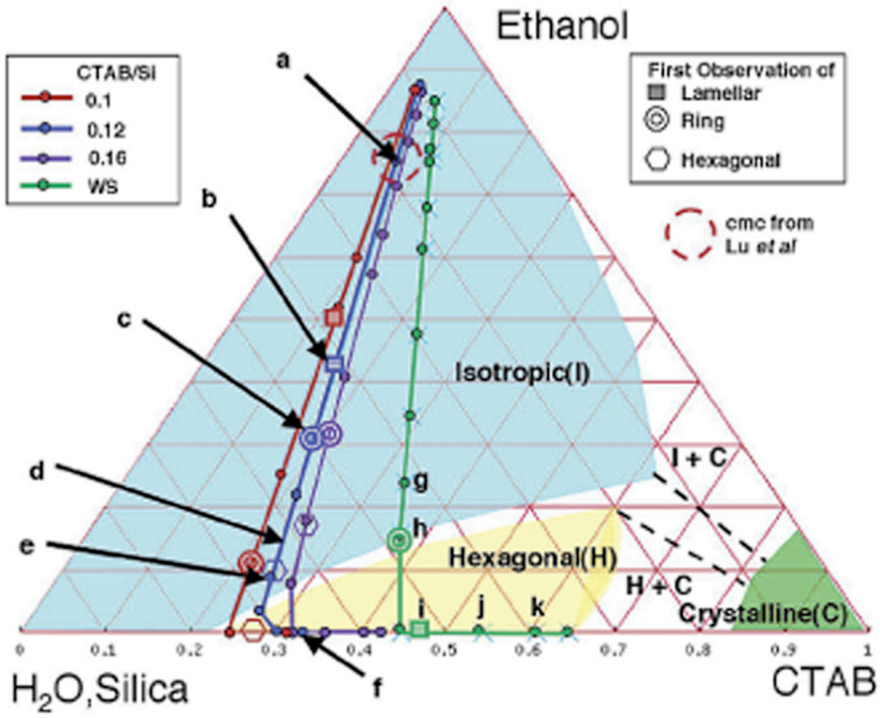

Figure 1.4. Schematic of ternary phase diagram of CTAB/water with evaporation-induced compositional trajectories of CTAB/silica films as a function of silica concentration. (Reproduced from Brinker, C.J. et al., J. Amer. Chem. Soc. **2003,** 125, 11649 with permission, copyright American Chemical Society).

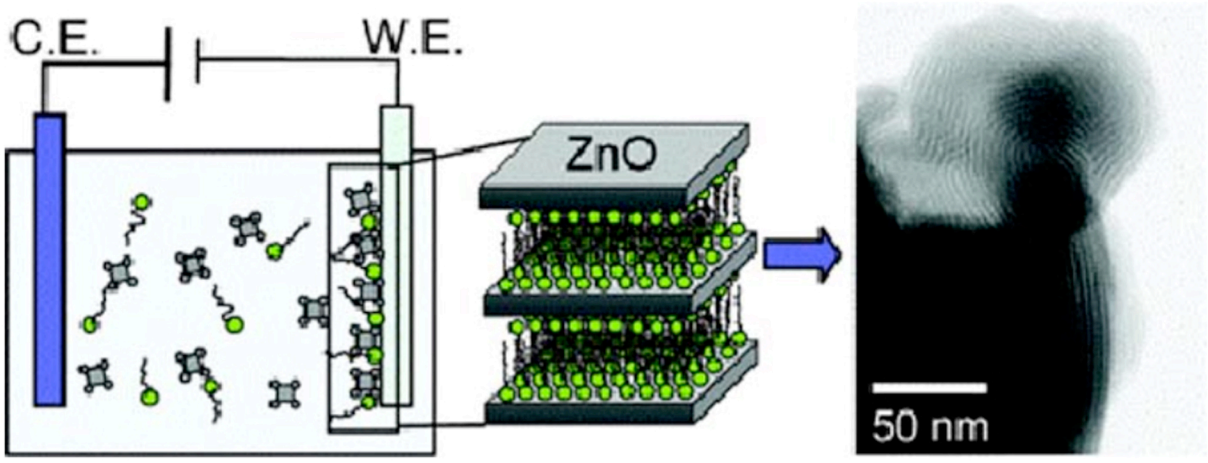

Figure 1.5. Example of surfactant-assisted electrochemical templating with a schematic representation of the synthesis (left) and a TEM image of the resulting lamellar ordering (right). (Reproduced from Choi, K.-S. et al., Langmuir **2005,** 21, 9618 with permission, copyright American Chemical Society).

1.4 Photovoltaic Properties of Hybrid Materials

In the area of photovoltaics, organic semiconductors have received significant attention as low-cost alternatives to the traditional inorganic solar cells because they do not require high temperature processing and complicated lithographic steps.[91-93] In addition, the energy gaps and ionization potentials of conjugated polymers can be altered by simple chemical modification of the chromophore. In organic semiconductors, however, photoexcitation upon light absorption in a solar cell does not directly result in the formation of free charge carriers, rather an exciton, or strongly bound electron-hole pair, is generated.[94-96] In order to produce the current necessary for a photovoltaic effect, the presence of two materials is required, therefore, to effectively separate the positive (holes) and negative (electrons) charge carriers so that they can each migrate to their respective electrodes without recombination occurring. In this context, heterojunction photovoltaic devices are designed consisting of an electron donor (p-type) and electron acceptor (n-type) materials, which allow for separation of excitons when the acceptor has a higher electron affinity and ionization potential than the donor. Figure 1.6 illustrates the operation of such a bulk heterojunction device.

The nanoscale morphology of heterojunction photovoltaic devices is critical to their performance. Specifically, charge carriers must be efficiently separated, prevented from recombining prior to collection, and transported through their respective layers. The exciton lifetime and diffusion length in organic semiconductors is limited by radiative and non-radiative decay, and therefore only excitons photogenerated near the p-n interface give rise to charges. The exciton diffusion length in polymers, only 5-10 nm, is much less than the optical absorption length, and therefore, organic-based cells absorb light more easily than the resulting excitons are

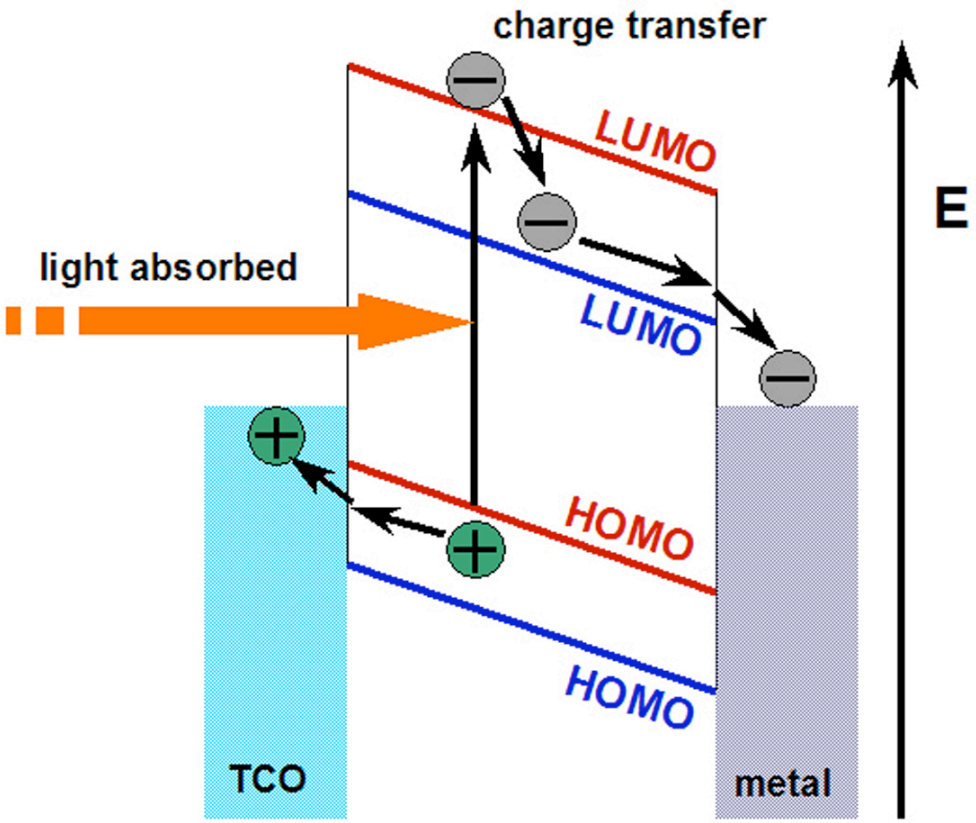

Figure 1.6. Schematic illustration of the operation of a bulk heterojunction excitonic solar cell with electron donor (red) and acceptor (blue) energy levels and movement of charges to respective electrodes upon light absorption and exciton separation.

split. This exciton diffusion "bottleneck" is a problem characteristic of organic semiconductors.[97] Consequently, close spacing of the two materials with well-defined chemical linkages is necessary to maximize charge separation, as well as maintain a high degree of ordering to optimize the flow of charges.

While conjugated polymers are particularly attractive electron-donating candidates with good hole mobilities, they usually exhibit relatively low electron mobilities (10^{-4} $cm^2V^{-1}s^{-1}$)[98] compared to inorganic devices, which severely limits their resulting solar power conversion efficiencies. For this reason, one class of organic-containing solar cells, are hybrid devices, which consist of a hole-transporting organic phase and an electron-transporting inorganic phase. Grätzel cells, which consist of dye-sensitized mesoporous titania and a liquid electrolyte solution, and are actually photoelectrochemical cells due to their operation by a different mechanism than the hybrids discussed, have achieved the highest efficiencies for non-inorganic solar cells.[14, 99] A number of architectures have been designed of hybrid cells that have included CdSe,[13, 100-102] TiO_2,[12, 103] ZnO[104-107] as the inorganic component.

Controlling the overall nanoscale morphology, as well as the ordering within the charge pathways, however, remains a non-trivial matter. With the vision illustrated in Figure 1.7, in mind, where the p- and n-type pathways are well-ordered and vertically-aligned on the nanoscale, this thesis aims to utilize molecular self-assembly to attain this goal in a facile, one-step manner. Chapter 2 explores the liquid-crystalline mesophase ordering achieved by non-ionic triblock amphiphiles containing either phenylene vinylene and thiophene oligomers and how this nanostructure can be used to optimize aggregation and exciton migration of the chromophores. Further attempts are made to mineralize and grow an inorganic phase of ZnO

within the hydrophilic domains of the LC structure. In Chapter 3, the dynamic co-assembly approach, EISA, is used with cationic bolaamphiphiles containing OPV and thiophene oligomers to form nanostructured hexagonal arrays with silica that exhibit long range ordering. Finally with lessons learned from the previous two systems, in Chapter 4, an electrochemical synthesis of ZnO is employed to form well-ordered lamellar sheets of alternating layers of n-type ZnO and various aromatic p-type-containing anionic amphiphiles.

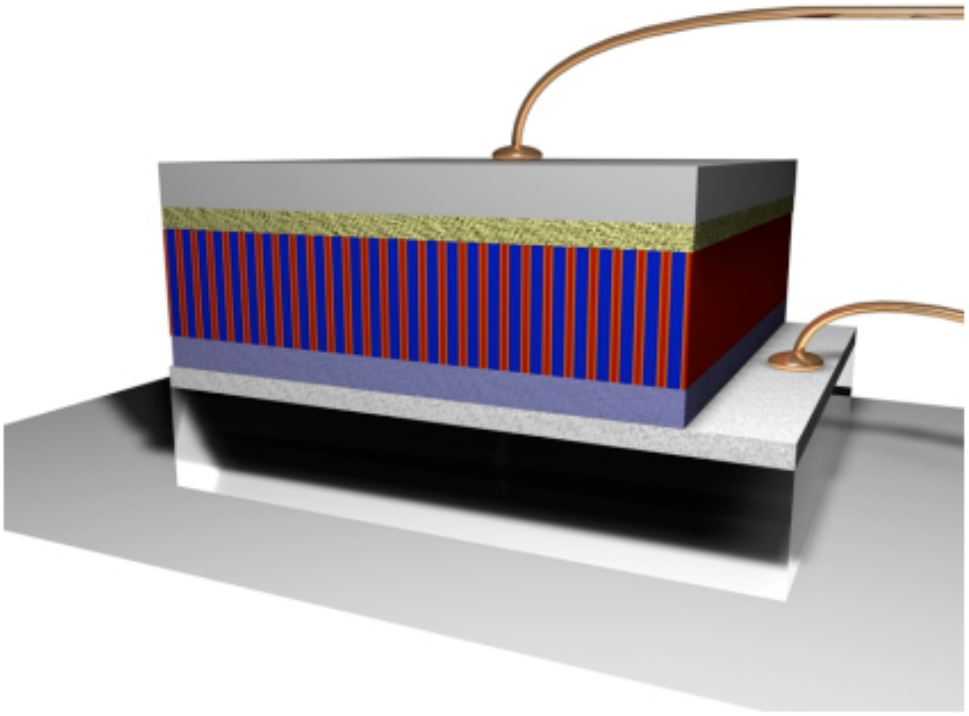

Figure 1.7. Schematic illustration of targeted hybrid solar cell with vertically aligned organic hole-transporting (red) and inorganic electron-transporting (blue) layers allowing for movement of charges to respective electrodes upon light absorption and exciton separation without charge recombination or trapping.

CHAPTER TWO

Liquid-Crystalline Phases of Conjugated Amphiphiles

Chapter 2: Liquid-Crystalline Phases of Conjugated Amphiphiles

2.1 Introduction

Chromophore-containing liquid crystals allow for anisotropic transport and enhanced charge mobility in organic electronic devices compared to amorphous polymeric networks. [38-51] In addition, the oligomeric analogues of conjugated polymers, due to their more well-defined structures and chemistries, allow for better molecular ordering, reducing the density of defects which can lead to unfavorable charge trapping.[52-55] For this reason, derivatives of oligo(phenylene vinylene) (OPV)[56-58] and oligothiophene[59, 60] have found application in organic electronic devices.

In this chapter, we report on the lamellar phase LC phases formed by a series of amphiphilic triblock molecules comprised of an OPV or oligothiophene core and substituted asymmetrically on either end with a hydrophilic poly(ethylene glycol) (PEG) block and a hydrophobic alkyl block.[45] Due to their amphiphilic nature, these molecules self-organize into thermotropic and lyotropic LC mesophases with long-range order. The solubility and mesophase structure can be tuned by controlling the length of the PEG block. In a detailed study of the lyotropic LC mesophase formed by the OPV derivative, we find that the amphiphilic structure controls the chromophore aggregation state, influencing exciton mobility and fluorescence, and potentially leading to improved charge carrier mobility.

The hydrophilic PEG regions in the aforementioned lamellar structures are further used in attempting to template the mineralization and growth of an inorganic electron acceptor material. Our own group has previously reported on the use of amphiphilic lyotropic liquid crystalline templates to synthesize nanostructured II-VI semiconductors.[68-72] However, the amphiphiles

used in those cases were not electronically active. In the present study, the synthesis of ZnO is targeted because it is a well-studied electron acceptor in solar cell devices and single-crystalline ZnO can be readily synthesized at low temperatures that are compatible with the organic surfactant.[108] The formation of single-crystalline TiO_2, for example, requires annealing to > 350 °C; a temperature at which organic molecules decompose.[109] Such a synthesis of ZnO nanoparticles using the hydrolysis and condensation of diethylzinc has been previously used with commercially available poly(phenylene vinylene) derivatives.[104] The target in this scheme is for the inorganic precursor to be attracted to the hydrophilic PEG channels of the LC and to convert to ZnO within its confines.

2.2 Synthesis of Non-Ionic OPV and Oligothiophene Amphiphiles

2.2.1 Non-ionic OPV-PEG synthesis

The non-ionic OPV-PEG-n amphiphiles were synthesized by Dr. Keisuke Tajima, of the author's laboratory, with details of the synthesis published elsewhere.[45] The synthetic scheme, as outlined in Figure 2.1, uses the Horner-Wadsworth-Emmons reaction for the formation of *trans*-vinyl bonds in the OPV trimer core. The PEG block was varied from n ~ 8 to 45 to study the thermotropic LC behavior as a function of hydrophile length.[45] The focus of this chapter, however, will be on the lyotropic LC behavior exhibited by the OPV-PEG-45 derivative.

2.2.2 Non-ionic oligothiophene-PEG synthesis

The non-ionic oligothiophene-PEG-n series of amphiphiles were synthesized by David Stone, of the author's laboratory. Derivatives with four and five repeat units of thiophene were synthesized, and PEG blocks of n ~ 24 and 45. The synthesis and reaction conditions shown in

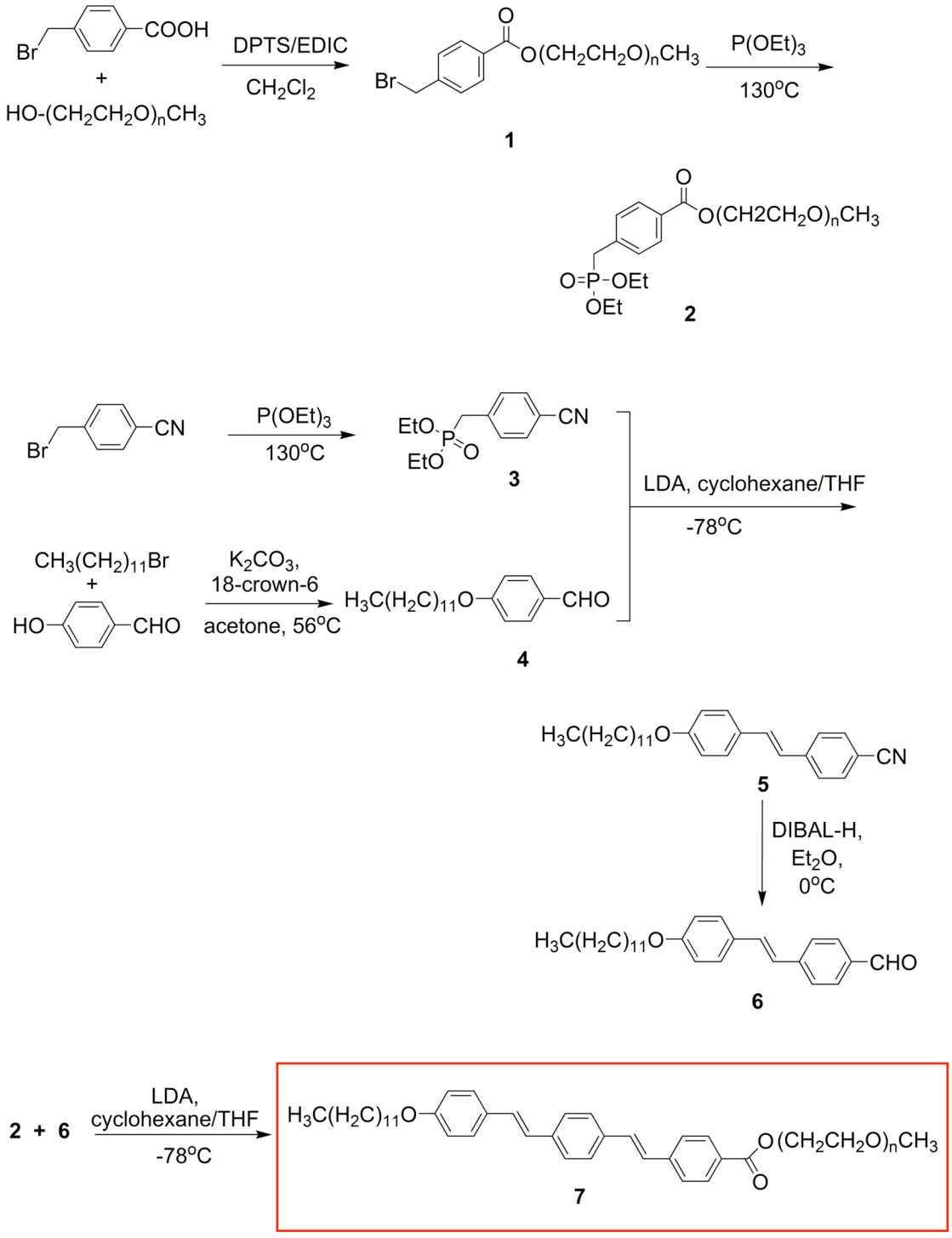

Figure 2.1. Chemical synthetic scheme for OPV-PEG-n amphiphiles with n ~ 8, 12, 14, 24, and 45. (prepared by Dr. Keisuke Tajima).

Figure 2.2 and described in detail in Appendix I.1 are for the quinquethiophene amphiphiles, 5T-PEG-24, which were primarily used in the synthesis of zinc oxide (*vide infra* Section 2.5).

2.3 Lyotropic Liquid Crystalline Behavior of OPV-PEG Amphiphiles

2.3.1 Lyotropic LC gel formation and structural characterization

In addition to exhibiting themotropic mesophases, these amphiphiles are also soluble in most polar solvents, including water for PEG blocks of n ~ 24 and 45, and form lyotropic LC mesophases at concentrations above 30 wt%. As shown in Figure 2.3 (a), the OPV-PEG-45 forms a highly viscous, transparent gel, which when illuminated with UV light, is also strongly fluorescent, despite the high concentration of OPV.

Polarized optical microscopy confirms the LC behavior of aqueous gels of OPV-PEG-45 where strong birefringence is observed from the uniform switching of bright to dark upon 45° rotation of the crossed polarizers (see Figure 2.3 (b)). Further, homogeneous alignment is induced by shearing with relatively large domain sizes (mm) attained, as shown in Figure 2.3 (b).

As observed in the thermotropic case, small-angle X-ray scattering identified the formation of lamellar ordering in the lyotropic LC gels. Table 2.1 shows the first-order diffraction peak for the lamellar ordering and isotropization temperature for solvents in which the lyotropic LC was observed. The isotropization temperatures, which will be discussed further in the following section, were obtained by differential scanning calorimetry (DSC).

When the OPV amphiphile was cast as a film from a dilute, aqueous solution and the solvent evaporated, SAXS again identified the formation of a lamellar structure (see Figure 2.4 (a)). The layer spacing, however, increases so that the (001), (002), and (003) peaks are equal to 15.4 nm, 7.6 nm, and 5.0 nm, respectively. This increase is attributed to the rearrangement of the

PEG chain. These chains typically form a 7/2, or 7 monomer repeat units per 2 turns, helical conformation with a pitch of 1.93 nm on drying.[110] The expected length, therefore, of the OPV-PEG-45 amphiphile is 12.5 nm, and the increased length indicates that a bilayer structure (see Figure 2.4 (b)) is formed with full interdigitation of the PEG layers. While it would be expected for the OPV-PEG-45 amphiphiles to pack in a hexagonal structure due to the long, bulky PEG chains which increase the curvature of the hydrophobic-hydrophilic interface,[25] the observation of a lamellar phase most likely results because of the aggregation of the chromophore segments which frustrate hydrophobic collapse and increase the molecular cross-section at the interface.

Table 2.1. Lamellar Spacing and Isotropization Temperature for Lyotropic OPV LCs

solvent	***d_{001} (nm)***	***T_i (^oC)***
H_2O	11.0	>100
DMSO	11.1	68
CH_3CN	11.3	55
DMF	13.1	52

2.3.2 Temperature dependence of lyotropic LC structure

In order to gain a better understanding of lyotropic LC structures formed, temperature-dependent studies were performed. In the case of the aqueous gel, the mesophase was retained up to the boiling point of the water. This stability is attributed to the strong interactions between the water and the PEG chains. Consequently, less polar solvents, that would interact more weakly with the PEG chains and undergo isotropization at a suitable temperature below the solvent boiling point, were used to compare the behavior of the self-assembled LC state and the disordered state.

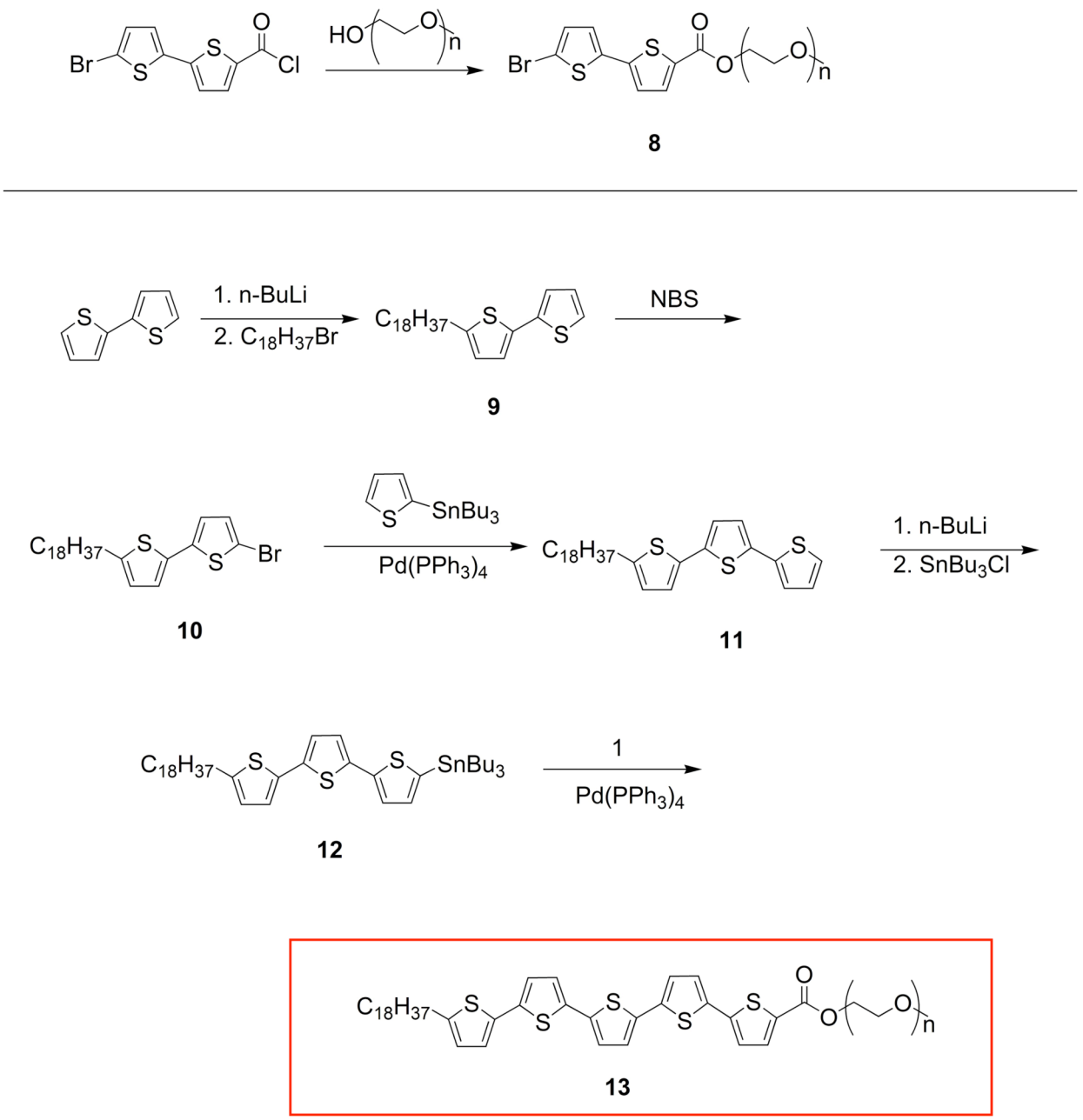

Figure 2.2. Chemical synthetic scheme for 5T-PEG-n amphiphiles with n ~ 24 and 45. (prepared by David Stone).

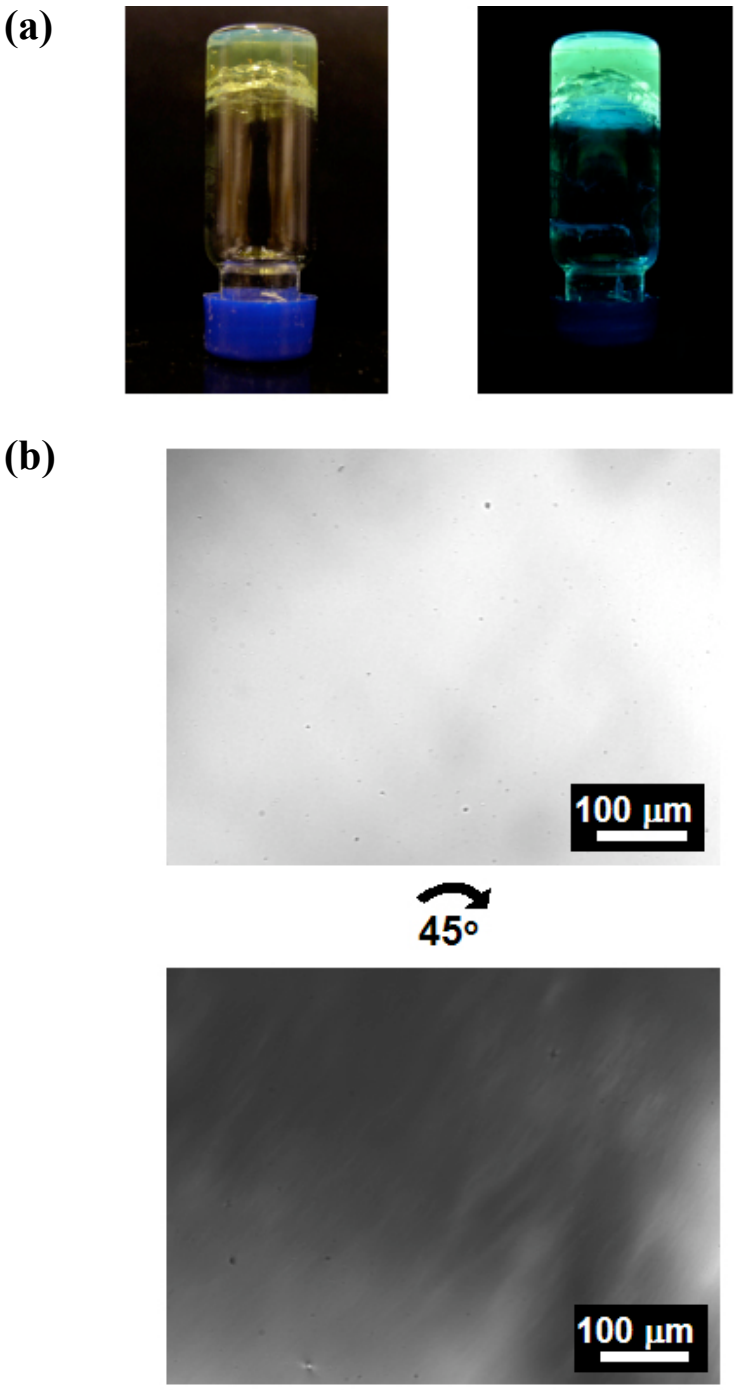

Figure 2.3. **(a)** Photographs of inverted vials of aqueous, lyotropic LC gel of OPV-PEG-45 amphiphile under visible (left) and UV (right) light. **(b)** POM images of shear induced homogenous alignment of aqueous LC switching from bright (top) to dark (bottom) on 45° rotation of crossed polarizers. (Reproduced from Hulvat, J. F. et al., J. Am. Chem. Soc. **2005**, 127, 370 with permission, copyright American Chemical Society).

(a)

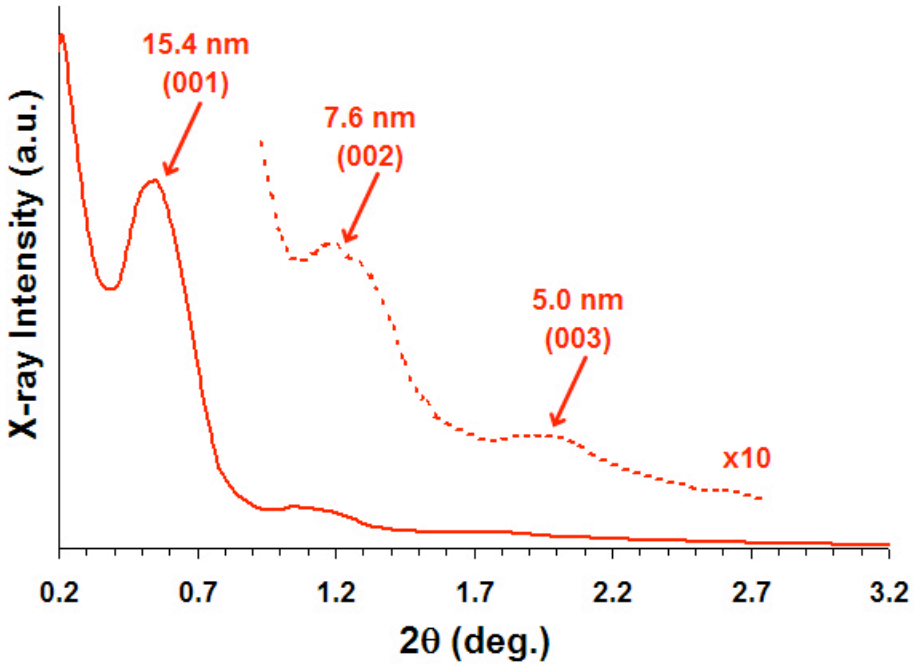

(b)

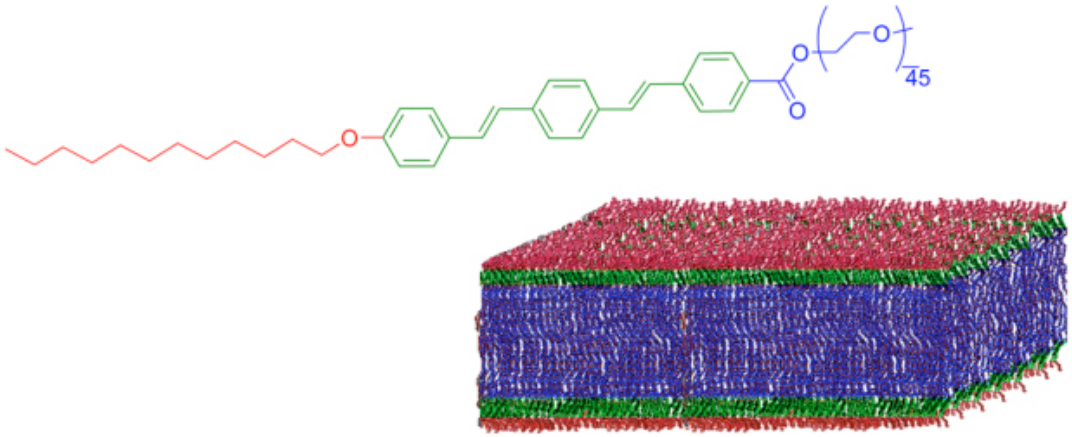

Figure 2.4. (a) SAXS spectra showing lamellar periodicity of aqueous dried gel of OPV-PEG-45 cast from dilute solutions. **(b)** Chemical structure of OPV-PEG-45 amphiphile and molecular graphics illustration of resulting bilayer packing.

In particular, acetonitrile was used to form a 40 wt% gel of OPV-PEG-45. A birefringent texture was observed by POM for the gel (see Figure 2.5 (a)), however, due to the weaker interactions present, the domain sizes evident are smaller in acetonitrile compared to the domains present in aqueous gels. The DSC trace (see Figure 2.5 (b)) indicates that the LC is disrupted and becomes a solution at an isotropization temperature of $T_i \sim 55$ °C. This transition is further confirmed by the POM image at 60 °C where birefringence disappears. The two-stage transition in the DSC suggests the occurrence of some rearrangement within the lamellar structure. The disruption of the LC structure is attributed to the melting of the PEG, which occurs near T_i.

The lamellar-to-isotropic transition observed in the 40 wt% gel of OPV-PEG-45 in CH_3CN was investigated further by variable-temperature SAXS measurements. At room temperature, as shown in Figure 2.6, a layer spacing of 10.3 nm is observed. By raising the temperature of the gel, a shift in the spacing from 10.3 nm to 11.2 nm occurred at 50 °C indicating that a swelling of the structure occurs as the solvent molecules began to dissociate from the PEG chains of the amphiphiles. This increase was coupled with a rise in the diffraction intensity, suggesting that the OPV portions of the structure, which should scatter the most due to their high electron density, become more ordered as the PEG regions swells. As should be expected, the peak completely disappears as isotropization is reached and the ordered LC transformed into a disordered liquid.

2.3.3 Temperature dependence of lyotropic LC photoluminescence

Temperature-dependent photoluminescence was used to compare the aggregation state of the OPV chromophore between the ordered LC and the disordered isotropic liquid. Again,

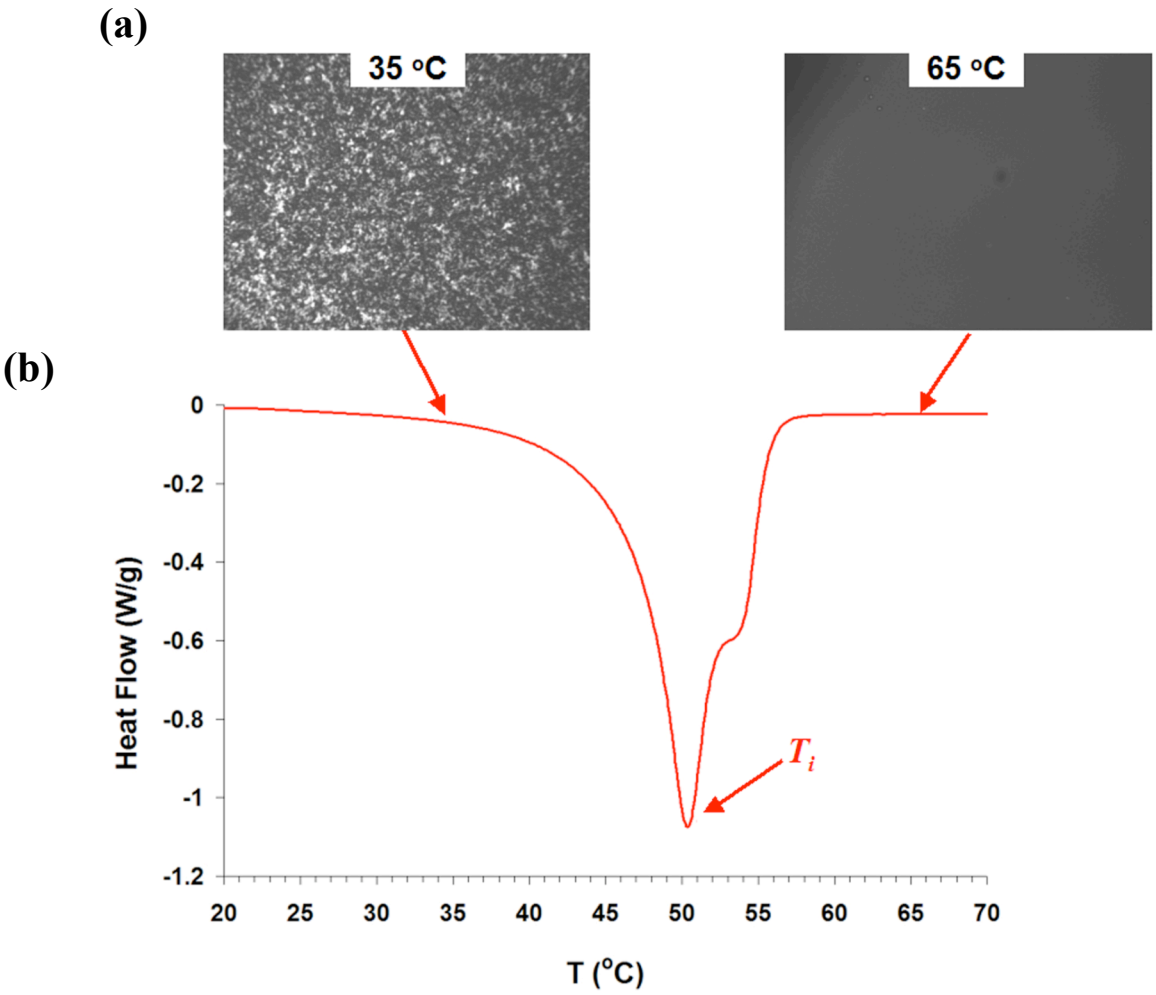

Figure 2.5. **(a)** POM images of 40 wt% OPV-PEG-45 amphiphile in CH_3CN, in LC, gel state (left) and in isotropic, liquid state (right). **(b)** DSC heating cycle of 40 wt% OPV-PEG-45 amphiphile in CH_3CN (exothermic up).

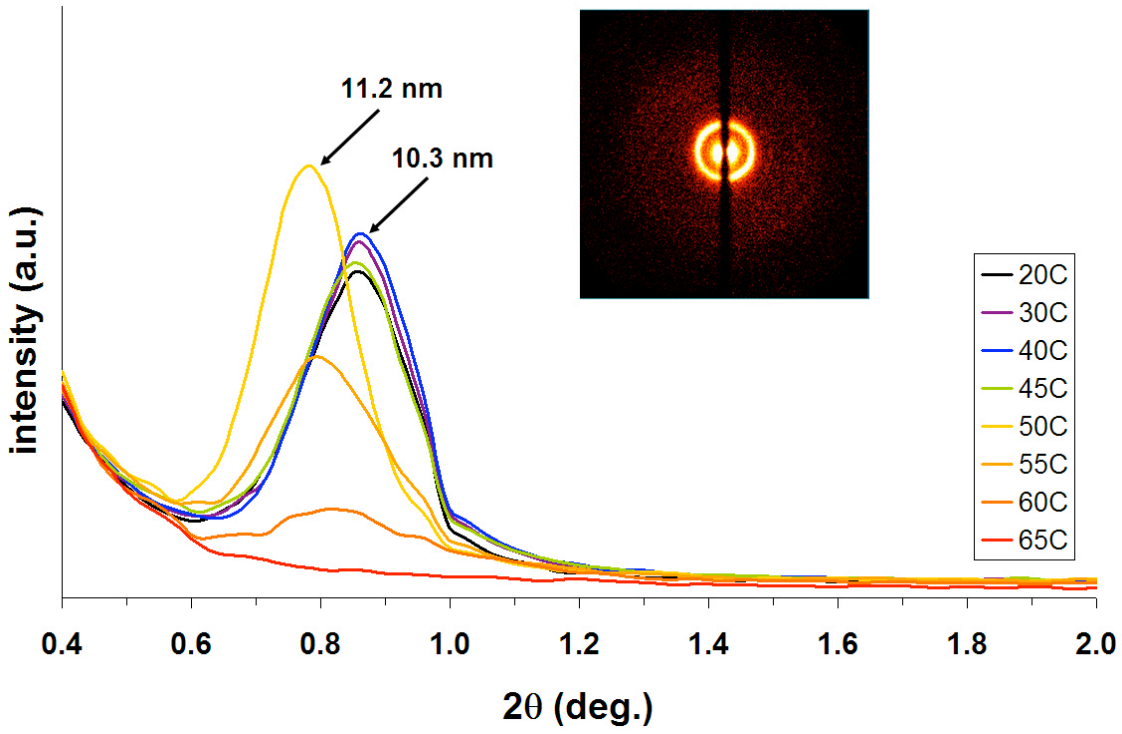

Figure 2.6. Variable-temperature small-angle X-ray scattering of 40 wt% OPV-PEG-45 amphiphile in CH_3CN, with inset showing 2D diffraction pattern.

because of the inability to disrupt the aqueous mesophase, acetonitrile was further investigated. The fluorescence emission was scanned at each temperature by exciting the gel at 475 nm, the edge of the absorption band to allow for transmission through the entire sample. As is shown in Figure 2.7 (a), the fluorenscence intensity is actually enhanced in the LC state compared to the disordered state above the isotropization temperature where fluorescence was quenched. This behavior was reversible and was not observed in a dilute solution of 0.7 wt% of the OPV-PEG-45 in acetonitrile. This result indicates that the aggregation state of the OPV chromophore is affected by the structural organization of the amphiphile. Figure 2.7 (b) displays the results of the temperature-dependent SAXS and PL scans on the same graph and further identifies a direct connection between the structural rearrangement at the LC-to-isotropic transition and the quenching of the OPV fluorescence exists. In the LC phase, the amphiphiles arrange in confined 2D layers. The structural dominance of the PEG groups must isolate the OPV portions from one another within their layers and maximize their fluorescent emission. As the LC structure is disrupted, the amphiphiles are able to rearrange and form small, disordered aggregates of the OPV chromophores, thereby quenching the photoluminescence.

More insight into the OPV aggregation is provided by the results of variable-temperature ^{1}H NMR on the gel of the OPV-PEG-45 amphiphiles in deuterated acetonitrile (see Figure 2.8). The peaks in the aromatic region, corresponding to the protons in the OPV, are broadened in the LC phase. As the PEG groups melt and the LC-to-isotropic transition is reached, the peaks exist as broad, poorly resolved bands between 55 and 70 °C. The peaks become sharper at 70 °C, the same temperature at which the SAXS peak disappeared and the photoluminescence was

(a)

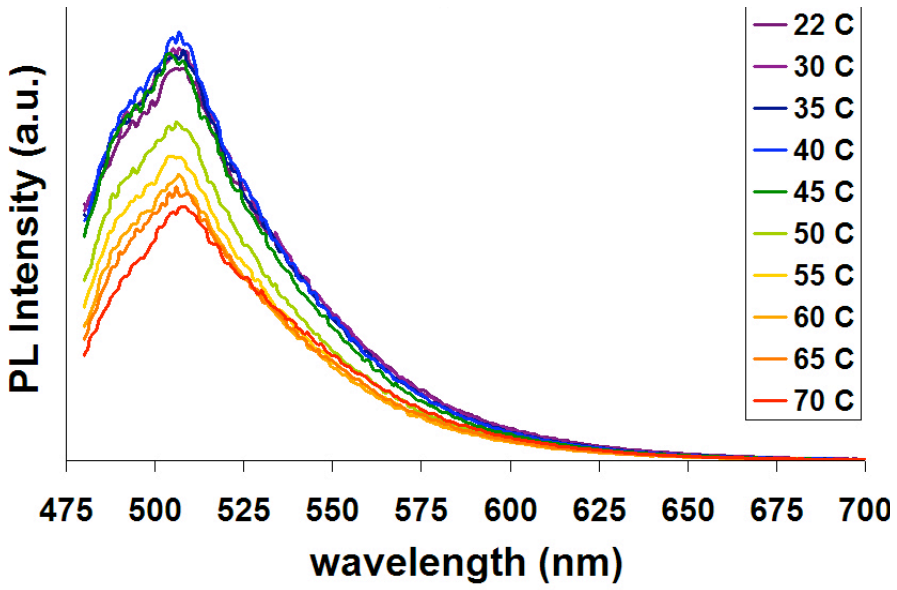

(b)

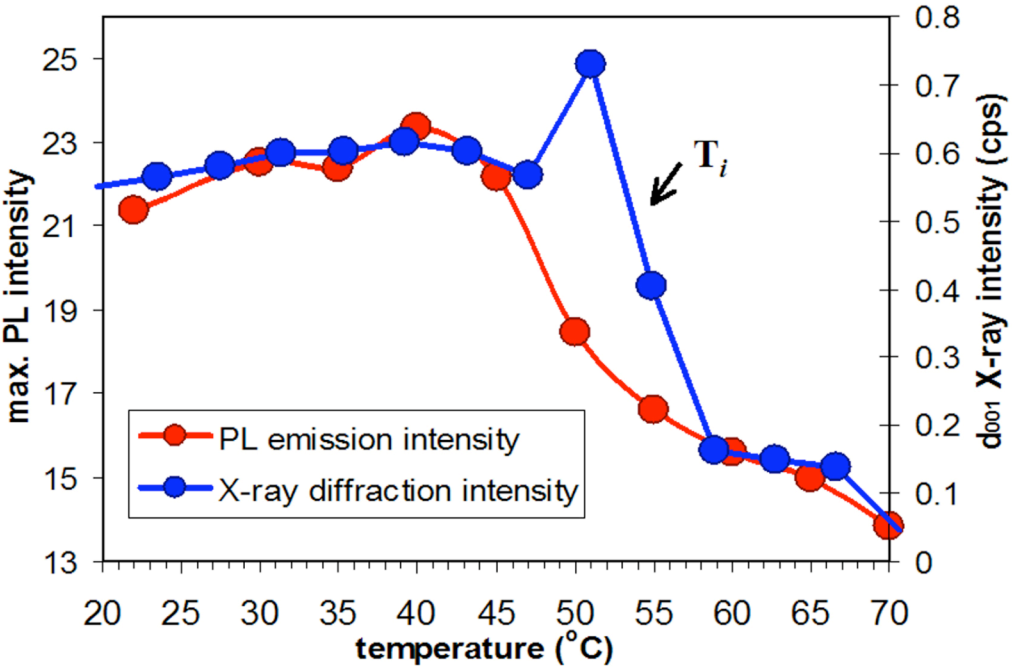

Figure 2.7. **(a)** Variable-temperature PL spectra of 40 wt% OPV-PEG-45 amphiphile in CH_3CN (ex. 475 nm). **(b)** Maximum PL intensity and X-ray intensity of $d_{(001)}$ peak as a function of temperature with arrow identifying isotropization point (T_i).

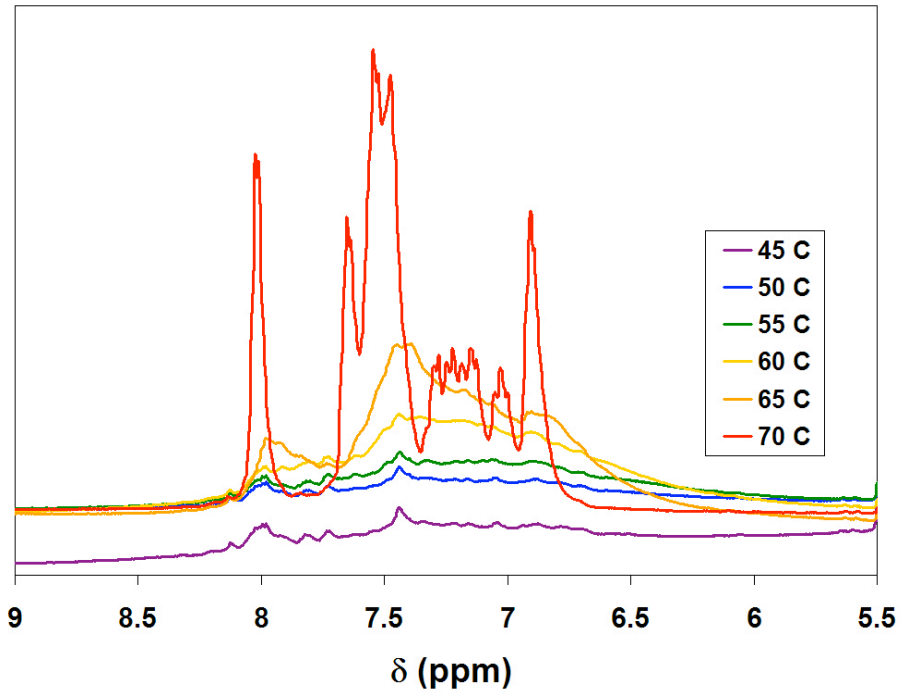

Figure 2.8. Variable-temperature ^{1}H-NMR of 40 wt% OPV-PEG-45 amphiphile in CD_3CN. (performed by Dr. Keisuke Tajima).

completely quenched. This result indicates a rise in proton T_1 relaxation times, and confirms the OPV aggregation in the isotropic state.

The molecular motion of these amphiphiles was further investigated by fluorescence polarization where the gel of the OPV-PEG-45 amphiphile in acetonitrile was excited with polarized light, and the polarization of the emitted light was measured. Only molecules with their transition dipoles parallel to the electric field vector of the incident light are excited. Polarization is (P) values range from -0.33 to 0.5, and are obtained by the following equation:

$$P = \frac{I_{parallel} - I_{perpendicular}}{I_{parallel} + I_{perpendicular}} \qquad (2.1)$$

where $I_{parallel}$ and $I_{perpendicular}$ are the fluorescence intensities parallel and perpendicular to the polarization of the incident light. In the case of the OPV-PEG-45 gel (see Figure 2.9), the maximum polarization value of 0.35 indicates that relatively little molecular rotation or exciton migration exist on the experimental timescale. The polarization remains constant with heating up to 70 °C where it decreases significantly to 0.14. In agreement with the NMR results, this observation further indicates even in isotropic solutions, molecular rotation is inhibited due to aggregation of the OPV.

The absence of any significant changes in the UV-Vis absorption (see Figure 2.10) as a function of temperature indicates that the photoluminescence emission behavior is not due to any changes in scattering and absorption by the molecules.

In investigating a different solvent system, a 40 wt% gel of OPV-PEG-45 in DMSO also exhibited lamellar ordering. In this case, however, while still forming a lamellar structure, the amphiphile crystallized at room temperature, and heating to 38 °C was necessary to attain a LC

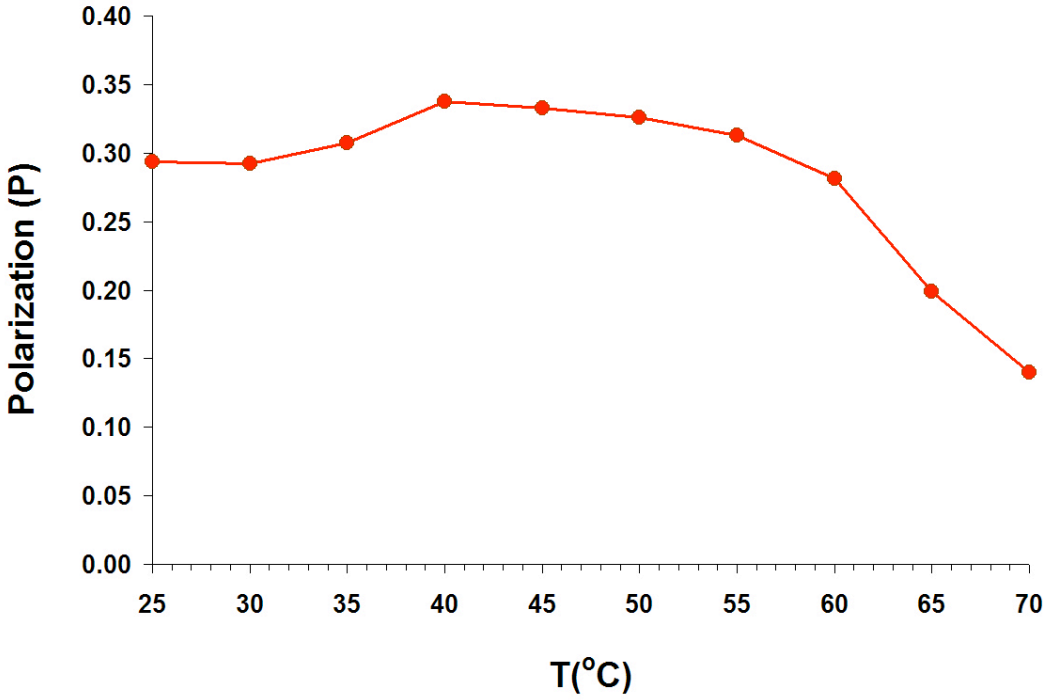

Figure 2.9. Fluorescence polarization of 40 wt% OPV-PEG-45 amphiphile in CH_3CN as a function of temperature (ex. 488 nm, em. 535 nm).

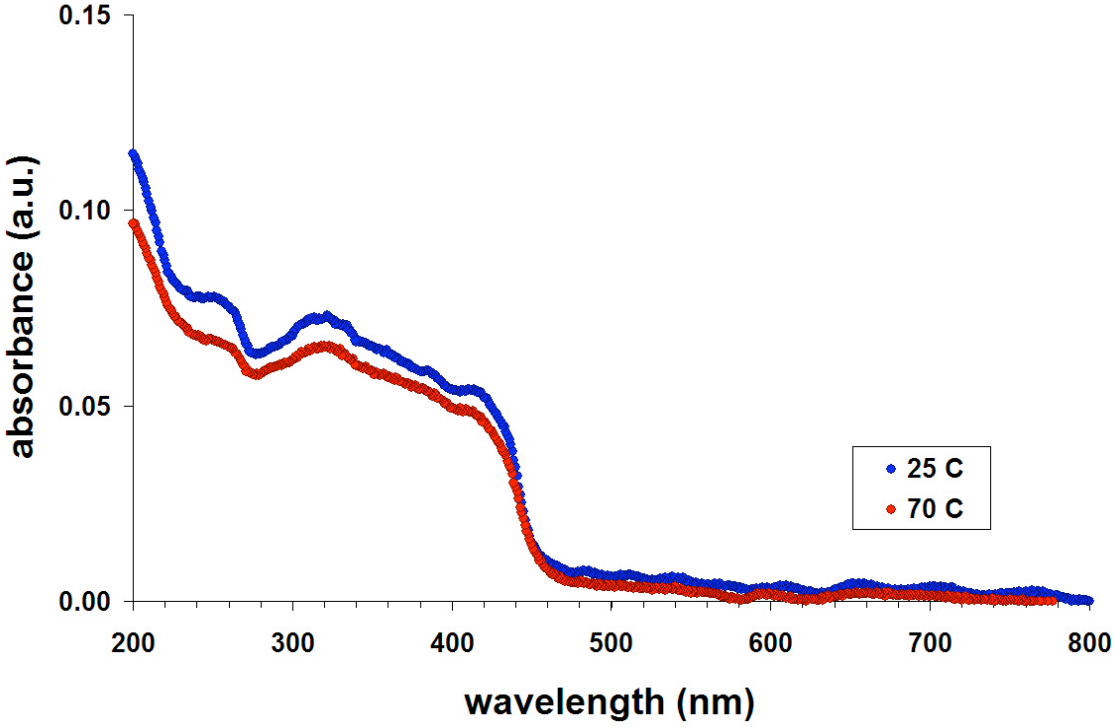

Figure 2.10. Variable-temperature UV-Vis absorption spectra of 40 wt% OPV-PEG-45 amphiphile in CH_3CN.

phase (see Figure 2.11), which then transformed to a disordered, isotropic solution above 68 °C. Coupled with this behavior, a four-fold increase in fluorescence and a 20-nm blue-shift was observed upon formation of the LC mesophase (see Figure 2.12), indicating a decrease in intermolecular interactions and π–π overlap, and hence, OPV confinement. Upon isotropization, the fluorescence returned to its previous room temperature level. This fluorescence behavior, as with all other temperature-dependent studies previously described, was fully reversible.

The dominance of the PEG block on the overall LC structure, is confirmed further by a concentration-dependent study of the OPV-PEG-45 in water. Below the critical micelle concentration (see Figure 2.13), the PL intensity of the OPV is directly proportional to concentration. Self-organized aggregates form at the CMC, as observed by the transition from clear to soapy solutions at 0.1 wt%. As such, the PL intensity also decreases above the CMC, as expected due to chromophore aggregation. Above the CMC, a vibronic shoulder at 505 nm is also observed, which reaches a maximum at 10 wt%. With LC mesophase formation at 30 wt%, this shoulder diminishes in intensity and the PL emission blue shifts toward the emission of the dilute solutions. This result further suggests that in the LC mesophase, the OPV layers are confined from one another, and therefore, intermolecular energy transfer is limited.

The LC mesophase's ability to form highly-ordered lamellar structures and control the aggregation state of the chromophores by confining them into discrete layers, makes it a suitable candidate to serve as a template or scaffold for the mineralization of a semiconducting inorganic phase within the hydrophilic channels. This is investigated in the following section.

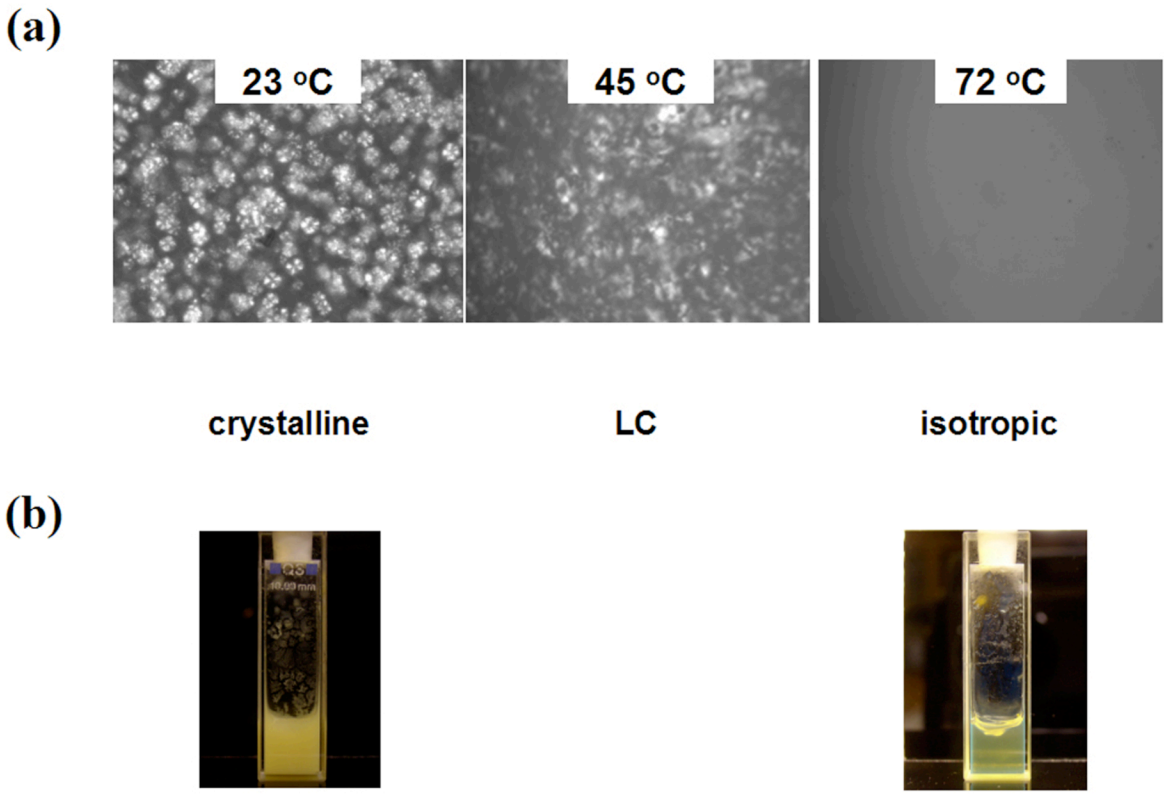

Figure 2.11. **(a)** Variable-temperature POM images of 40 wt% OPV-PEG-45 amphiphile in DMSO, in crystalline, liquid-crystalline, and isotropic states. **(b)** Photographs of vials of 40 wt% OPV-PEG-45 amphiphile in DMSO, at corresponding temperatures.

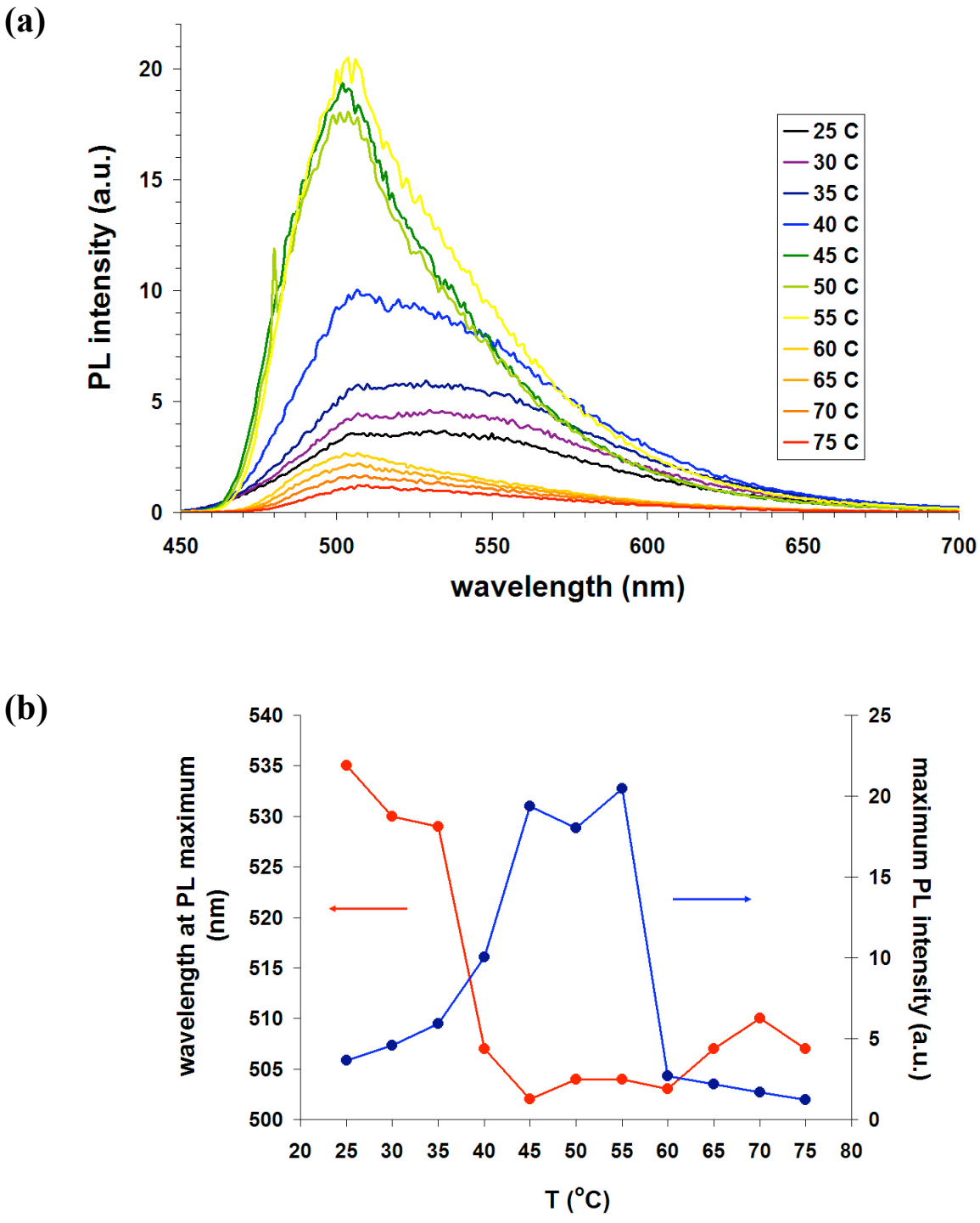

Figure 2.12. **(a)** Variable-temperature PL spectra of 40 wt% OPV-PEG-45 amphiphile in DMSO (ex. 375 nm). **(b)** Temperature-dependent behavior of PL emission wavelength (red) and intensity (blue). (Reproduced from Hulvat, J. F. et al., J. Am. Chem. Soc. **2005**, 127, 371 with permission, copyright American Chemical Society).

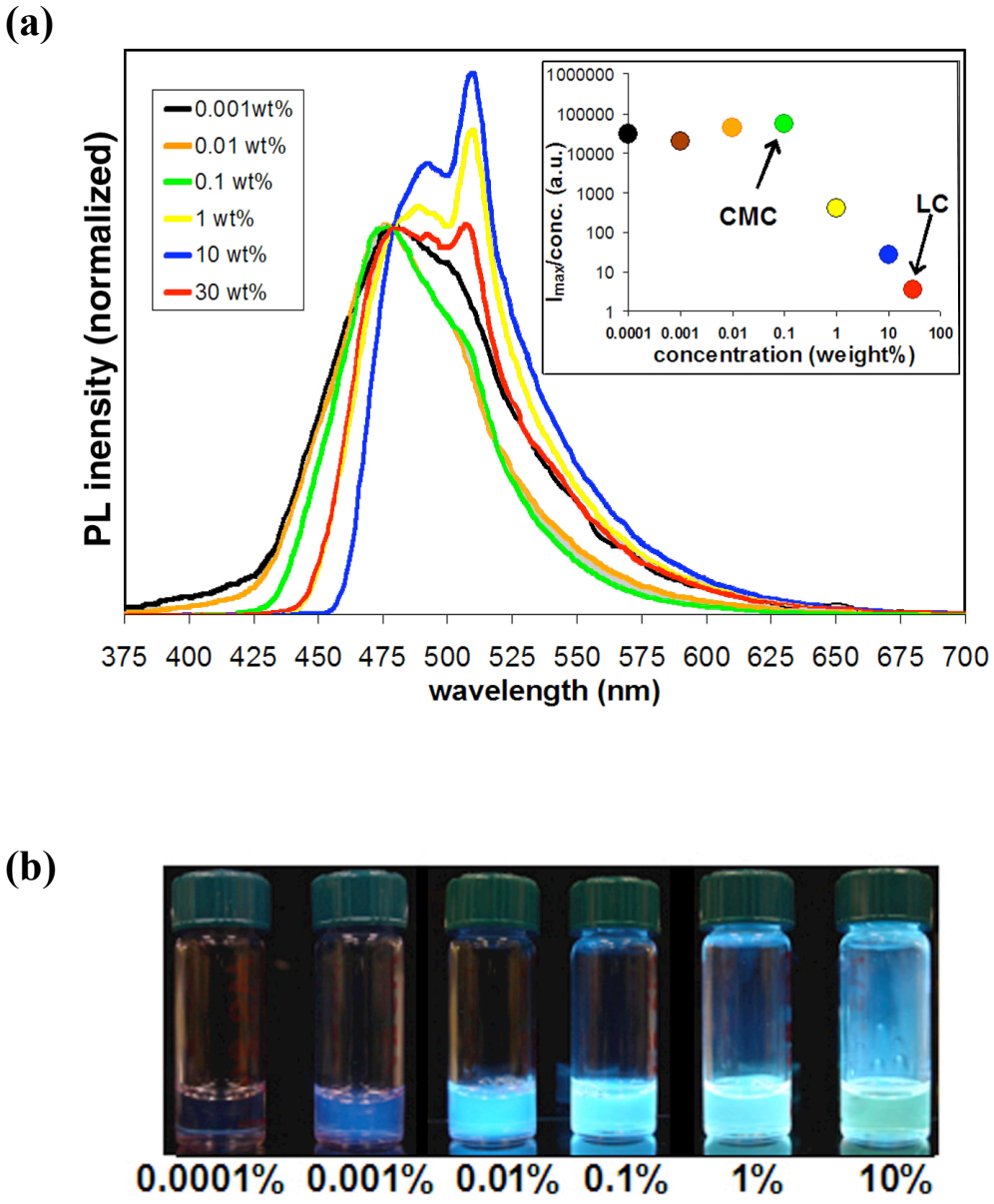

Figure 2.13. **(a)** Normalized PL spectra of aqueous OPV-PEG-45 solutions at various concentrations (ex. 325 nm) with inset showing concentration normalized PL intensity proportional to quantum efficiency of solution. **(b)** Photographs of vials of solutions under UV light illumination at concentrations designated from PL spectra. (Reproduced from Hulvat, J. F. et al., J. Am. Chem. Soc. **2005**, 127, 370 with permission, copyright American Chemical Society).

2.4 Zinc Oxide Synthesis

ZnO nanoparticles were synthesized by the sol-gel reaction of the precursor, diethylzinc (1.1 M in toluene). In order to stabilize and slow down the rapid hydrolysis of the precursor, anhydrous THF (64 vol%) was added to the solution to coordinate to the zinc. Hydrolysis and conversion to zinc hydroxide occur with exposure to air. Upon annealing at 150 °C, the hydroxide condenses to ZnO. The ZnO formed is crystalline and of the wurtzite phase (see Figure 2.14 (a)). The significantly broadened peaks are attributed to the finite size of the nanoparticles. According to the Debye-Scherrer relationship, particle size is inversely proportional to the width of the diffraction peaks.[111] As such, using the equation:

$$diameter = \frac{0.9\lambda}{B\cos\theta}, \quad B = FWHM, \lambda = 1.54\,\text{Å} \qquad (2.2)$$

the average particle size is calculated to be 5.3 $\pm$ 1.3 nm. The UV-Vis absorption (see Figure 2.14 (b)) also confirms the formation of ZnO with an absorption onset of 360 nm or 3.3 eV.

The synthesis of ZnO from the hydrolysis and condensation of diethylzinc was further investigated in the presence of the PEG amphiphiles with the assumption that the highly-moisture sensitive precursor would be attracted to the hydrophilic PEG, and therefore, hydrolysis and conversion of diethylzinc into ZnO could occur within the PEG channels of the lamellar mesophase. As such, the anhydrous THF was eliminated from the diethylzinc to promote its coordination to the PEG instead. For these studies, the oligothiophene derivatives (see Figure 2.2) were used due to their absorption beyond the 360 nm absorption onset of the ZnO, allowing for optical characterization of both the organic and inorganic phases. The oligothiophene-PEG-n amphiphiles formed similar lamellar LCs as the OPV-PEG-n amphiphiles.

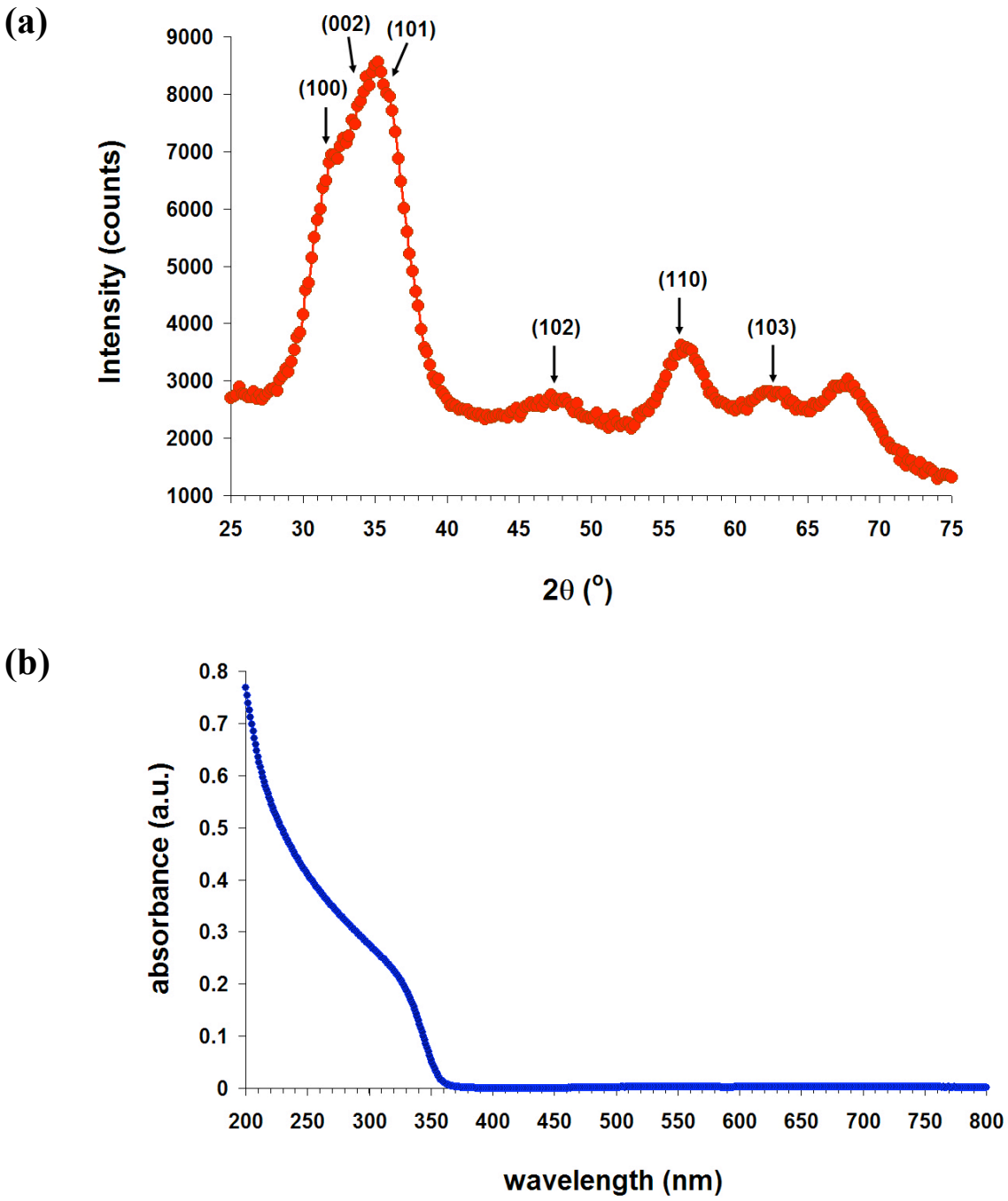

Figure 2.14. **(a)** Powder XRD pattern identifying wurtzite phase for ZnO film synthesized from diethylzinc precursor with subsequent annealing at 150 °C for 1 hr. **(b)** UV-Vis absorption spectrum for synthesized ZnO showing absorption onset of 360 nm.

Thin films were cast from concentrated aqueous solutions (above the CMC) of the oligothiophene-PEG amphiphiles. After air-drying, the films were annealed at 150 °C to remove any residual solvent and then slowly cooled to room temperature so that the thermotropic mesophase could reform. The isotropization temperature of the thermotropic LCs was observed at 140 °C, and therefore the heating and cooling was also used to increase the size of the LC domains. Because of the necessity for future device applications to use thin films, as well as a desire to use less amphiphile, thermotropic instead of lyotropic mesophases of the PEG amphiphiles were utilized for mineralization studies. In addition, the 5T-PEG-24 was preferred over the 5T-PEG-45 because the crystallization of longer PEG chains was observed to disrupt the overall lamellar packing in the thermotropic phases.[45] Exposure to the diethylzinc precursor solution was conducted in an air-free flask under argon. The precursor was hydrolyzed upon the film's exposure to air, and conversion to zinc oxide occurred by annealing at 150 °C for one hour under nitrogen.

2.5 Structural and Morphological Characterization of Hybrid Films

The presence and conversion of ZnO on the 5T-PEG-24 films is confirmed by UV-Vis absorption (see Figure 2.15). With increased exposure time, the ZnO absorption is apparent from the absorption onset at 360 nm and below. Further, the maximum absorption of the quinquethiophene at 380 nm is red-shifted to 400 nm. Due to the nature of the thin films, as well as the presence of the thiophene and small domain sizes, it was difficult to make any conclusions about the morphology of the ZnO from XRD.

Polarized optical microscopy of a mineralized film revealed the existence of birefringent textures at room temperature (see Figure 2.16). The relatively small size of these domains might

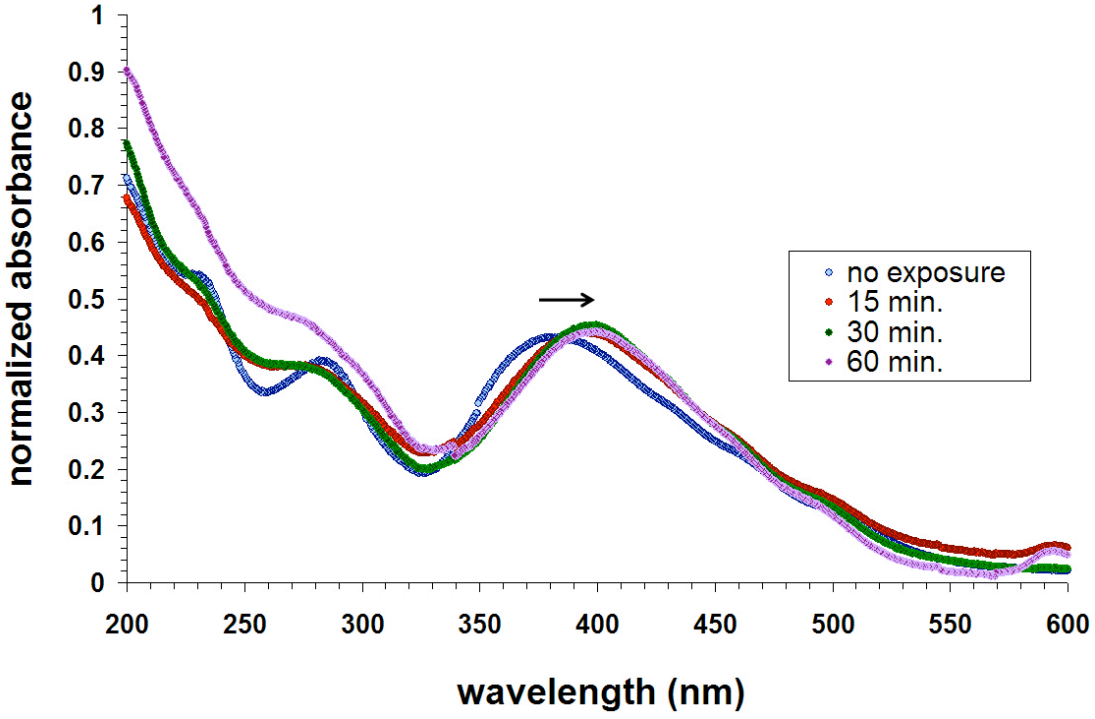

Figure 2.15. Normalized UV-Vis absorption spectra for 5T-PEG-24 films as a function of exposure time to diethylzinc for formation of ZnO.

be attributed to the disruption of long-range ordering from diethylzinc exposure and conversion. Upon annealing beyond the isotropization of the amphiphile, the birefrigent texture disappears and becomes isotropic and disordered. As is observed in the absence of the ZnO, the birefringent texture is recovered with cooling.

TEM imaging was used to determine whether or not the lamellar ordering is retained and the ZnO nanoparticles are formed within this template. In most instances, micron-size aggregates of ZnO are observed or nanoparticles in disordered arrangements (see Figure 2.17 (a)). No clear conclusions on ordering can be made from the images. The EDS line spectrum (see Figure 2.17 (b)), however, does show the presence of both sulfur, due to the thiophene, and zinc, due to the zinc oxide, indiating that both phases are present.

The diethylzinc precursor is extremely pyrophoric and the hydrolysis reaction is rapidly initiated in air. In previous syntheses of ZnO from diethylzinc, the films were kept in a controlled environment throughout hydrolysis and condensation with the relative humidity also controlled.[104] It is possible that performing both the mineralization and conversion in a glove box environment might provide better control over the rapid reaction and retain the LC structure. The temperature, however, at which the films are annealed for conversion of zinc hydroxide in zinc oxide (150 °C) is also just above the isotropization point of the thermotropic mesophase formed by the amphiphiles. Because the conversion is occurring at a temperature in which the LC has been disrupted, it is quite possible that when the LC is reformed upon cooling nanoparticles formed are trapped outside of this matrix.

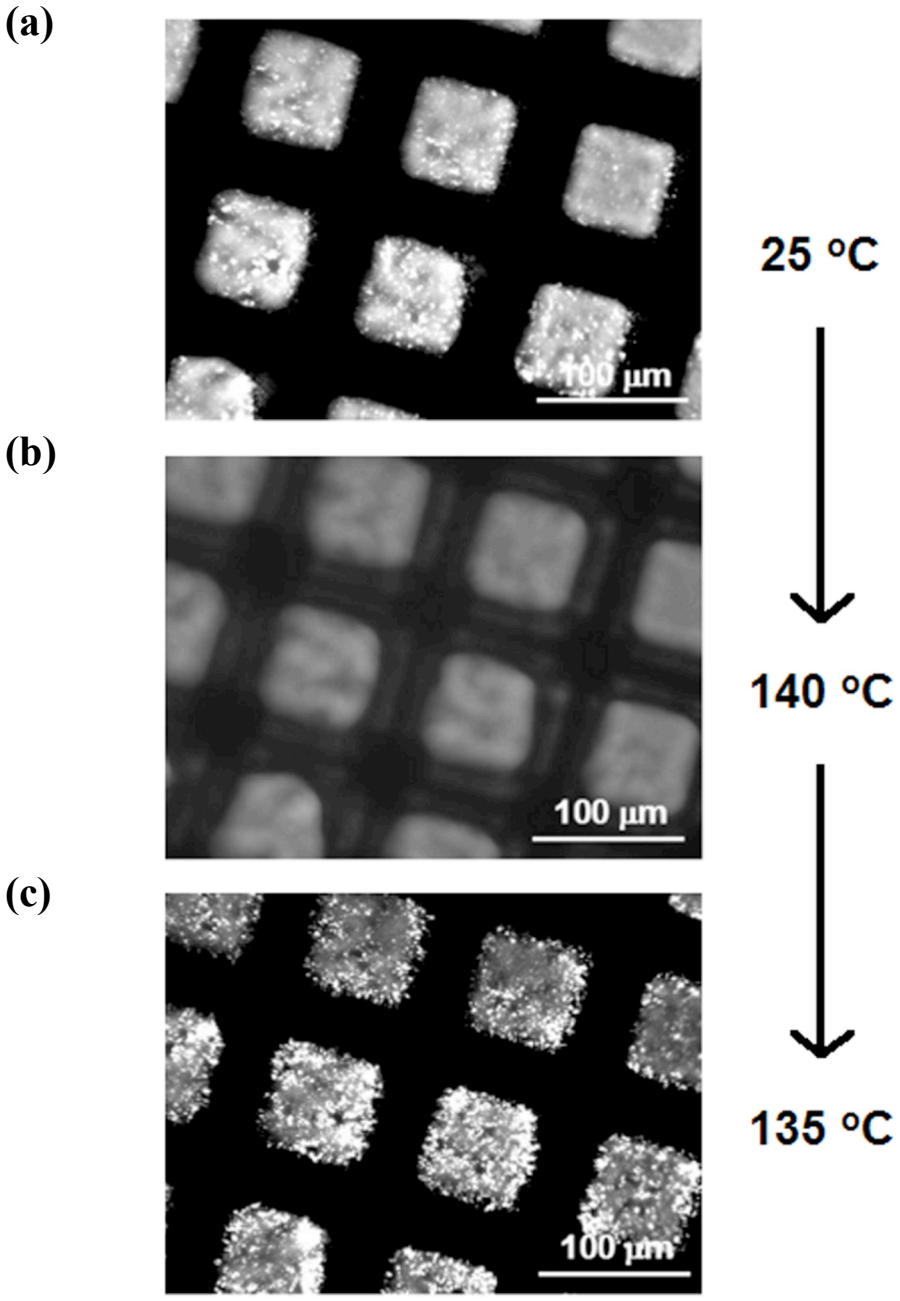

Figure 2.16. Polarized optical microscopy images of films of 5T-PEG-24, cast on TEM grids, after formation of ZnO (30 min. diethylzinc exposure) as a function of heating and cooling.

(a)

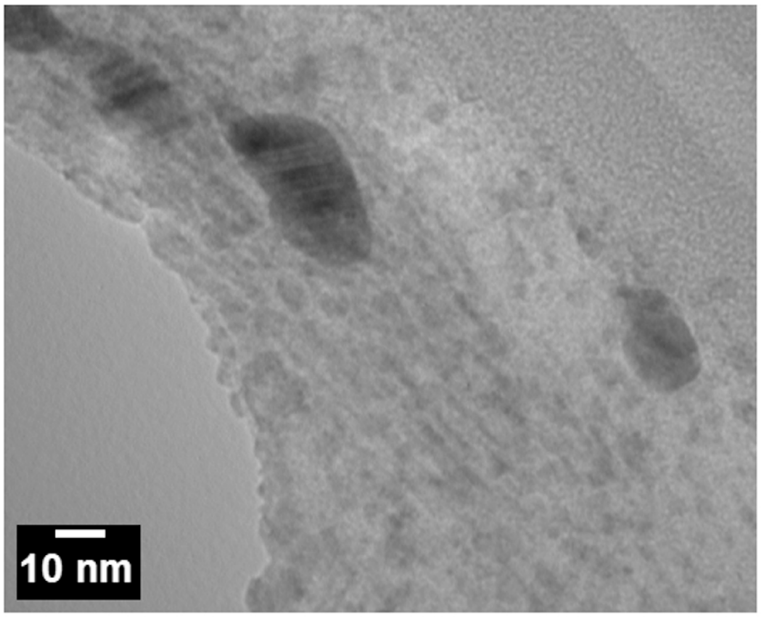

(b)

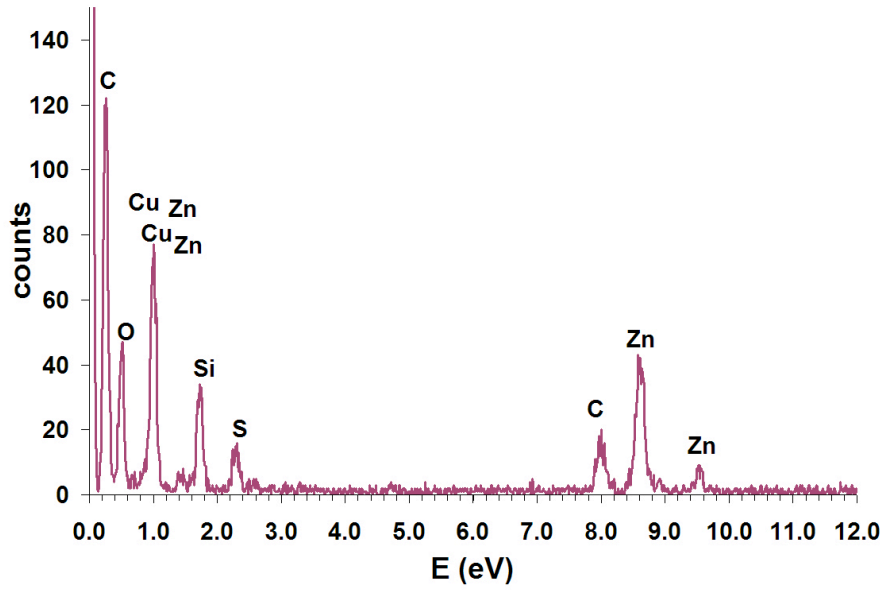

Figure 2.17. **(a)** TEM image of 5T-PEG-24 film upon formation of ZnO in-situ. **(b)** EDS spectrum of hybrid film.

2.6 Summary and Outlook

This chapter describes the synthesis of a series of non-ionic, water-soluble triblock amphiphiles containing either OPV or oligothiophene conjugated moieties. Due to their amphiphilicity, these molecules self-organize into liquid crystalline phases that exhibit lamellar ordering. This self-assembly of these molecules is further shown to directly control their optical properties. The dominance of the PEG block isolates and confines the chromophores layers from one another, leading to enhanced luminescence behavior and limited intermolecular energy transfer. The LC is therefore used as a template or scaffold in an attempt to mineralize a semiconducting inorganic phase (ZnO) within the hydrophilic channels. While the presence of water hinders the growth of the ZnO within the confines of the LC structure, the nanostructural ordering of the organic phase alone provides an in-depth understanding of the power of self-assembly in optimizing optolectronic properties by using oligomeric derivatives of surfactants with well-defined structure and end-functionalization. From the lessons learned in the chapter, the following two chapters investigate dynamic co-assembly approaches to mineral formation using electronically active, ionic oligomeric amphiphiles. Such amphiphiles are preferred in this scheme as PEG chains are expected to be poor units for direct charge transfer due to the presence of water and because of their sigma bonding.

2.7 Experimental

OPV-PEG-n amphiphiles were synthesized by Dr. Keisuke Tajima, of the author's laboratory. Oligothiophene-PEG-n amphiphiles were synthesized by David Stone, also of the author's laboratory. Characterization of the LC phases of the OPV amphiphiles were carried out

in close coordination with Dr. James Hulvat, also of the author's lab, who performed some of the experiments described above.

2.7.1 Organic synthesis and thermal characterization

Details of the synthetic approach for the OPV-PEG-45 amphiphile is provided in the literature. The details of the synthetic approach for the 5T-PEG-24 amphiphile is provided in Appendix I.1. Thermogravimetric analysis (TGA) perfomed on these molecules at 10 °C/min in air, using a TA Instruments 2920 DSC/TGA showed a decomposition onset by 200 °C for all amphiphiles. DSC was performed on the amphiphiles in gel-form with 10 mg of sample at heating and cooling rates of 5 °C/min. with two temperature cycles starting at 20 °C and going up to 5 °C below the solvent boiling point. Phase transitions were determined by using the second of the two cycles.

2.7.2 Zinc oxide synthesis

A film of oligothiophene-PEG-n was spin-cast from a concentrated aqueous solution (~30 mg/mL) onto an O_2 RIE-cleaned (5 min. on both sides at 100 W, 50 sccm O_2) glass substrate. After air-drying overnight, the sample was annealed at 150 °C for 1 hr. and slowly cooled down to room temperature to remove residual solvent and reform the thermotropic LC phase of the amphiphile. The substrate was inserted into an air-free 100 mL two-arm flask, and sat on a copper wire holder, hanging vertically from one arm at ~ 85 mm above the flask bottom. The flask was dried further and remained under argon atmosphere during mineralization. As much as 0.5 mL of diethylzinc (1.1 M solution in toluene, Sigma-Aldrich) was then injected through the second arm into the bottom of the flask. After the elapsed exposure time, the substrate was removed from the flask in air and then annealed at 150 °C for 1 hr. for conversion

of ZnO. When anhydrous THF was added to diethylzinc to slow down hydrolysis, the two solutions were mixed under nitrogen prior to injection in the flask.

2.7.3 Optical microscopy

A Leitz Laborlux 12POL polarizing microscope was used with an attached Sony XC-ST-70 CCD camera. For the lyotropic LC studies, a small amount of gel was squeezed between glass slides, sealed and separated by a 75 μm plastic spacer. All samples were subsequently heated to isotropization and cooled under N_2 using a temperature-controlled stage at a rate of 0.3 °C/min, in order to obtain identifiable liquid crystalline textures.

2.7.4 X-ray Scattering

SAXS was performed using a Rigaku CuKα source (30 kV, 17 mA) with 2D Bruker CCD detector calibrated with silver behenate. Gels were sealed in 1.5 mm-diameter quartz capillary tubes. To insure proper loading and full mixing, concentrated solutions (< 10 wt%) were pipetted into the capillary and then solvent was slowly evaporated to chosen concentration. For temperature-dependent scans, samples were placed in a temperature-controlled heating stage with a Pt thermocouple and digital temperature controller attached to a thermistor and a water-cooled Cu heating block. Temperature readings were equilibrated for 5 min. before each scan.

2.7.5 UV-vis and PL spectroscopy

All LC gels samples were prepared by pipetting a concentrated solution and slowly evaporating the solvent to achieve a 40 wt% amphiphile concentration. For temperature-dependent studies, holders were sealed with Teflon to prevent evaporation and allowed to equilibrate for 10 min. at each temperature prior to measurement.

UV-vis absorption was recorded on a Cary 500 UV-VIS-NIR in double beam mode. For LC gels, ultra-short (10 μm) path length quartz holders (Starna, Inc.) were used for adequate transparency.

PL spectra were recorded on a PC1 Spectrofluorometer in right angle geometry using monochromators with a FWHM of 8 nm for both the excitation and emission. 1 mm path length quartz cuvettes (Starna, Inc.) were used.

Fluorescence depolarization was performed on a Beacon 2000 Fluorescence Polarization System using fluorescein filters (488 $\pm$ 6 nm ex., 535 $\pm$ 12 nm em.). The gel was sealed in a 6 x 50 mm glass tube.

Variable-temperature ^{1}H-NMR was performed on a Varian Unity 400 (400 MHz) spectrometer using the solvent proton signal as a standard.

2.7.6 TEM

TEM samples were made using two procedures. In the first, lacey formvar/carbon 300 mesh Cu grids (Ted Pella, Inc.) were used to gently contact the grid with the carbon-coated side face down over the deposited film for transfer. In the second, formvar/silicon monoxide 300 mesh Cu grids (Ted Pella, Inc.) were used for added durability during handling to directly grow the film onto the grid. The ends of the grid were adhered with double-sided tape onto the clean substrate (silicon monoxide-coated side face down) prior to film deposition and then gently lifted off after film growth. Samples were imaged at 200 kV on a Hitachi HF-2000 TEM and a Hitachi H-8100 TEM. Images were recorded using a Gatan CCD camera. EDS line scans were performed using the Inca Software.

CHAPTER THREE

Evaporation-Induced Self-Assembly of Silica and Conjugated Cationic Amphiphiles

Chapter 3: Evaporation-Induced Self-Assembly of Silica and Conjugated Cationic Amphiphiles

3.1 Introduction

Evaporation-induced self-assembly (EISA) offers a particularly efficient avenue towards achieving highly-ordered hybrid mesophases with nanoscale periodicity.[86, 87, 112] Originally inspired by the work of the Mobil Corp. in producing mesoporous silica,[5, 6] this dynamic co-assembly approach involves the mixing of organic amphiphiles, at concentrations below their critical micelle concentration, with inorganic precursors, in dilute homogenous solutions. Under sol-gel conditions used to synthesize the inorganic phase, the precursors will interact with the amphiphiles due to electrostatic interactions. As conversion to the inorganic phase takes places and the solution is cast into a thin-film, the preferential evaporation of solvent and resulting concentration gradient induces the self-organization of a highly-ordered and nanostructured hybrid.[113, 114] The organic amphiphiles, used solely as structure-directing agents, were traditionally removed and the remaining mesoporous inorganic used for applications such as catalysis.

The facile and powerful nature of EISA in producing such highly-ordered hybrid nanostructures with intimate contact between the two phases, however, has naturally led researchers to add function to the organic component as well. The versatility of EISA has been demonstrated, for example, by introducing polymerizable surfactants.[115-118] Extending into the realm of electronic applications, for the purpose of enhancing the fluorescence properties in hybrid materials, nonionic conjugated surfactants,[119-121] as well as very low concentrations of charged conjugated surfactants[122] have recently been incorporated into EISA systems.

The author's group recently exploited the utility of EISA by designing electronically active bolaamphiphiles to generate hybrid materials for energy transfer applications.[123] The amphiphiles consist of an oligo(p-phenylene vinylene) (OPV) trimer moiety symmetrically substituted at the para position with a short alkyl tail terminated with a trimethylammonium bromide group. Similar bolaform OPV amphiphiles for the fabrication of organic light emitting diodes (OLEDs),[124] as well as bolaform sexithiophene amphiphiles[125-127] have been reported, but were used in multi-step layer-by-layer assemblies rather than a one-step EISA process. The high solubility of the reported amphiphiles in polar solvents allows for EISA to occur with the electronically active OPV as the lone surfactant without the need for dilution with non-conjugated surfactants. The molecular architecture of the amphiphiles discussed in this chapter differs from that of amphiphiles typically used in EISA systems because it includes the use of positively charged head groups at both termini of the molecule as opposed to the common surfactant with a charged head group at only one terminus. As such, its symmetric structure also differs from the asymmetric nature of the other previously reported conjugated surfactant systems.[119, 120, 122]

Initial studies on energy transfer of these self-assembling hybrids showed nanoscale ordering, however, the resulting nanostructure was not fully characterized.[123] In EISA systems, structural characterization by X-ray techniques is used to gain a better understanding of the process itself, as well as to optimize conditions and tune the final mesostructure for specific applications. Grazing-incidence X-ray scattering (GIXS) is a powerful and non-destructive technique which is used to identify the in-plane,[128] as well as out-of-plane structure of thin films, and has therefore been used to characterize EISA-formed nanostructured films.[113, 114, 129-131] In

this chapter, the nanoscale structure of these hybrid systems is characterized using GIXS as well as specular X-ray reflectivity (XRR) and powder X-ray diffraction (XRD). Two different systems are investigated, one is the previously reported silica-OPV amphiphile hybrid, and a second one containing silica and a bolaamphiphile with a more conductive tetrameric oligothiophene as the conjugated segment.

3.2 Syntheses of Cationic OPV and Oligothiophene Bolaamphiphiles

3.2.1 Cationic OPV bolaamphiphile synthesis

The cationic OPV bolaamphiphile described here was synthesized by Dr. Keisuke Tajima, of the author's laboratory, with details of the synthesis published elsewhere.[123] The synthetic scheme, outlined in Figure 3.1, uses the Horner-Wadsworth-Emmons reaction for the formation of *trans*-vinyl bonds in the OPV trimer core and subsequent alkylation of the tertiary amines to the quaternary ammonium salts. The overall yield for the four-step reaction is ~41%.

3.2.2 Cationic oligothiophene bolaamphiphile synthesis

The cationic quaterthiophene bolaamphiphile described was synthesized by David Stone, of the author's laboratory. The synthesis and reaction conditions are shown in Figure 3.2 and described in detail in Appendix I.2. Briefly, a Stille reaction is used for the formation of the quaterthiophene core and subsequent alkylation of the tertiary amine to form tetramethylammonium salts. The overall yield for the four-step reaction is ~46%.

3.3 Self-Assembly of OPV Bolaamphiphile

3.3.1 The neat uncharged precursor

The uncharged precursor to the OPV bolaamphiphile **3**, as shown in Figure 3.1, contains dimethylamine groups on both termini and was used to investigate the role of charge on

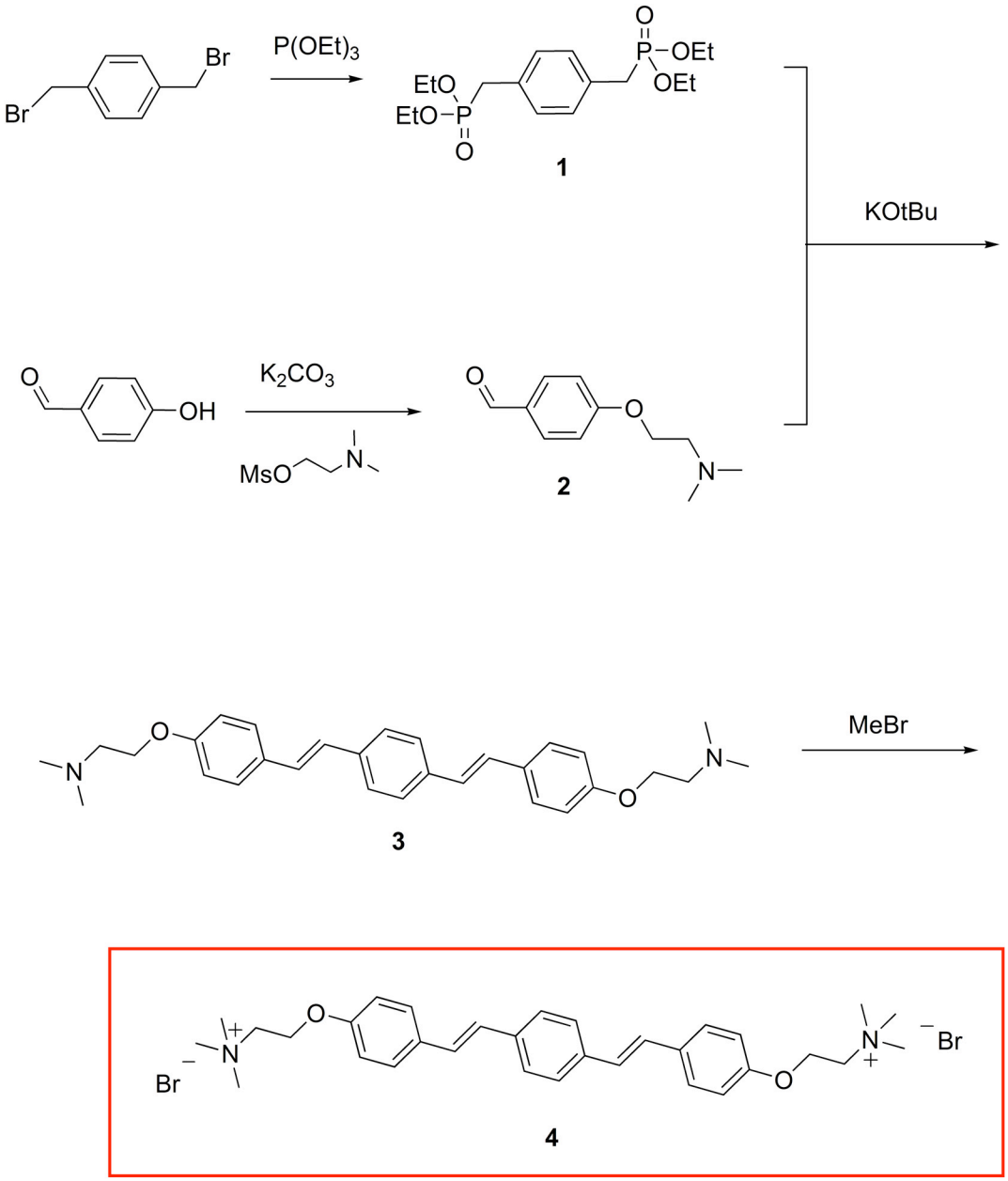

Figure 3.1. Chemical synthetic scheme for cationic OPV bolaamphiphile. The four step reaction has an overall yield of ~41%. (prepared by Dr. Keisuke Tajima)

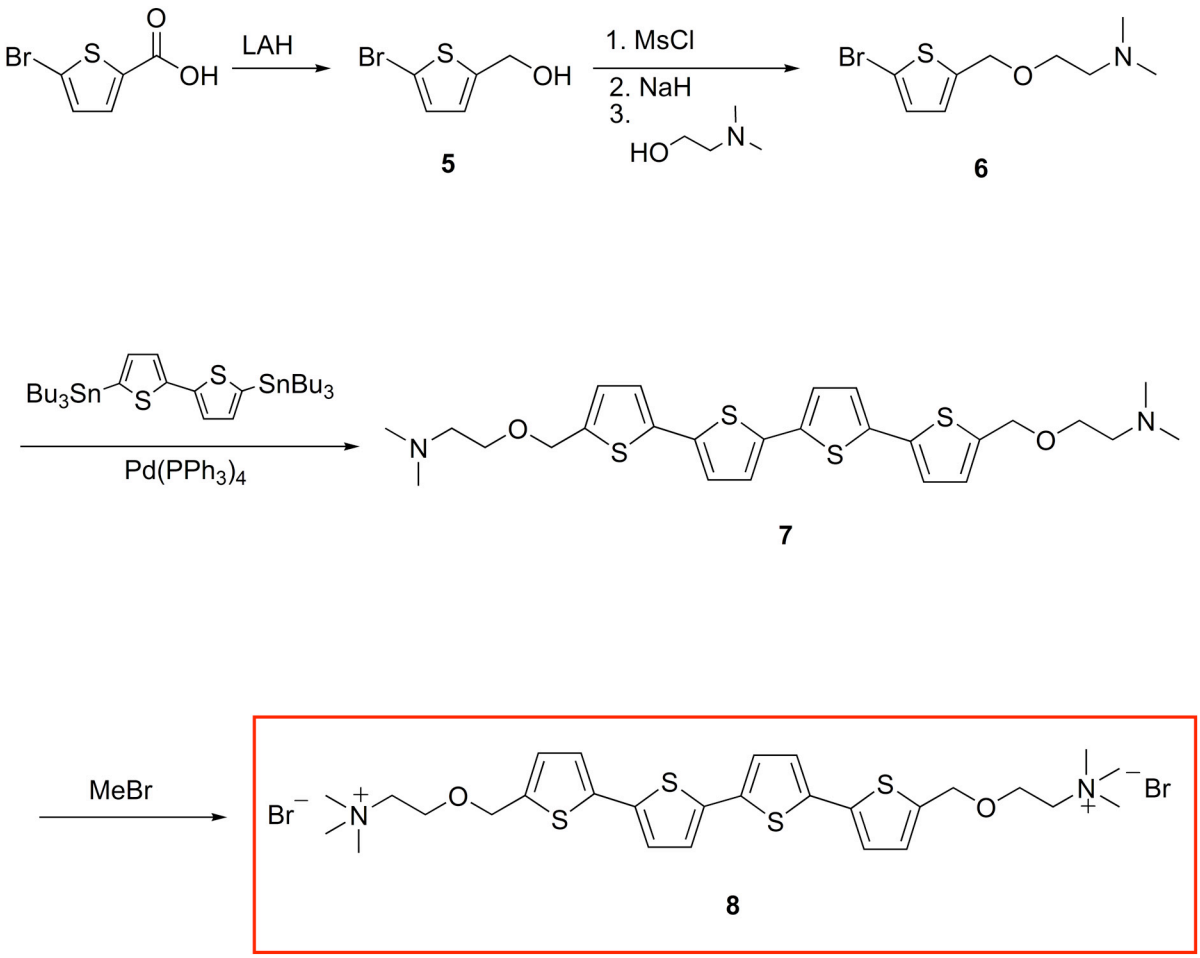

Figure 3.2. Chemical synthetic scheme for cationic quaterthiophene bolaamphiphile. The four step reaction has an overall yield of ~46%. (prepared by David Stone)

molecular packing. The SAXS pattern (Figure 3.3) of the uncharged OPV in its neat form indicates the formation of a lamellar structure with *d*-spacings of 2.71 nm, 1.36 nm, and 0.91 nm corresponding to (001), (002) and (003) reflections, respectively. A layered packing of the molecule, as shown in Figure 3.4 (a), is further suggested by the first-order peak which is slightly larger than the fully extended length of the molecule between the two nitrogen atoms (2.5 nm). Attempts to cast a film of the molecules from solution were unsuccessful due to insolubility in organic solvents at sufficient concentrations. The WAXS pattern (see Figure 3.5) reveals several sharp peaks, with the most dominant at 4.4 angstroms, indicating strong π–π stacking interactions, which are one of the major driving forces towards the highly-ordered layered structure that molecule **3** self-organizes into.

3.3.2 The neat cationic derivative

The addition of charges to the end groups of the molecules, leads to the collapse of the previously observed lamellar packing in the uncharged derivative. As shown in Figure 3.3, the cationic OPV bolaamphiphile **4** only generates an extremely faint peak almost two orders of magnitude weaker in intensity than the first-order peak of the uncharged analog at 2.1 nm. This peak corresponds roughly to the distance between the alkyl chains on either end. This observation strongly suggests that repulsion between like charges disrupts long range ordering of the molecules. The widths of the peaks in the bis-tertiary amine indicate that domains of uncharged molecules are larger than those of the cationic amphiphile. The results therefore suggest that the single lone broad peak for the cationic amphiphile **4** is due to weak ordering from small domains. The weak ordering is most likely due to the small fraction of rigid cores that are able to π-stack in the presence of the charged groups at the termini of molecules as

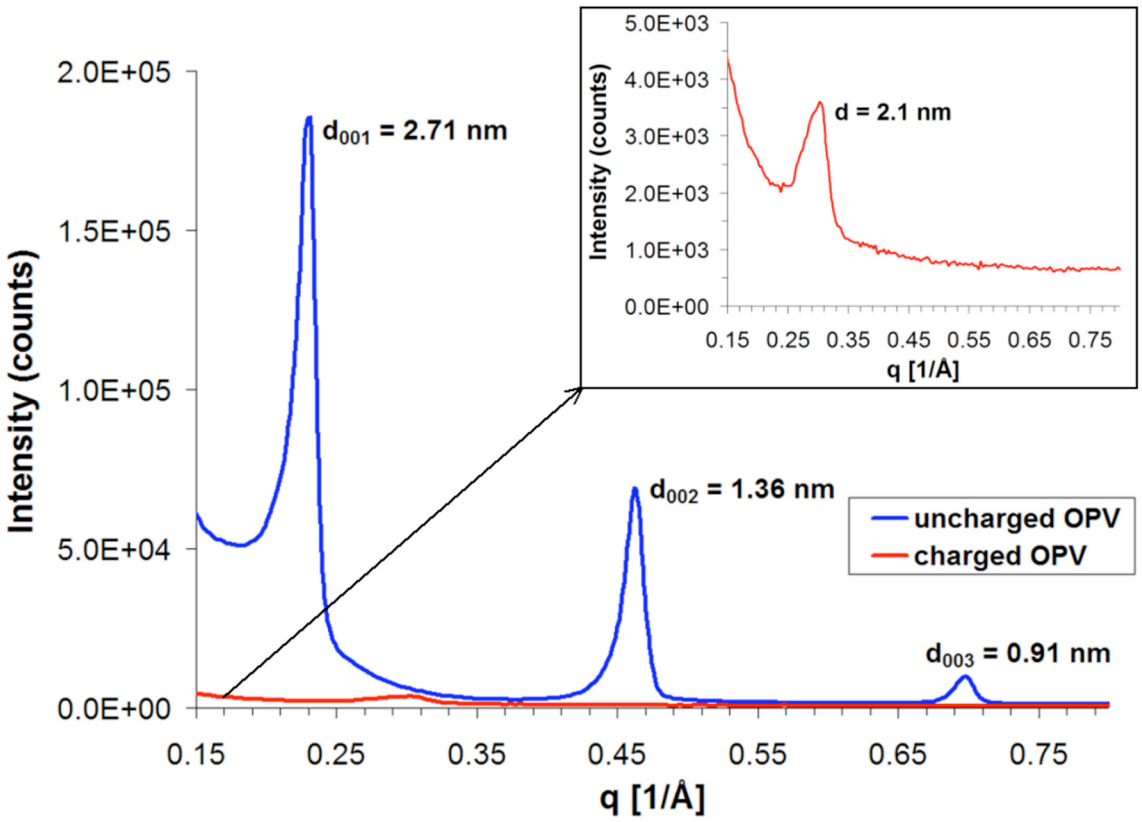

Figure 3.3. Small-angle powder X-ray diffraction of the neat uncharged precursor of the OPV bolaamphiphile **3** (blue line) and of the neat cationic OPV bolaamphiphile **4** containing positively charged termini and bromine ions (red line). Inset shows magnified view of spectrum of cationic derivative.

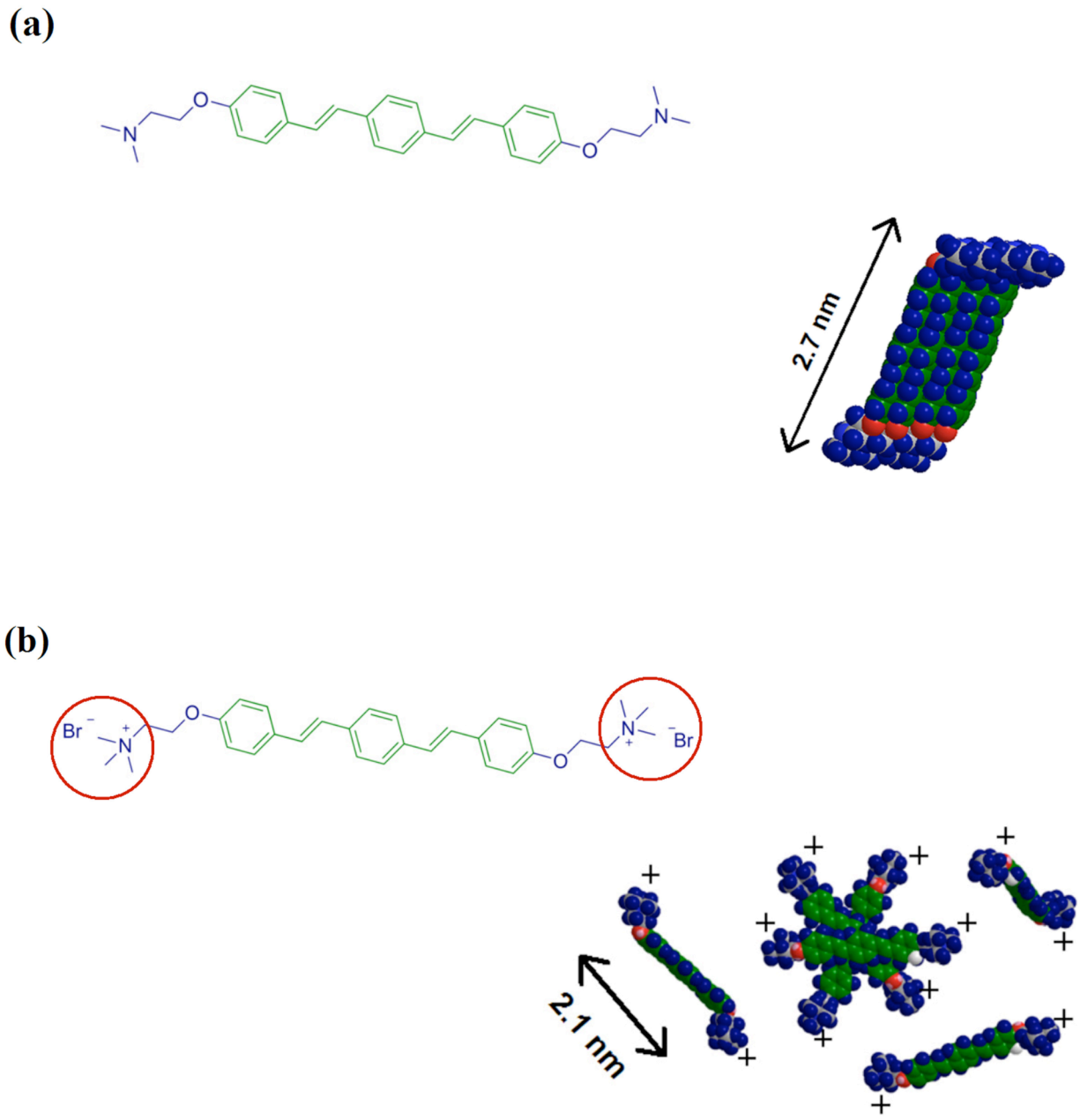

Figure 3.4. Chemical structures (left) and molecular graphics visualizations of molecular packing (right) based on SAXS patterns. **(a)** Neat uncharged OPV bolaamphiphile **3**. **(b)** Neat cationic OPV bolaamphiphile **4**.

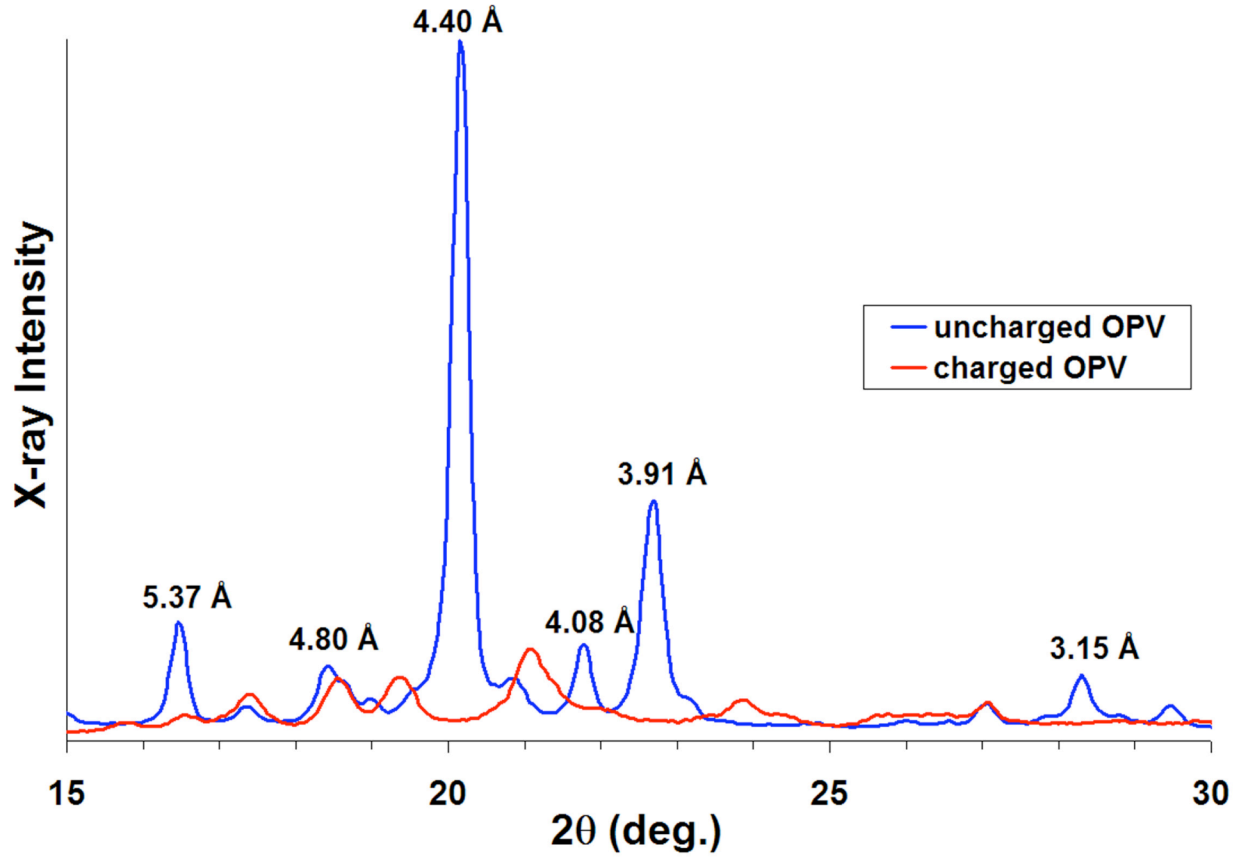

Figure 3.5. Wide-angle powder X-ray diffraction of the neat uncharged precursor of the OPV bolaamphiphile **3** (blue line) and of the neat cationic OPV bolaamphiphile **4** containing positively charged termini and bromine ions (red line).

depicted in Figure 3.4 (b). Bolaamphiphiles containing quaternary ammonium salts have been reported that exhibit thermotropic LC ordering, however, in those cases the hydrophobic core contained a long alkyl chain and no conjugation, which allowed for more flexibility in the molecules to screen charges from one another.[132] It is suggested, therefore, that a short and rigid conjugated hydrophobic block cannot overcome the electrostatic repulsion present. In the case of the cationic OPV **4**, the WAXS pattern in Figure 3.5 further suggests that electrostatic repulsion affects the π–π stacking interactions between the OPV chromophore segments of molecules. Similar to the results in the small-angle regime, the peaks present in the WAXS spectrum are fewer, weaker in intensity, and broader in comparison to the observed peaks in the uncharged OPV.

A film was cast of the cationic OPV amphiphile **4** from a solution at a concentration of 9.0 mM in methanol. Specular XRR was used to probe the periodicity along the surface normal q_z axis of the film. The specular reflectivity of this film, which is sensitive to planes parallel to the surface, lacks any Bragg peaks (see Figure 3.6 (a)). Well-ordered Kiessig fringes are evident above the critical angle of the glass substrate (q_c = 0.032 Å^{-1}), indicating a smooth and uniformly homogeneous film. Total external reflection occurs below the critical angle of the glass, or the point where the intensity begins to rapidly decrease. The dip before this critical angle represents the critical angle of the film, or the film refraction correction for the material, which in the case of the OPV is q_{fc} = 0.0275 Å^{-1}. The Kiessig fringes, which result from the interference between the different interfaces reflected along the surface normal direction (see Figure 3.6 (a)), are used to determine the overall film thickness:[133]

$$t_{film} = 2\pi / \Delta q_z \qquad (3.1)$$

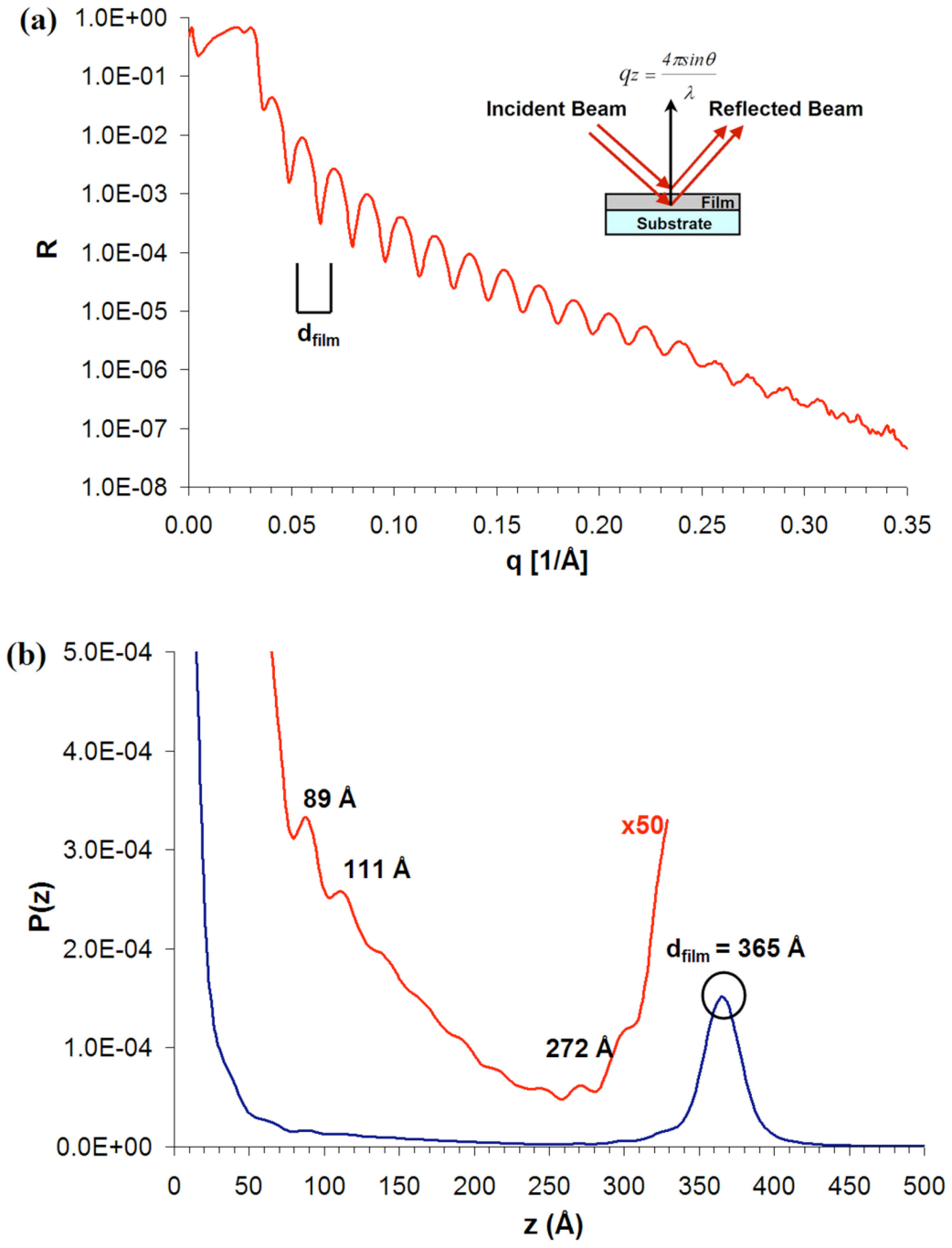

Figure 3.6. **(a)** Specular XRR of film cast from neat cationic OPV bolaamphiphile **4** with inset showing XRR experimental set-up and geometry. **(b)** Resulting Patterson map with red curve showing a magnified view.

where Δq_z is the periodicity between fringes. The overall film thickness, therefore, is calculated as 37 nm.

The Patterson function, P(z) (Fourier transform of the reflectivity normalized by the Fresnel reflectivity for an ideally flat glass mirror) is shown in Figure 3.6 (b). The observed peaks correspond to the distances between any two interfaces which are sensed by a change in electron density.[134, 135] The periodicity of the Kiessig fringes matches the peak corresponding to the overall film thickness (37 nm) in the Patterson map. It is also clear from the Patterson map in Figure 3.6 (b) that the cationic OPV amphiphile also does not form a highly ordered structure in film-form. Only a few peaks exist with a roughly 2.2 nm distance separating them that might correspond to the length of the molecule between the two oxygen atoms. However, this ordering is not very pronounced and does not occur throughout the entire film.

3.4 Evaporation-Induced Self-Assembly of Hybrids and Energy Transfer

In order to produce novel hybrid films with electronic function, the cationic conjugated bolaamphiphiles were used to mineralize silica by the EISA technique. As shown in the schematic in Figure 3.7 (a), the silica precursor, tetraethyl orthosilicate (TEOS) was added to 9.0 mM solutions of the bolaamphiphiles in methanol. An acid catalyst, HCl, was used to initiate the hydrolysis of the TEOS in a controllable fashion and the solution stirred for half an hour at room temperature. Given the positively-charged nature of the bolaamphiphiles, the hydrolyzed silica precursors are expected to interact with the ends of the surfactants. As is typical of the EISA process, the sol-gel reaction proceeded with subsequent condensation of the precursors into silica (see Figure 3.7 (b)) upon spin-casting of the solution into a thin film and further solvent drying to form an ordered nanostructure.

(a)

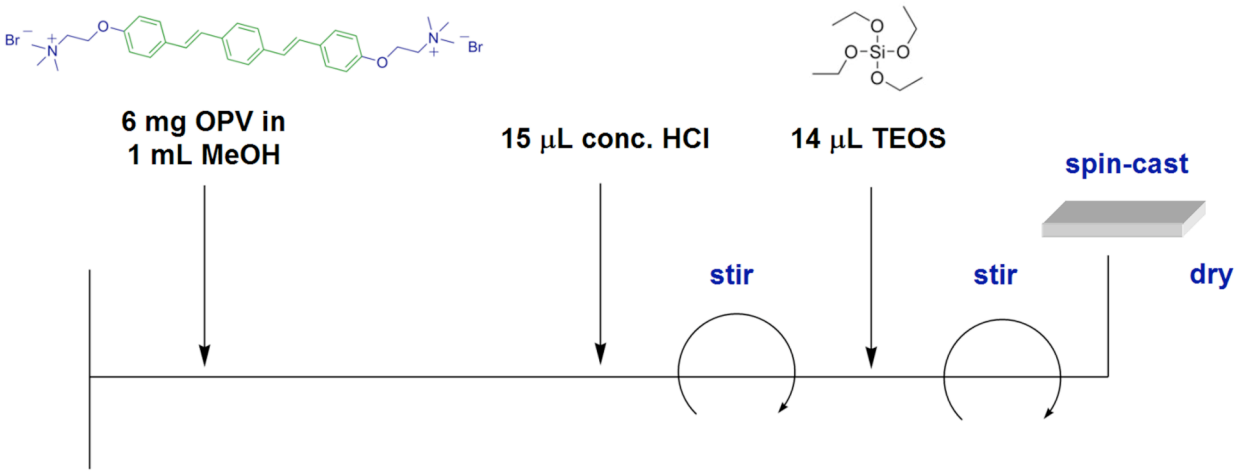

(b)

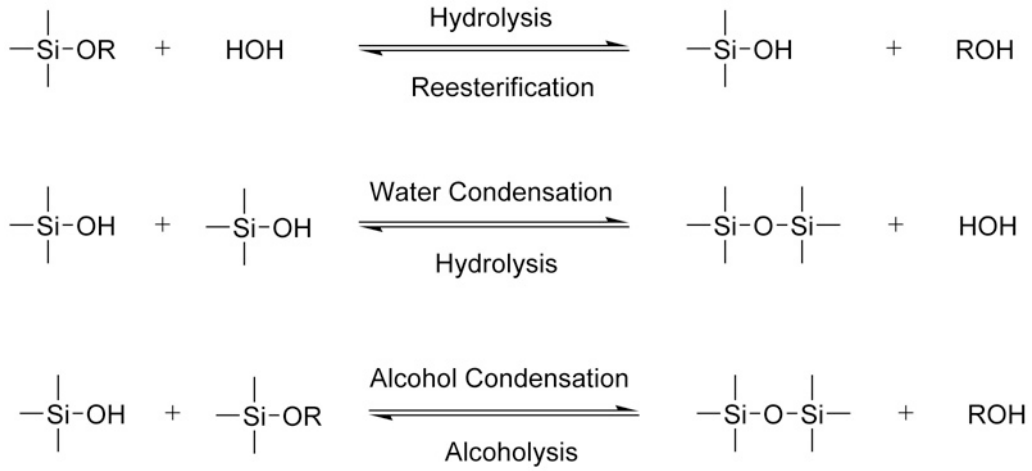

Figure 3.7. **(a)** Experimental schematic of EISA process using the cationic OPV bolaamphiphile as the structure-directing agent and TEOS as the silica precursor for mineralization. **(b)** Chemical synthetic scheme of sol-gel reaction of TEOS during mineralization process.

The EISA process using these conjugated bolaamphiphiles was further utilized to spatially arrange donor and acceptor molecules to promote energy transfer.[123] The silica precursor TEOS was substituted with a triethoxysilane group covalently attached to the acceptor molecules, a rhodamine B dye derivative, as shown in Figure 3.8. The cationic OPV derivatives were used as donor molecules and the rhodamine dye was expected to be incorporated selectively into the periodic silica network of the films during the course of the sol-gel process by simply mixing the dye molecules into the precursor solution as described above. As a result, the energy transfer from the OPV segments in the organic domains to the dye molecules embedded in the silica network was significantly enhanced as compared to a film prepared under non-assembly conditions and lacking any nanoscale ordering. When the hybrids are irradiated near the absorption onset of the OPV trimer (λ = 365nm), the film prepared by EISA appears red, indicating emission from the rhodamine dye (Figure 3.8). In contrast, with the same 2 mol% amount of rhodamine dye added, the amorphous film where the silica is substituted for poly(2-hydroxyethyl methacrylate) (PHEMA), remains blue. A more detailed and quantitiative investigation of the enhanced energy transfer properties of these hybrids films are further described and published elsewhere.[123] The focus of the remainder of this chapter, therefore, is on the investigation of the nanostructure, produced by EISA, of these films.

3.5 Structural Characterization of Hybrid Films

3.5.1 Grazing-incidence X-ray Scattering

In the initial structural characterization of the OPV/silica hybrid during the energy transfer investigation, specular X-ray reflectivity yielded first- and second-order Bragg peaks corresponding to *d*-spacings of 2.76 and 1.37 nm.[123] It was proposed that these two out-of-plane

(a)

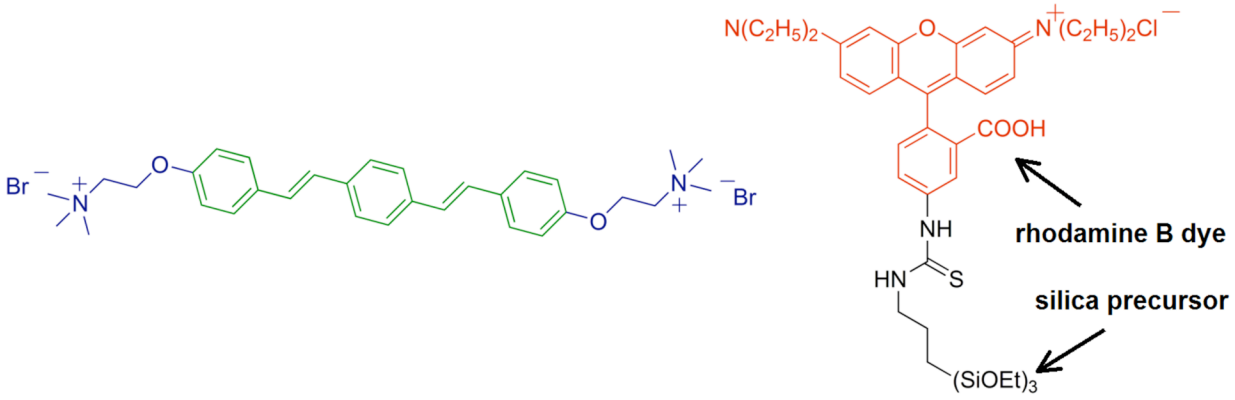

(b)

Figure 3.8. Energy transfer study using EISA. **(a)** Chemical structures of the donor molecule, the cationic OPV bolaamphiphile (left) and the acceptor molecule, the modified silica precursor with a rhodamine B derivative covalently attached (right). **(b)** Photographs of OPV/PHEMA amorphous film (left) and OPV/silica ordered film (right) cast from precursor solutions containing 2mol% rhodamine B under UV irradiation (λ = 365 nm). (Reproduced from Stupp, S.I. et al., J. Amer. Chem. Soc. **2006,** 128, 5493 with permission, copyright American Chemical Society).

peaks could be assigned possibly to a lamellar structure. However, a hexagonal structure could be present in these systems resulting from the packing of cylindrical micelles aligned parallel to the substrate, and giving rise only to (01) and (02) reflections so that the (11) reflection would not be observed.

To probe the ordering in these films along the in-plane and surface normal directions and determine their nanoscale structure, GIXS measurements were performed at the APS with a 2D area CCD detector (see Figure 3.9 (a)). The GIXS pattern for the OPV/silica hybrid film is shown in Figure 3.9 (b) with momentum transfer reciprocal space coordinates q_x-q_z, where q_z is the out-of-plane direction and q_x is in-plane and perpendicular to the incident beam. Due to the Kapton foil placed over the sample with flowing N_2 to prevent ozone formation and minimize radiation damage, a Kapton powder diffraction ring intersecting d_{04} is evident. An oversaturation along the q_z axis is observed due to the strong intensity along the specular direction. The pattern shows a slightly distorted 2D hexagonal phase with the out-of-plane vector slightly shorter than the in-plane. To take into account this distortion, a rectangular face-centered unit cell with lattice parameters a_{rec} and c_{rec}, was used to index the diffraction spots and represent the vertically strained hexagonal lattice (see Figure 3.9 (c)). The 2D hexagonal (*hex*) unit cell axes are shown as red-dashed line vectors. The 2D rectangular face-centered *(rec*) unit cell axes are indicated by black arrows with c_{rec} along the surface normal.

The GIXS pattern in Figure 3.9 (b), with the red arrows representing the reciprocal space 2D hexagonal unit cell axes, is generated by a film mineralized with a starting molar ratio of TEOS to OPV of 6.67, the same amount used in for the energy transfer experiments with

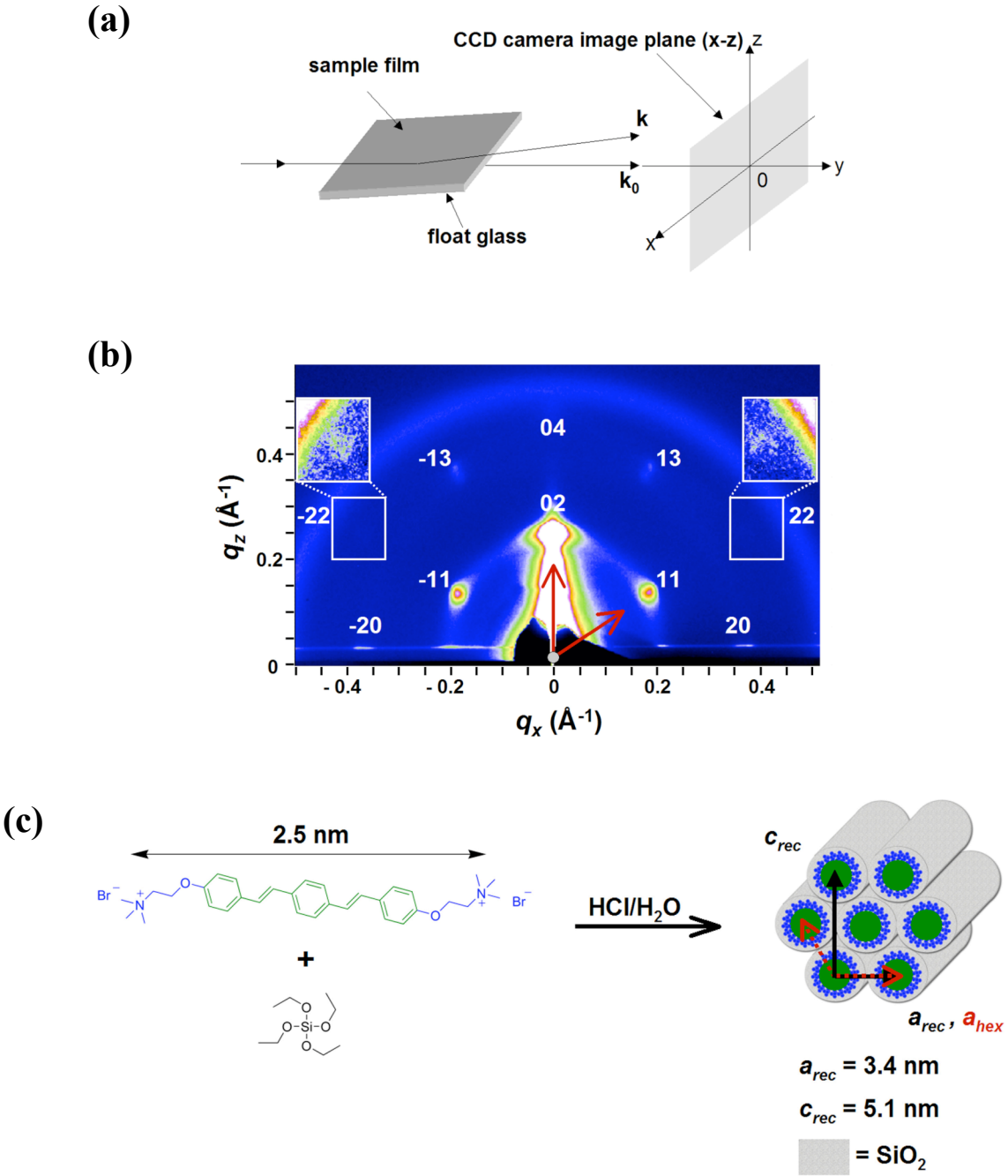

Figure 3.9. **(a)** Schematic of experimental set-up and geometry of 2D grazing-incidence X-ray scattering (GIXS). **(b)** Indexed GIXS pattern in reciprocal-space of mineralized cationic OPV/silica film. The reciprocal space 2D hexagonal (*hex*) unit cell axes are indicated by red arrows. **(c)** Schematic of EISA and formation in real-space of vertically strained hexagonally packed cylindrical micelles with their axes lying parallel to the surface planar. The 2D hexagonal (*hex*) unit cell axes are shown as red-dashed line vectors. The 2D rectangular face-centered (*rec*) unit cell axes are indicated by black arrows with c_{rec} along the surface normal.

rhodamine.[123] When the observed diffraction spots are indexed, a_{rec} is found to be equal to 3.4 nm and c_{rec} = 5.1 nm (see Figure 3.9 (c)).[111]

$$\frac{1}{d_{hl}^{\ 2}} = \frac{h^2}{a_{rec}^{\ 2}} + \frac{l^2}{c_{rec}^{\ 2}} \Rightarrow \frac{1}{d_{20}^{\ 2}} = \frac{4}{a_{rec}^{\ 2}} \Rightarrow a_{rec} = 2 * d_{20} = 3.4nm \qquad (3.2)$$

$$\frac{1}{d_{hl}^{\ 2}} = \frac{h^2}{a_{rec}^{\ 2}} + \frac{l^2}{c_{rec}^{\ 2}} \Rightarrow \frac{1}{d_{02}^{\ 2}} = \frac{4}{c_{rec}^{\ 2}} \Rightarrow c_{rec} = 2 * d_{02} = 5.1nm \qquad (3.3)$$

This characterizes the nanoscale structure as distorted cylinders with diameters of 3.4 nm parallel to the substrate and 3.1 nm out-of-plane. Details of the conversion of the CCD images of the GIXS patterns from reciprocal space into real space, including the position spacings of all indexed diffraction spots, are provided in Appendix II.1. For an undistorted 2D hexagonal lattice, the ratio of the rectangular face-centered lattice spacings would be $c_{rec}/a_{rec} = \sqrt{3}$.[111] The one-dimensional shrinkage of the cylinders normal to the substrate creates elliptical rather than perfectly circular shapes for the cylindrical cores. This effect has been previously attributed to vertical compressive strain caused by drying effects and siloxane condensation occurring after the hexagonal mesophase forms.[113, 114, 129, 131, 136] The hexagonally packed cylindrical micelles are formed in the hybrid films oriented parallel to the substrate surface. As observed in all previous work on hexagonal mesoporous silica, we expect the conjugated surfactants to orient transverse to the long axis of the pores (see Figure 3.9 (c)). In addition, the fully extended length of the OPV amphiphile, as mentioned previously, is approximately 2.5 nm between the two nitrogen atoms, and therefore the observed overall cylinder diameters, 3.4 nm in-plane and 3.1 nm out-of-plane, are consistent with transverse orientation of the molecules with silica shells formed around them. The charged end groups of the amphiphiles are expected to interact with

TEOS, the silica precursor, and thus the inorganic material should coat the exterior of the cylindrical aggregates of conjugated molecules.

The observed diffraction spots do not change their positions when samples are rotated about their surface normal direction. This indicates the presence of individual domains consisting of aligned hexagonally-packed cylinders. The cylindrical axis of each domain is aligned parallel to the surface, but there is no preferred in-plane orientation for these domains. While most of the domains lie flat on the substrate, the faint powder rings produced around the diffraction spots indicate that a small fraction of the domains are randomly oriented.

In order to study the effect of the molar ratio of silica on the final overall structure, two more hybrid film samples were prepared by maintaining a constant concentration of **4** (6 mg/mL) and either increasing or decreasing the molar concentration of TEOS, and proportionally the acid catalyst, HCl, in order to minimize siloxane condensation and insure cooperative assembly of the surfactant and silica.[86] In these cases, the same pseudo-hexagonal packing or rectangular face-centered unit cell is generated. In fact, the resulting d-spacings and cylinder dimensions remain constant for the unit cell in all three cases with starting molar ratios of TEOS to cationic OPV of (a) 10, (b) 6.67 and (c) 3.33 equivalents as shown in Figure 3.10. Because the cylinder dimensions do not change with the amount of TEOS, the results suggest that there is a maximum molar ratio of TEOS which will interact with the fixed number of charged end groups of OPV amphiphilic molecules to generate the hexagonally packed nanoscale structure. When more TEOS is added, this fixed number of charged end groups on amphiphiles prevents further silica from being incorporated around the cylindrical aggregates. The XRR studies suggest that the additional silica formed is not incorporated within the cylindrical hybrid nanostructure (vide

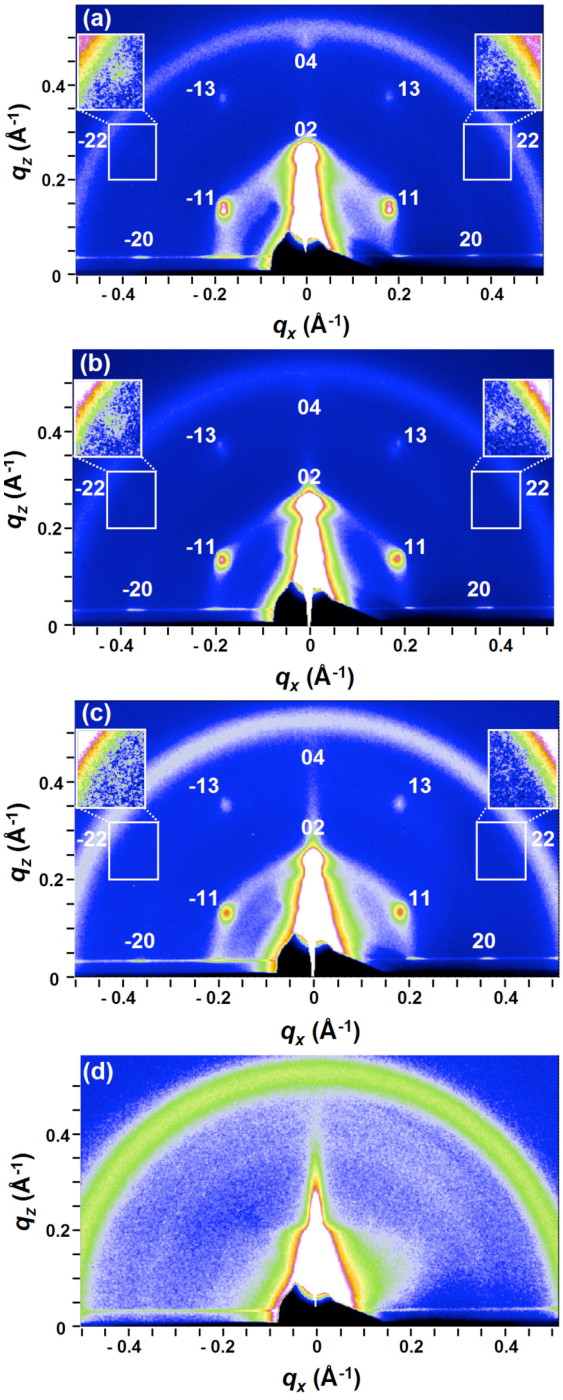

h	l	d(Å)
1	1	28.00
0	2	25.42
2	0	17.20
1	3	14.93
2	2	14.08

h	l	d(Å)
1	1	27.72
0	2	25.57
2	0	16.68
1	3	14.89
2	2	14.20

h	l	d(Å)
1	1	27.92
0	2	26.19
2	0	17.00
1	3	15.66
2	2	14.31

Figure 3.10. 2D GIXS patterns identifying vertically strained hexagonal packing of cationic OPV bolaamphiphile/silica films and lack of ordering in unmineralized OPV film. Listed *hl* indices for each Bragg peak are in reference to the 2D rectangular face-centered unit cell. The starting molar ratio of OPV/TEOS of: **(a)** 1:10, **(b)** 1:6.67, **(c)** 1:3.33, **(d)** 1:0. Insets showed magnified portions of weaker intensity peaks. Tables to right show positions for indexed spots.

infra). As previously reported, a uniform distribution of the amphiphiles is implied by the linear relationship between the optical density and film thickness of the hybrids.[123]

In the absence of TEOS and the acid catalyst, a film cast from the cationic OPV **4** in solution at the same concentration near its solubility limit of 9.0 mM did not lead to the hexagonal structure (see Figure 3.10 (d)) as should be expected from the lack of any Bragg peaks in the XRR spectra in Figure 3.6. This result implies that the ordering observed in the hybrid films is a direct result of the mineralization process. While some rather weak ordering might exist, as shown in Figure 3.6 (b), due to the bolaform of the amphiphile, the absence of silica prevents the charge-shielding necessary to allow for any long-range packing of molecules with like charges at both termini.

The highly charged nature of the conjugated amphiphiles is very important to the development of long range order in the self-assembling hybrid materials investigated. In the absence of mineralization, charges on these molecules clearly disrupt packing, but binding of TEOS by the end groups and the subsequent mineralization screens charges in the cationic amphiphiles. This screening, in turn, allows the possibility of forming the long range order observed in the hexagonal phase of the hybrid. Based on curvature packing arguments,[25] as well as the similar behavior of CTAB that has been previously reported,[113] the aggregates of conjugated molecules, it is concluded, are sterically forced into the curved hexagonal structure as the film is formed and solvent is evaporated. This results in the transformation from a lamellar to a hexagonal nanostructure. The uncharged derivative of the OPV bolaamphiphile packs in a layered structure which subsequently collapses upon protonation of the amphiphiles into their positively-charged form. As shown in Figure 3.11, in solution, the cationic OPV

bolaamphiphiles are fully solvated. The silica precursors, which are omitted from Figure 3.11 for simplicity, interact with the hydrophilic end groups, screening the charges and allowing the molecules to aggregate into a lamellar (layered) phase. The solution begins to concentrate with solvent evaporation upon film casting. As the silica hydrolysis continues the added bulk on the head groups breaks the lamellar phase into a more rounded cylindrical micelle and the cylindrical micelles than pack into hexagonal arrays.

The symmetric dual charge nature of the OPV amphiphiles and the subsequent interactions with silica precursors gives rise to long range ordering in these nanostructured hybrid films. The presence of two binding sites for TEOS per molecule and their ability to π-stack may also be a contributing force to the transformation and the long range order observed in these hybrid structures. In comparison to a surfactant molecule such as CTAB, not only are hydrophobic interactions important in this case, but π–π stacking interactions among the conjugated amphiphiles should also promote aggregation of the OPV segments. It is assumed that twisting of the amphiphiles within the π–stacked aggregates along the long axis gives rise to the uniaxial symmetry observed.

To test the generality of this self-assembling hybrid system with a different amphiphile, the conjugated segment was substituted for the more conductive quaterthiophene analogue. Interestingly, upon mineralization with silica the same distorted hexagonally packed cylindrical micelle nanostructured films. Figure 3.12 shows the CCD image obtained for one quadrant of the q_x-q_z plane for a film prepared from a 1-mL solution in MeOH of 6 mg of cationic quaterthiophene amphiphile **8** and 14 μL TEOS with a molar ratio of TEOS to amphiphile of 7.23. In the case of the cationic quaterthiophene amphiphile, the slightly longer extended

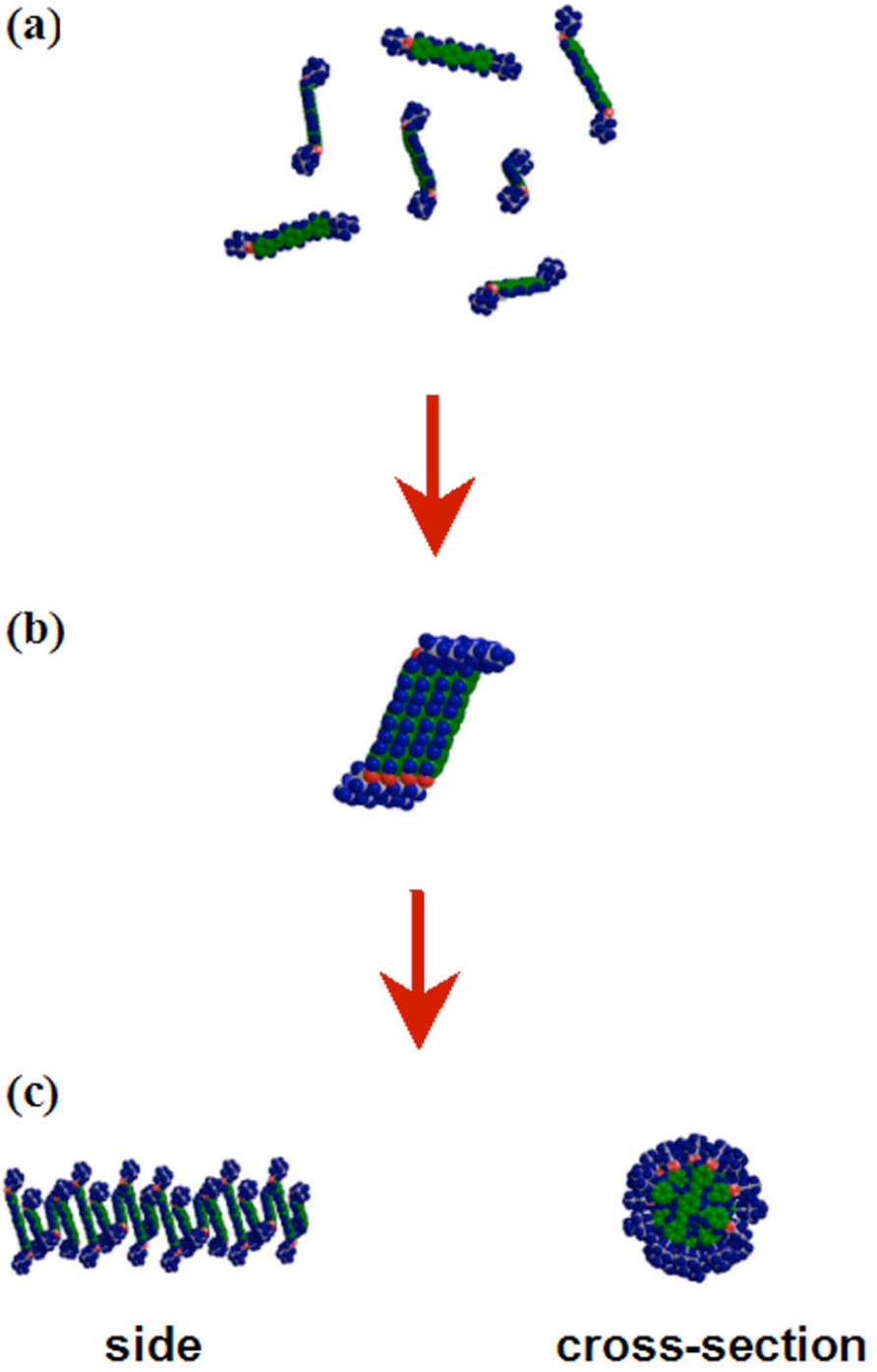

Figure 3.11. Proposed mineralization mechanism occurring during EISA. **(a)** Fully solvated molecules in solution. **(b)** Molecules aggregating into layers due to screening of charges by silica precursors, and upon film casting and solvent evaporation. **(c)** Side- (left) and cross-sectional (right) views of layers sterically breaking and forming rounded cylindrical micelles that pack hexagonally upon silica condensation. Silica and charges have been omitted for simplicity.

(a)

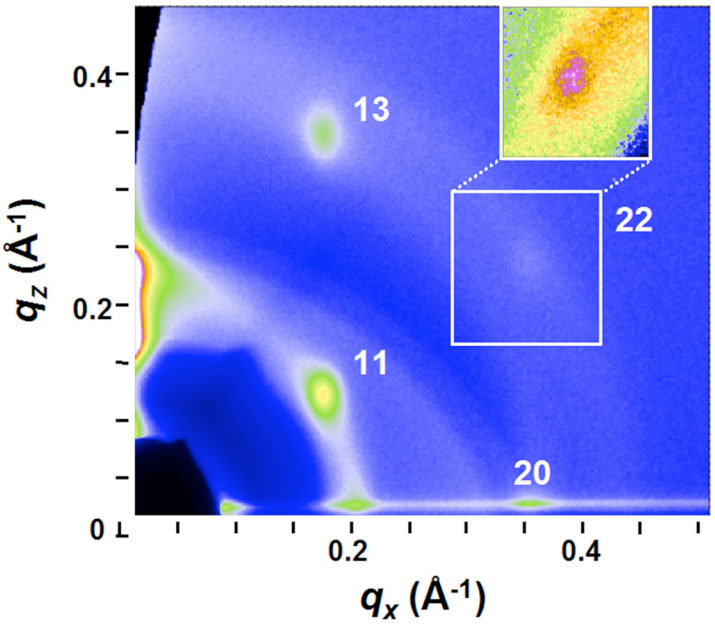

h	l	d(Å)
1	1	29.26
0	2	26.55
2	0	17.57
1	3	16.10
2	2	14.80

(b)

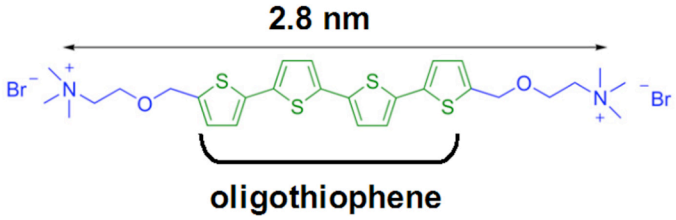

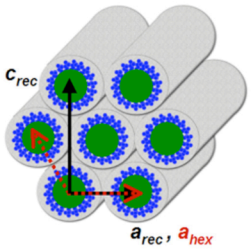

a_{rec} = 3.6 nm

c_{rec} = 5.8 nm

Figure 3.12. **(a)** 2D GIXS pattern of cationic quaterthiophene bolaamphiphile/silica film for one quadrant of q_x-q_z. Listed *hl* indices for each Bragg peak are in reference to the 2D rectangular face-centered unit cell. Inset shows magnified portion of weaker intensity peak. Table to right show positions for indexed spots. **(b)** Chemical structure of cationic quaterthiophene bolaamphiphile (left) and real-space schematic of vertically strained hexagonal packing of cationic quaterthiophene/silica film with resulting dimensions (right).

molecular length of 2.8 nm compared to cationic OPV trimer amphiphile (2.5 nm) is also reflected in a slight increase of the unit cell dimensions with a_{rec} = 3.6 nm and c_{rec} = 5.8 nm. This leads to cylinder dimensions of 3.6 nm parallel to the substrate and 3.4 nm out-of-plane. This result using GIXS on a second compound further supports the expectation that the conjugated molecules are oriented perpendicular to the long axis of a one-dimensional cylindrical aggregate and surrounded by silica.

3.5.2 Specular X-ray reflectivity

In order to obtain more information about the internal structure of the OPV hybrid films, specular XRR was used to probe the periodicity along the surface normal q_z (see Figure 3.13 (a)). For the sample with the lowest starting molar ratio of TEOS to **4** of 3.33, the specular reflectivity in Figure 3.13 (b) yielded the first- and second-order allowed Bragg peaks corresponding to 2.6 nm and 1.3 nm, respectively. The Bragg peaks, whose periodicity is double that of the Kiessig thickness fringes, are calculated by:

$$d = 2\pi / q_z \qquad (3.4)$$

where q_z is the peak position. The peaks were also observed in the CCD image in Figure 3.10 (c) and are assigned to the (02) and (04) diffractions of the rectangular face-centered unit cell. The overall film thickness is determined to be $2\pi/\Delta q_z$ = 48 nm.

The distances between the observed peaks in the Patterson map (see Figure 3.14 (a)) had an average value of 2.7 nm which closely matches the position of the first-allowed Bragg peak. These peaks are evident along the entire film profile, indicating that the periodicity of the hexagonally packed cylinders exists throughout the q_z direction. The peak at 48 nm corresponds

(a)

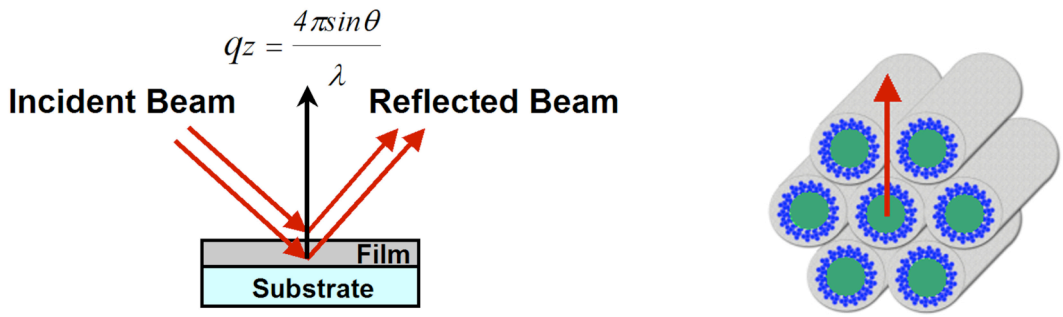

(b)

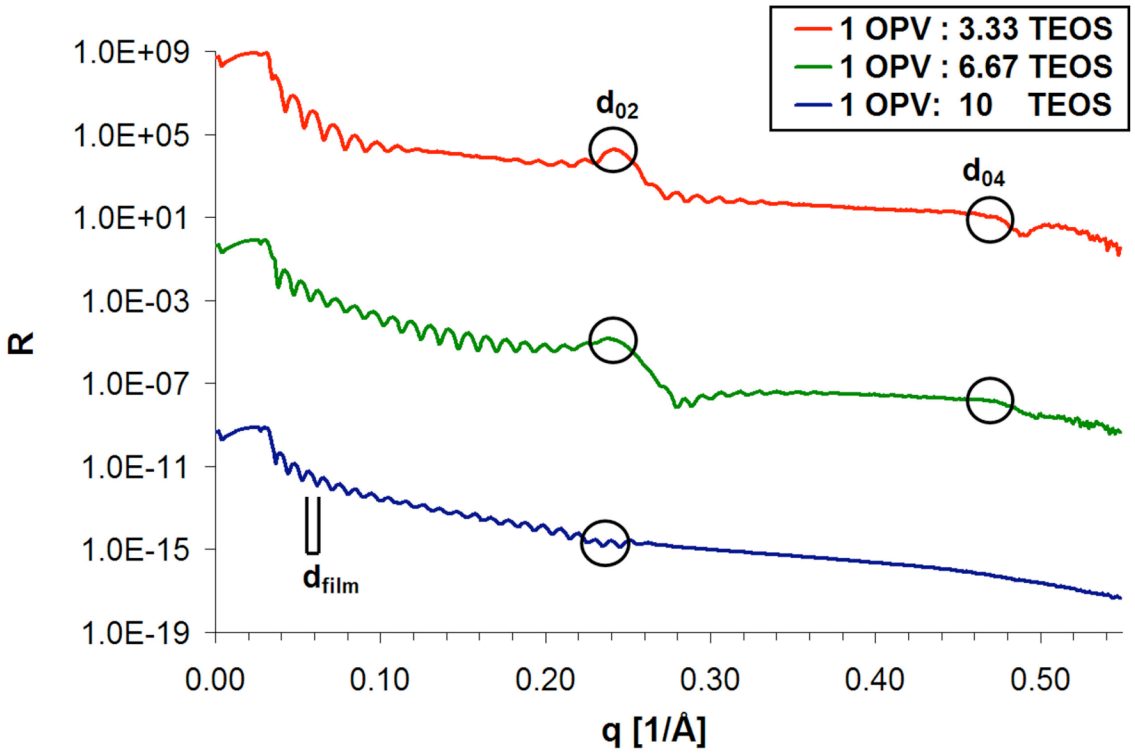

Figure 3.13. **(a)** Schematic XRR set-up and geometry probing layers of 2D hexagonally packed cylindrical micelles along surface-normal. **(b)** Specular XRR data for mineralized OPV films with starting molar ratios of OPV **4**/TEOS of 1:3:33 (red), 1:6.67 (green) and 1:10 (blue).

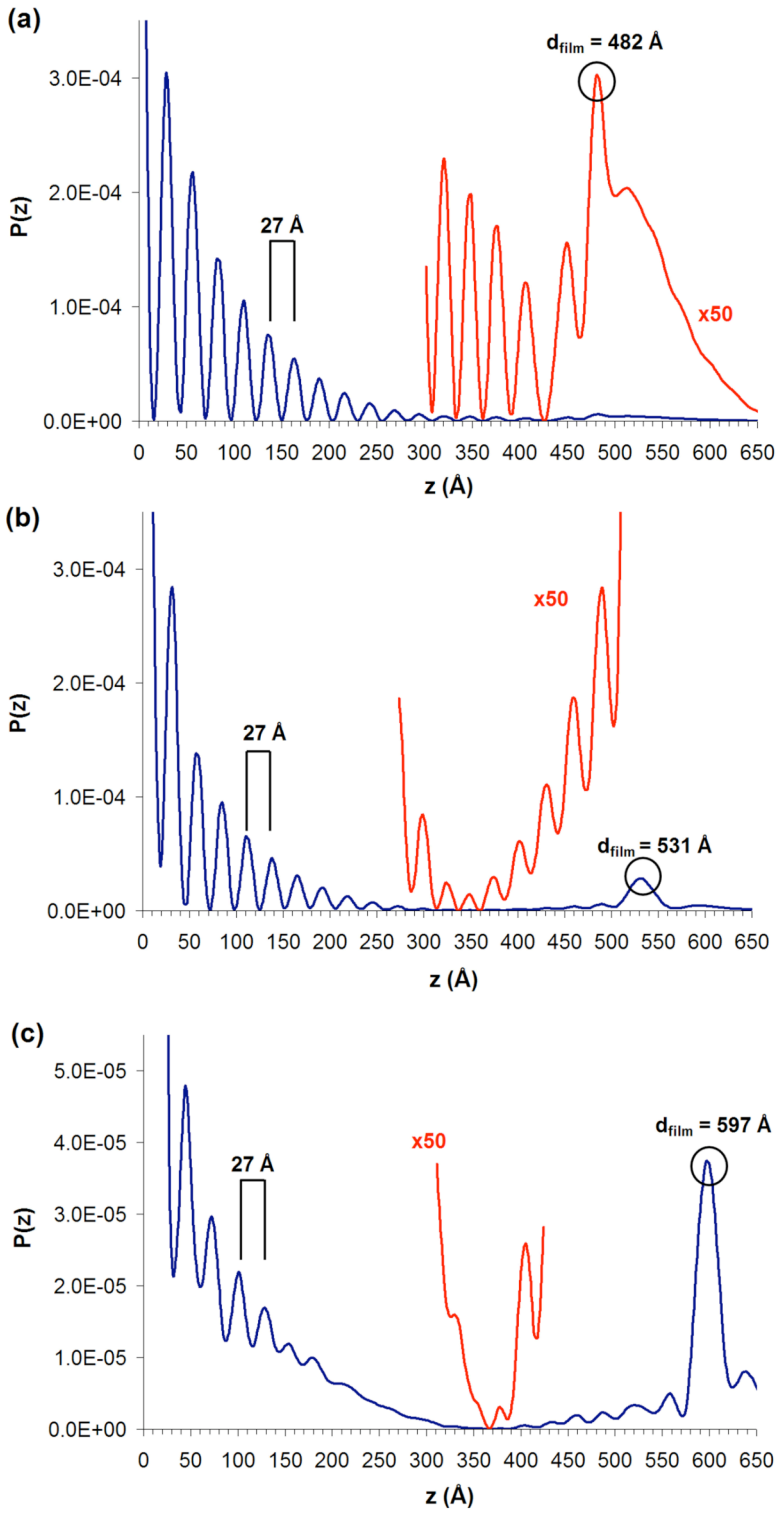

Figure 3.14. Patterson maps of mineralized OPV films with starting molar ratios of OPV **4**/TEOS of **(a)** 1:3.33, **(b)** 1:6.67, **(c)** 1:10 with red insets showing magnified views.

to the overall film thickness. Profilometry on all films matched the thicknesses obtained from XRR measurements.

When the initial molar ratio of TEOS to **4** is 6.67, the specular reflectivity again generates the first- and second-order allowed Bragg peaks corresponding to the (02) and (04) peaks of the rectangular face-centered unit cell (see Figure 3.13 (b)). The well-pronounced oscillations throughout the angular range indicate a homogeneous and uniform film. [134, 135] While the nanoscale structure is maintained, it is clear that an increased amount of silica leads to an increase in the overall film thickness (53 nm) that is also evident in the Patterson function in Figure 3.14 (b). The Patterson map further indicates that the periodicity of the nanostructure exists along the entire film thickness profile.

The hybrid sample measured with the largest starting molar ratio of TEOS, 1:10 **4**/TEOS also formed hexagonally packed cylindrical micelles in Figure 3.10 (a). However, the first-order allowed Bragg peak is no longer obvious and the second-order peak completely disappears in the specular reflectivity in Figure 3.13. The interference fringes, which correspond to the film thickness (60 nm), disappear past the first-order allowed Bragg peak. This damping of the thickness fringes and their appearance within a narrower angular range implies that the roughness of the film is higher than for other samples. Roughness in a film gives rise to diffuse scattering, resulting in less intensity for the specularly reflected beam. [134, 135] Further inspection of the Patterson map in Figure 3.14 (c) shows a dampening of the periodicity peaks within the middle of the film thickness profile, indicating that while the film is highly ordered at both its bottom and top interfaces, disorder seems to exist in the middle of the film. This implies that with an increase in the starting amount of TEOS in relation to OPV conjugated amphiphiles the

distorted hexagonal structure is still formed, but the additional silica formed is not incorporated within the periodic framework and instead exists as bulk silica in regions within the center of the film.

3.6 Summary and Outlook

This chapter describes the nanoscale structure of model hybrid materials, synthesized by evaporation-induced self-assembly, with phases of silica and electronically active bolaamphiphile assemblies containing either OPV or oligothiophene segments. Grazing-incidence X-ray scattering studies of these materials revealed the formation of two-dimensional hexagonally packed cylindrical micelles of the organic molecules with diameters between 3.1 and 3.6 nm and cylindrical axes parallel to the surface. During the self-assembly process at low pH, the cylindrical aggregates of conjugated molecules become surrounded by silica giving rise to a hybrid structure with long range order. Specular X-ray reflectivity confirmed the long range periodicity of the hybrid films within a specific range of molar ratios of tetraethyl orthosilicate to cationic amphiphile. Long range ordering, however, was not observed in fully organic analogues unless quarternary ammonium groups were replaced by tertiary amines. These observations suggest that charge screening in these bis-cationic conjugated molecules by the mineral phase is a key factor in the evolution of long range order in the self-assembling hybrids. As we turn to the proper choice of a conductive inorganic phase in the following chapter, the long range order and electronic function in the organic compartments of the hybrids described here provide great insight into the goal of achieving self-assembling hybrid photovoltaic systems.

3.7 Experimental

Cationic amphiphiles were synthesized by Dr. Keisuke Tajima and David Stone of the author's laboratory. GIXS measurements of EISA-formed films were carried out in collaboration with the Bedzyk group, who also provided assistance in the indexing and analysis of synchrotron X-ray data.

3.7.1 Synthesis and thermal characterization

The synthetic approach, purification and characterization of the OPV bolaamphiphile are described in the reference.[123] Further details for the quaterthiophene bolaamphiphile are described in Appendix I.2. Thermogravimetric analysis (TGA) using a TA Instruments 2920 TGA showed an onset of decomposition by 200 °C on heating at 10 °C/min in air.

3.7.2 Powder X-ray diffraction

XRD patterns were recorded using a Rigaku ATX-G X-ray diffractometer at an operating power of 50 kV and 240 mA with a CuKα (8.05 keV, 1.54 Å) source.

3.7.3 Film preparation

Precursor solutions of the cationic bolaamphiphile/silica hybrid films were prepared by first dissolving 6.0 mg of the amphiphile in 1.0 mL of MeOH. Solutions were ultra-sonicated to fully dissolve the amphiphile and then 15 μL of 35 wt% aqueous HCl and 14 μL of TEOS were added for a molar ratio of 1:6.67 (**4**/TEOS) or 1:7.23 (**8**/TEOS). For concentration-dependent studies, the ratio of amphiphile to TEOS was varied by adjusting the amount of TEOS and acid added to the amphiphile solution. Solutions of the pure OPV amphiphile films were prepared by dissolving 6.0 mg of the amphiphile in 1.0 mL of MeOH and further sonicating for full dissolution. All solutions were membrane filtered (pore size: 0.45 μm) and deposited on 2.5 cm

x 2.5 cm float glass substrates by spin-casting at 1000 rpm for 30 s. Substrates were treated prior to deposition in piranha solution (7:3 (v/v) H_2SO_4/H_2O_2 (30% aq)) for 10 min at 100 °C to remove organic contaminants from the surface followed by rinsing with water (Millipore Milli-Q-purified, 18.3 MΩ cm), soaking in (4:1 (v/v) NH_4OH/H_2O_2 (30% aq)) for 5 min, rinsing with water (Millipore Milli-Q-purified, 18.3 MΩ cm) and finally drying under a stream of dry N_2. The films were left overnight at ambient atmosphere and subsequently dried under high vacuum for 3 hr. for full solvent evaporation.

3.7.4 Grazing-incidence X-ray scattering

Grazing incidence X-ray scattering measurements were carried out at the 5ID-C beam line of the APS at an energy of 12.4 keV (1.00 Å wavelength). The incident angle was set at or near the critical angle for the glass substrate (q_c = 0.032 $Å^{-1}$) to enhance scattering from the film with a MAR CCD 2D area detector located 340 mm away from the sample for the OPV studies. The detector was located 388 mm away from the sample for measurements on the thiophene derivative. The sample was kept under flowing nitrogen so as to prevent ozone formation and minimize radiation damage. Frames were collected for 30-100 s. Further details of the conversion of the CCD images from reciprocal space to direct space and indexing are provided in Appendix II.1

3.7.5 Specular X-ray reflectivity

Measurements of the pure OPV amphiphile films and initial measurements of the hybrid films were measured using a Rigaku ATX-G instrument at an operating power of 50 kV and 240 mA with a CuKα (8.04 keV, 1.54 Å) source and incident beam size of 0.1 mm wide by 0.3 mm high. Further XRR of the hybrid films was performed at the 5ID-C beam line of the APS at 12.4

keV energy (1.00 Å wavelength).

Samples were positioned in the center of the beam (half the full intensity), and aligned so that the rotation axis always lay on the sample surface. The X-ray beam intensity reflected by the sample at grazing angles was monitored. Collected reflectivity scans were background subtracted and normalized to the ideal Fresnel reflectivity (R_F) for float glass. Samples were tested to confirm that radiation damage was not affecting the collected data over the course of the multiple scans made. Film thicknesses were confirmed using a Tencor P10 profilometer and averaging 15 measurements per sample.

Patterson maps were obtained by taking the inverse fourier transform (IFT) of the normalized reflectivity data. The Matlab code used for the IFT is given in Appendix II.2.

CHAPTER FOUR

Electrochemical Self-Assembly of Zinc Oxide and Conjugated Cationic Amphiphiles

Chapter 4: Electrochemical Self-Assembly of Zinc Oxide and Conjugated Cationic Amphiphiles

4.1 Introduction

Electrodeposition offers a one-step, room temperature approach towards synthesizing highly stoichiometric binary n-type semiconductors with few atomic defects in high yield.[55] In continuing to pursue a strategy towards achieving self-assembled hybrid materials with nanoscale ordering for photovoltaics, this chapter targets the synthesis of the inorganic n-type phase, specifically ZnO, by electrochemical means.

Dye-sensitized solar cells have been designed by the electrodeposition of phthalocyanine-modified ZnO.[137-139] In addition, surfactant-assistant electrochemical templating, has been reported in the literature in achieving lamellar morphologies of ZnO with an organic structure-directing surfactant.[89, 90] In this approach, a precursor solution is composed of soluble inorganic reactants and organic surfactant molecules. The end functional group of these molecules will bind to specific crystal faces of the growing semiconductor, thus controlling the morphology of the grown inorganic phase. In addition to allowing for the synthesis of a conductive n-type inorganic in a co-assembly approach with an organic amphiphile, the electrodeposition technique is also attractive because it is possible to guarantee an electrical connection between the growing inorganic component and the electrode. This is because the resulting hybrid grows directly on the surface of the substrate electrode.

In this chapter, the electrodeposition of ZnO into lamellar nanostructures by structure-directing organic surfactants is pursued for hybrid photovoltaics by using surfactant molecules that contain conjugated p-type blocks. In so doing, a nanoscale morphology of alternating n-type

and p-type layers is targeted in a one-step, cost-effective approach. Due to the π-π stacking of the organic moieties, the organic substituent are expected to have the ability to conduct holes in a direction parallel to the sheet axis. The resulting nanoscale structure and morphology are investigated using XRD, TEM, XAS. Furthermore, preliminary measurements are made on the optical and electronic behavior of these hybrid nanostructures.

4.2 Surfactant-Assisted Electrochemical Synthesis of Zinc Oxide

The electrochemical synthesis of ZnO is achieved through the cathodic deposition of an aqueous $Zn(NO_3)_2$ bath. Figure 4.1 shows the schematic of the three-electrode electrodeposition set-up, where ITO-coated glass is the cathode or working electrode on which nucleation and growth occurs. The ITO electrode serves the dual purpose of being the anode in a solar cell device, and therefore, electrodeposition provides for direct electrical contact with the active layer in the formation of devices described in Section 4.6. The two-step reaction at the cathode proceeds by the reduction of the $Zn(NO_3)_2$ according to the equations below:

$$NO_3^- + H_2O + 2e^- \rightarrow NO_2^- + 2OH^- \qquad E_{red} = 0.01V \qquad (4.1)$$

$$2(OH^-) + Zn^{2+} \rightarrow Zn(OH)_2 \rightarrow H_2O + ZnO \qquad (4.2)$$

An Ag/AgCl electrode stored in 3M NaOH serves as the reference. The reaction at the zinc wire counter electrode anode occurs through the equation below:

$$Zn \rightarrow Zn^{2+} + 2e^- \qquad E_{red} = -0.764\ V \qquad (4.3)$$

The cathodic deposition of ZnO proceeds therefore by the final overall equation:

$$Zn + NO_3 \rightarrow NO_2^- + ZnO \qquad (4.4)$$

The above reaction was conducted in a 0.02 M $Zn(NO)_3 \cdot 6H_2O$ solution with a 1:1 (v/v) ratio of H_2O/DMSO. While the presence of water is required for the reduction of the $Zn(NO_3)_2$,

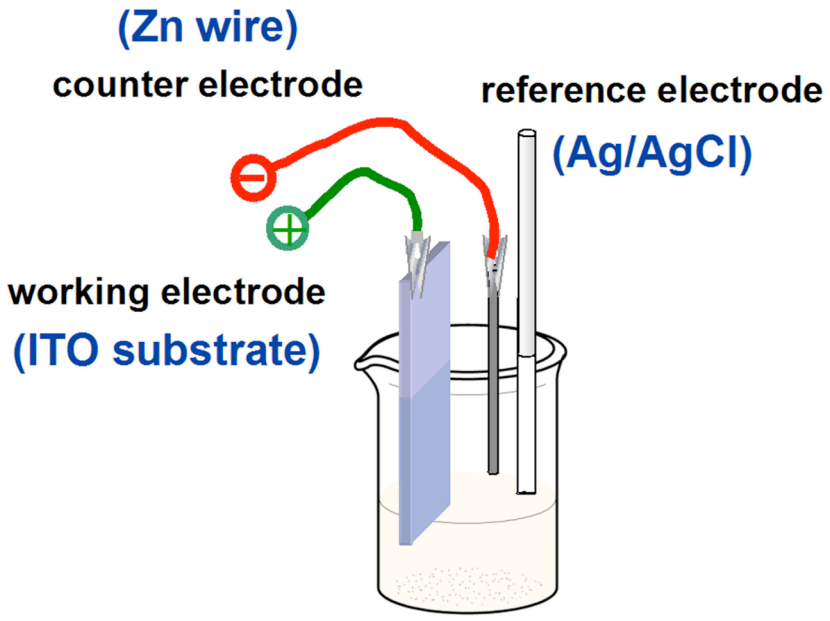

Figure 4.1. Schematic illustration of electrodeposition set-up with labeled electrodes consisting of the counter electrode (zinc wire), the working electrode (ITO substrate), and the reference electrode (Ag/AgCl).

DMSO was added to aid in the solubility of the organic surfactants. As an initial investigation, an applied potential range for deposition of ZnO was determined based on the cyclic voltammetry trace (see Figure 4.2) of a 0.02 M $Zn(NO)_3$•$6H_2O$ solution with a 1:1 (v/v) ratio of H_2O/DMSO in the absence of surfactant. Hexagonally-faceted wurtzite phase ZnO was obtained, as shown in the SEM image in Figure 4.3, and confirmed by powder XRD, at an applied potential of -0.9 V. Less negative potentials generated relatively poor faceting, while more negative potentials led to the generation of Zn metal.

Using the conditions established for the deposition of ZnO under non-surfactant conditions, the initial surfactant investigated was 1-pyrenebutyric acid (PyBA) (see Figure 4.4 (a)). The PyBA surfactant, containing a conjugated, p-type pyrene chromophore attached to an alkyl chain and a carboxylic acid end-group, is the focus of the next two sections in understanding the growth mechanism and resulting structure and morphology of the hybrids generated by the electrodeposition technique.

4.3 Structural Characterization of Hybrid Nanostructures

4.3.1 SEM of platelet structures

The addition of PyBA to the 0.02 M $Zn(NO)_3$•$6H_2O$ electrolyte solution at a concentration of 0.05 wt% (below its critical micelle concentration) led to the deposition of a film of highly-dense platelet structures (see Figures 4.4 (b), (c), and (e)). At this concentration, the ratio of surfactant to zinc nitrate was 1:10. These high-aspect ratio structures were on average 10-50 nm in thickness and 1-5 μm in length (see Figure 4.4 (d)). As observed in the cross-sectional view (see Figure 4.4 (e)), a number of the platelets grow vertically from the

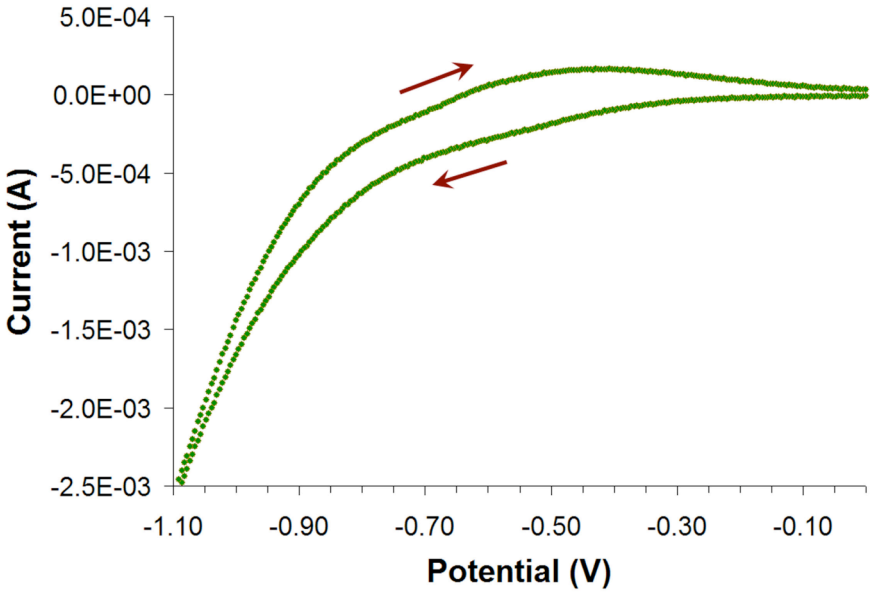

Figure 4.2. Cyclic voltammetry trace from 1:1 (v/v) H_2O/DMSO 0.02 M $Zn(NO_3)_2$ solution.

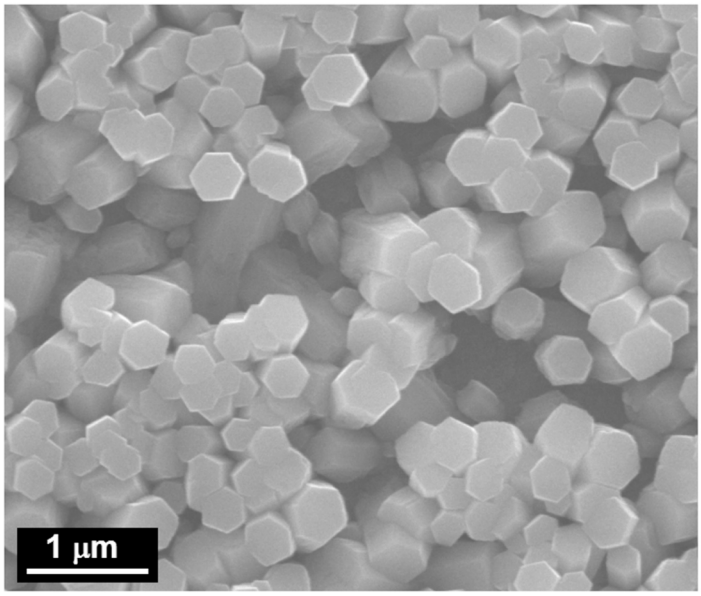

Figure 4.3. SEM of hexagonally-faceted wurtzite ZnO deposited at -0.9 V from 1:1 (v/v) H_2O/DMSO 0.02 M $Zn(NO_3)_2$ solution.

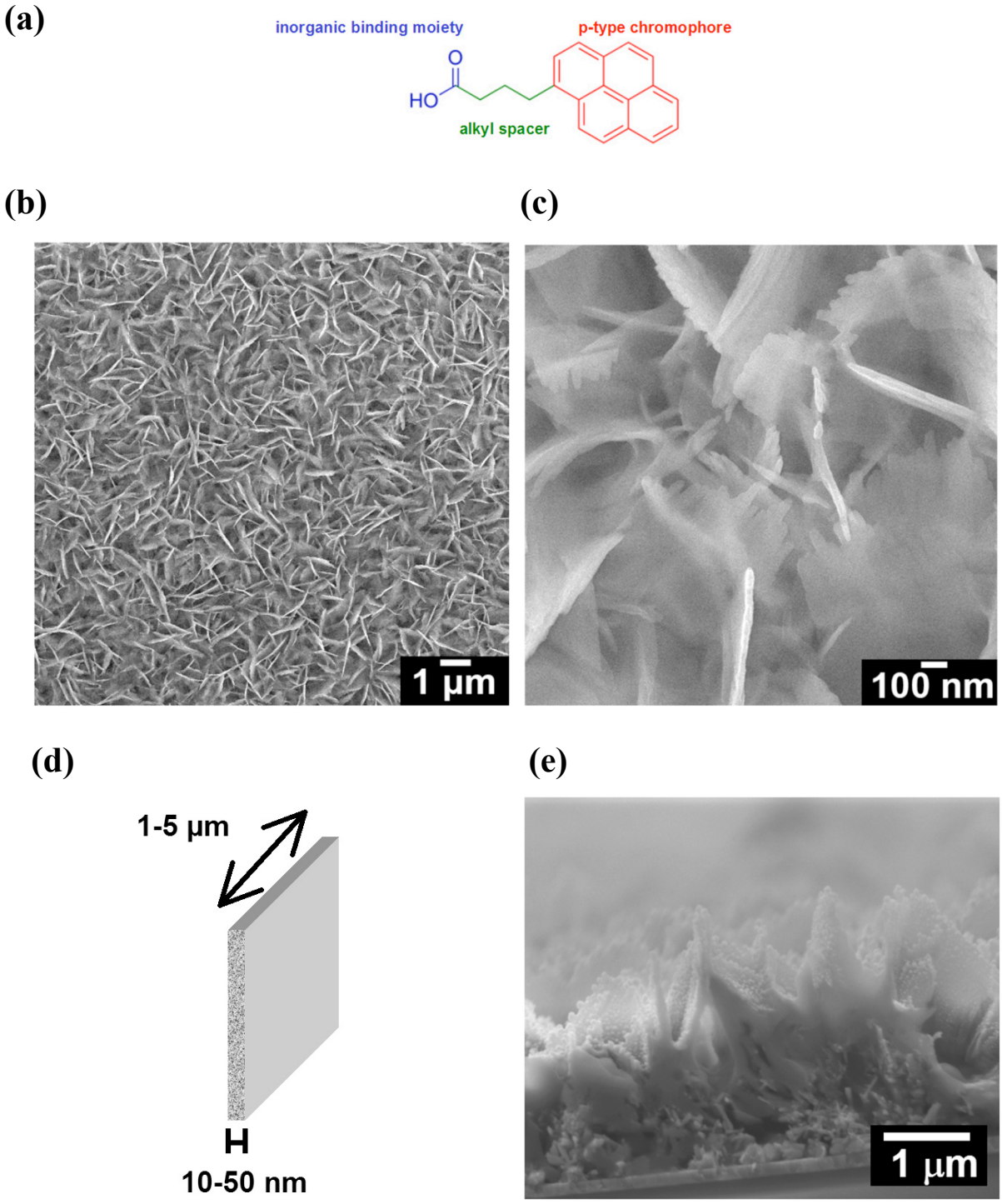

Figure 4.4. (a) Chemical structure of PyBA molecule used in electrochemical ZnO synthesis. **(b)** SEM image (top-down) of platelet nanostructures generated during synthesis. **(c)** magnified SEM image (top-down). **(d)** Illustration of platelets with average dimensions. **(e)** SEM image (cross-section) of platelets grown off the working electrode surface (ITO).

surface. Optical microscopy, as shown in Figure 4.5, revealed the formation of birefringent, crystalline textures.

4.3.2 TEM and SAXS of hybrid lamellae

The ordering within the platelet structures was investigated by small-angle X-ray scattering on the deposited films, which reveals the formation of a lamellar structure with *d*-spacings of 3.2 nm, 1.6 nm, 1.1 nm, and 0.8 nm corresponding to (001), (002), (003), and (004) reflections, respectively (see Figure 4.6). To further probe the origin and identity of this layered ordering, TEM imaging revealed alternating lamellar stripes of dark and bright regions (see Figure 4.7) with a periodicity of 3.2 nm, as identified from the SAXS spectrum. Under TEM, regions of higher electron density appear darker. The dark regions, which are 0.8-1.0 nm in width, therefore, can be assigned to the inorganic, zinc-rich phase. The bright regions, which are roughly 2.4 nm in width, are attributed to the organic surfactant. As depicted in Figure 4.8, based on the extended length of the molecules of 1.1 nm, these dimensions correspond to a bilayer of PyBA molecules with the inorganic phase binding to the end-functionalized carboxylates (COO^-) on either end.

4.4 Morphological Characterization of Inorganic Phase

4.4.1 Temperature dependence of overall nanostructure

The morphology of the growing inorganic phase is believed to be controlled by the organic surfactant by either directing the growth through the organic native supramolecular structure,[68, 69, 73, 74, 140] impeding the growth along certain crystal directions by covalently binding to specific crystal facets,[139, 141] or by stabilizing an intermediate phase of the target hybrid material. As a means to better understand the growth mechanism and identify the

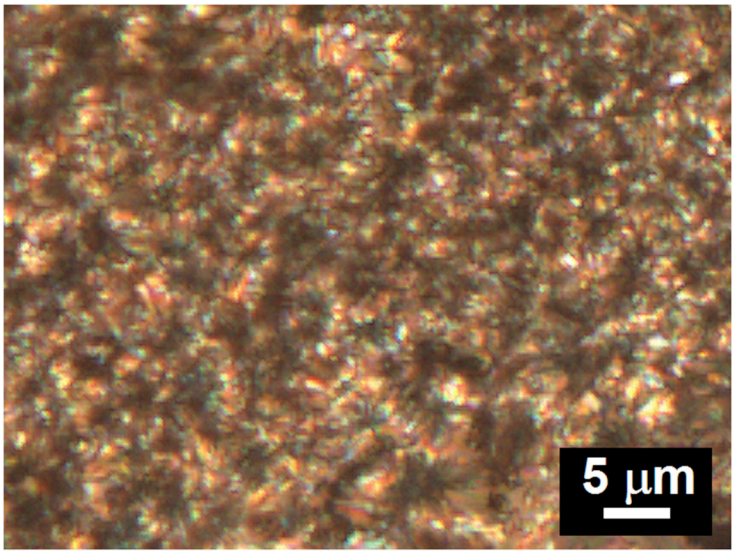

Figure 4.5. Optical micrograph of hybrid film electrochemically deposited at -0.9 V from 0.05 wt.% PyBA in 1:1 (v/v) H_2O/DMSO 0.02 M $Zn(NO_3)_2$ solution.

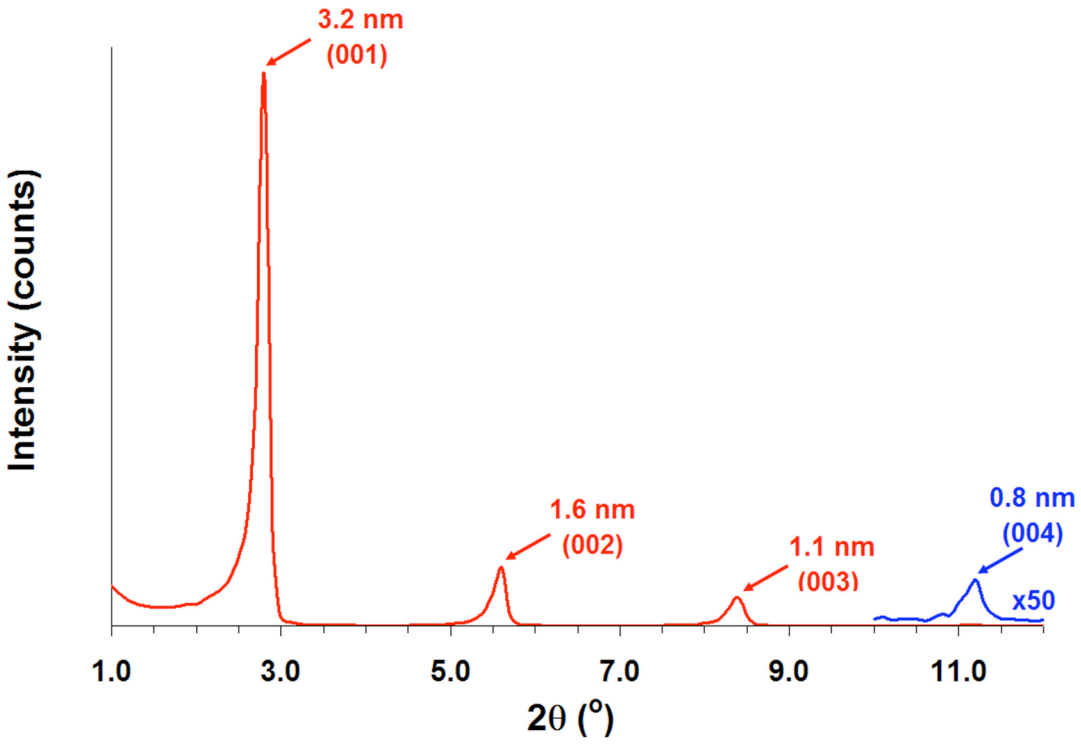

Figure 4.6. Small-angle X-ray scattering spectrum of electrodeposited hybrid film from 0.05 wt.% PyBA in 1:1 (v/v) H_2O/DMSO 0.02 M $Zn(NO_3)_2$ solution indicating lamellar ordering.

(a)

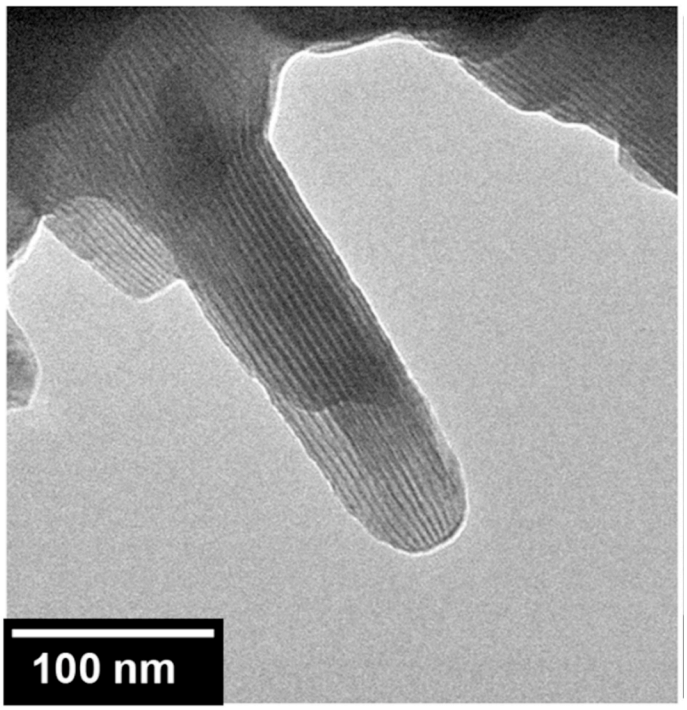

(b)

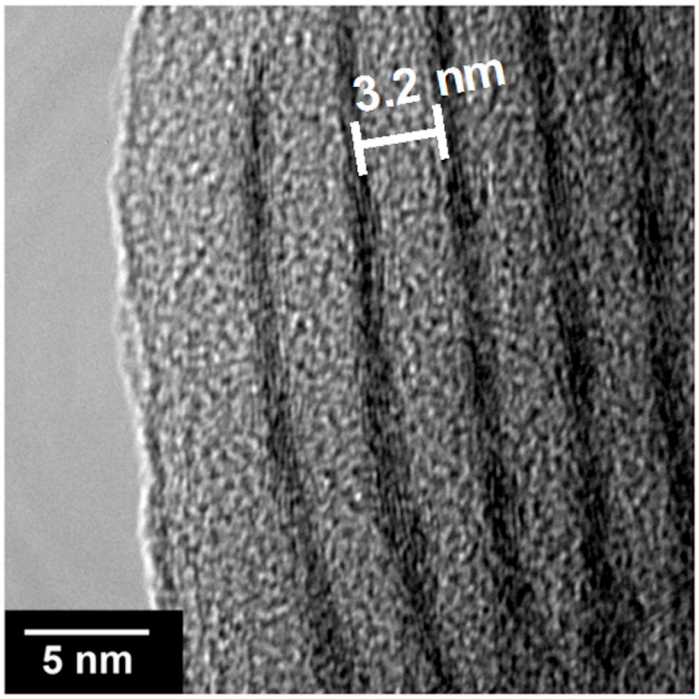

Figure 4.7. TEM images of lamellae generated from electrodeposited hybrid film of 0.05 wt.% PyBA in 1:1 (v/v) H_2O/DMSO 0.02 M $Zn(NO_3)_2$ solution. morphology of the ZnO, temperature-dependent studies were performed on the as-deposited films with the PyBA surfactant.

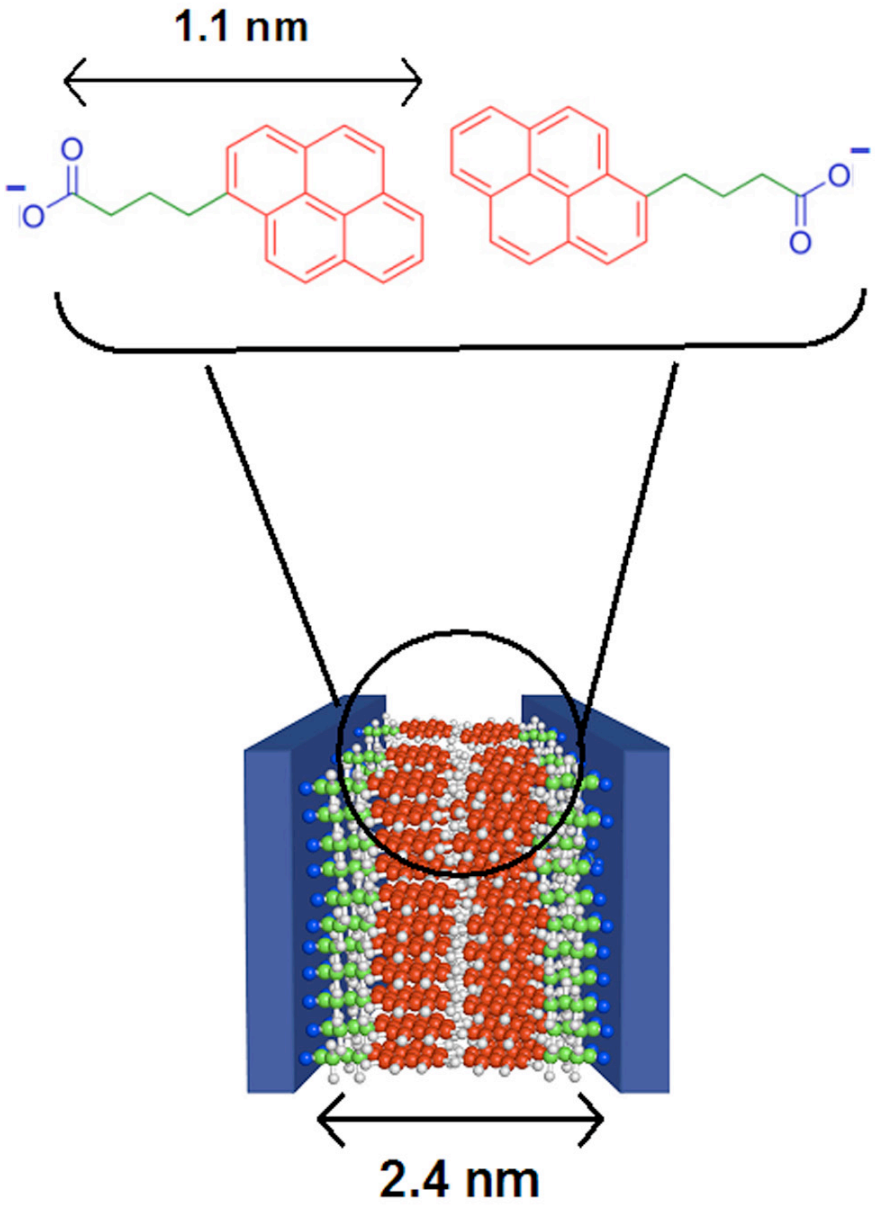

Figure 4.8. Schematic molecular graphic illustration of lamellae generated from electrodeposited hybrid film of 0.05 wt.% PyBA in 1:1 (v/v) H_2O/DMSO 0.02 M $Zn(NO_3)_2$ solution with chemical structure of PyBA.

Thermogravimetric analysis (see Figure 4.9) of the electrodeposited hybrid film revealed a significant loss of water (20 wt% loss) above 100 °C followed by a decomposition onset of the organic surfactant by 300 °C. Coupled with the loss of water, the SAXS spectrum of the film upon annealing to 150 °C for 12 hr. revealed a decrease in the crystallinity of the lamellar ordering with a disappearance of the higher-order d-spacings (see Figure 4.10). In addition, the domain size is decreased with an increase in the width of the d_{001} peak. Interestingly, annealing above 300 °C and the decomposition of the organic, leads to a collapse of the lamellar structure. This observation is in contrast to the work on mesoporous oxides, synthesized by sol-gel means, where the organic is decomposed and the inorganic nanostructured framework retained for further applications.[5, 6] This result, therefore, suggests that the inorganic phase is strongly bound to the carboxylate end groups of the surfactants, which direct the formation of the lamellar phase. The decomposition of the organic and the disruption of this binding, also leads to the disruption of the lamellar ordering. As such, the bound carboxylate anion stretch at 1700 cm^{-1} in FT-IR (see Figure 4.11) is still present for the hybrid film at 150 °C annealing, but weaker in intensity than at room temperature. In addition, the FT-IR spectrum reveals that the 150 °C leads to a disappearance of the –OH stretch that is evident at room temperature, further confirming the water loss observed in TGA.

4.4.2 X-ray absorption spectroscopy

X-ray absorption spectroscopy (XAS) was used to determine the identity of the inorganic phase formed in the electrodeposited hybrid films. In addition, it was necessary to determine the temperature-dependent changes of the local structure of the inorganic phase based on the annealing behavior observed in the previous section for the overall hybrid nanostructure. While

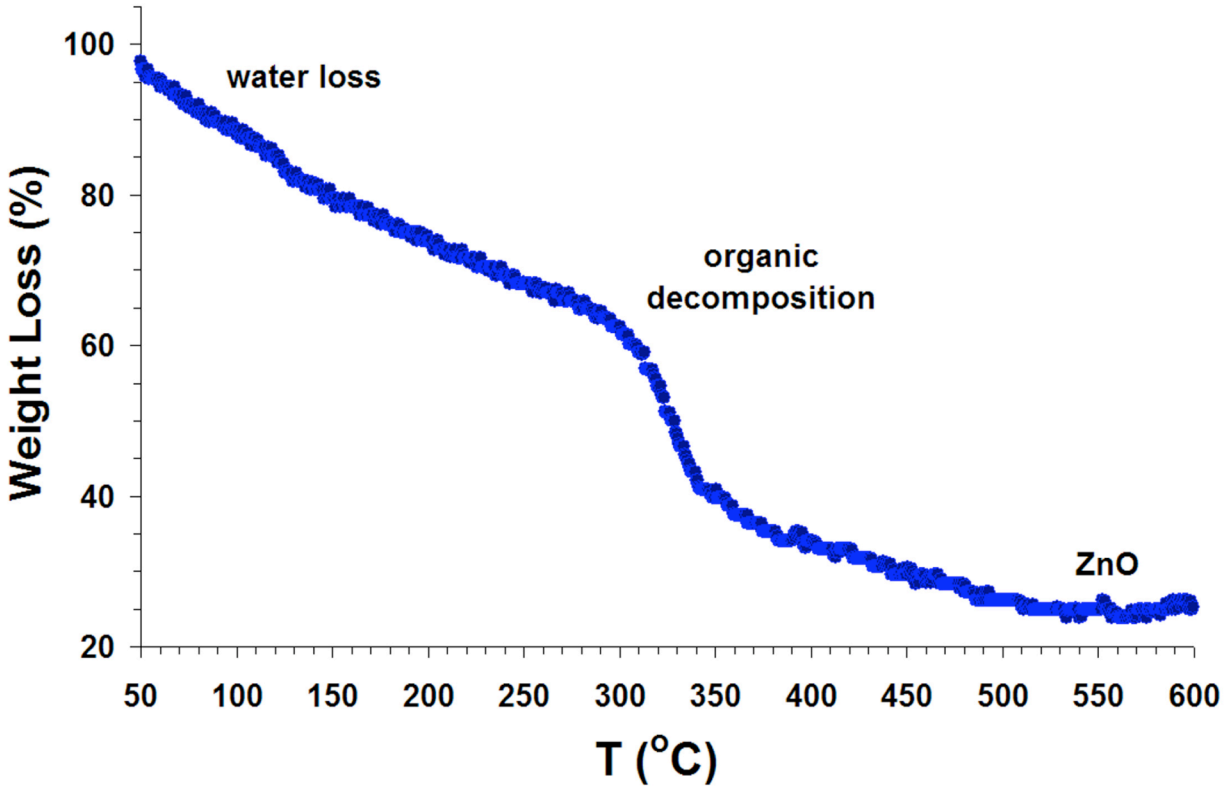

Figure 4.9. Thermogravimetric analysis (TGA) of electrodeposited hybrid film of 0.05 wt% PyBA in 1:1 (v/v) H_2O/DMSO 0.02 M $Zn(NO_3)_2$ solution.

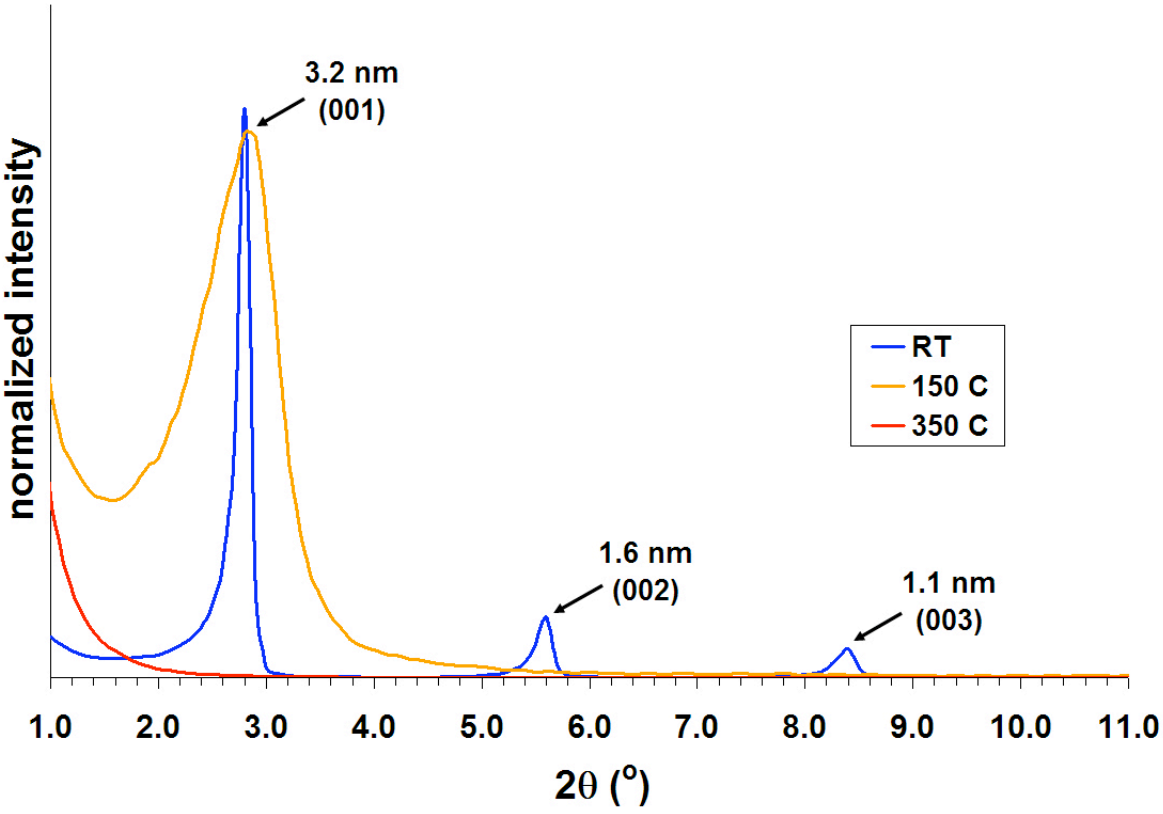

Figure 4.10. SAXS spectra of electrodeposited hybrid film of 0.05 wt% PyBA in 1:1 (v/v) H_2O/DMSO 0.02 M $Zn(NO_3)_2$ solution before and after heat treatments.

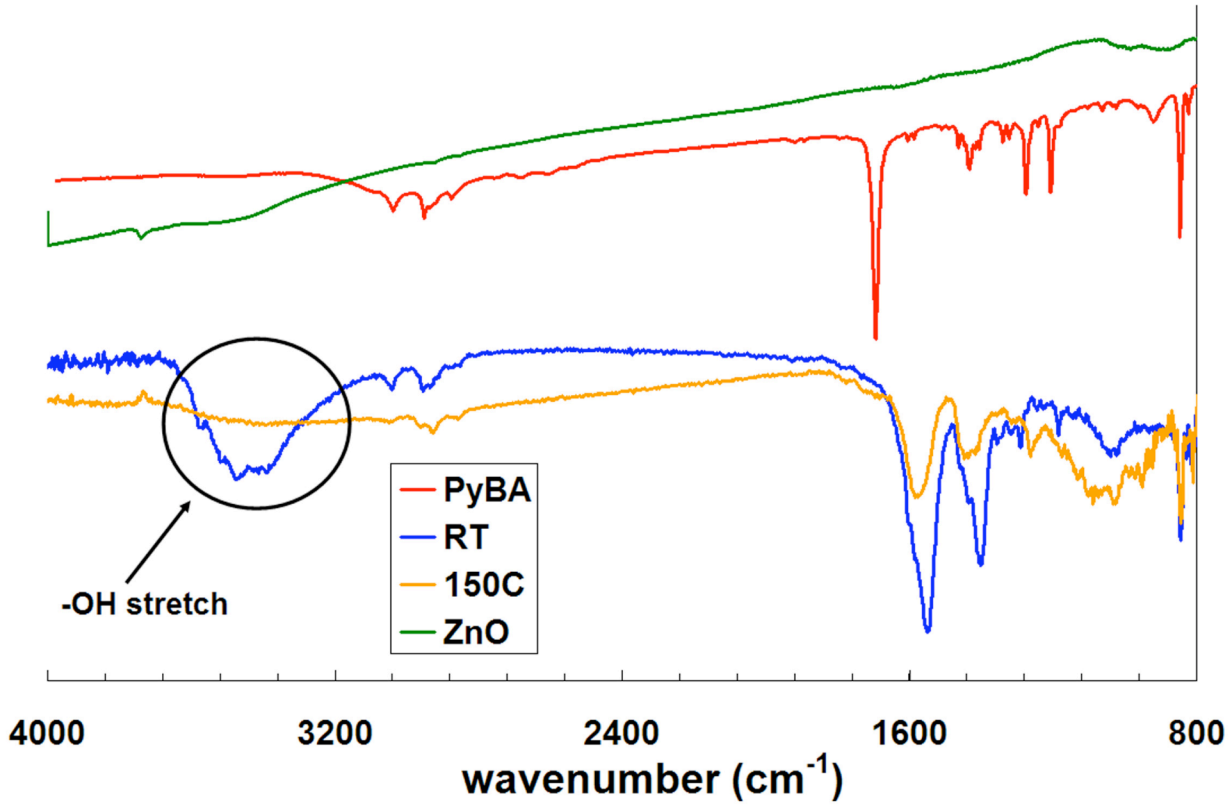

Figure 4.11. FT-IR spectra of ZnO and PyBA standards, and of electrodeposited hybrid film of 0.05 wt% PyBA in 1:1 (v/v) H_2O/DMSO 0.02 M $Zn(NO_3)_2$ solution before and after heat treatment.

conventional X-ray diffraction techniques are a measure of the averaged coordination environment for all elements present, XAS is an element-specific electron spectroscopic technique, and therefore was used to determine the identity of the zinc-rich lamellae generated.[142]

The XANES spectrum, or region within 30 eV from the absorption edge of zinc, identified the as-deposited hybrid film to consist of zinc hydroxide (see Figure 4.12 (a)). The spectrum closely matches that of the zinc hydroxide standard (α-$Zn(OH)_2$ nitrate derivative) and is also consistent with the observed energy value for the absorption edge of zinc hydroxide (~3.2 eV greater than the Zn K edge of 9658.6 eV). Remarkably, upon annealing the film to 150 °C, the XANES spectrum reveals the transformation of the inorganic phase to zinc oxide (see Figure 4.12 (b)). The absorption edge is shifted to 2.6 eV from the Zn foil, consistent with the bulk ZnO standard.[143]

The fourier transform of the EXAFS region, or extended spectrum of much higher electron kinetic regions, reveals more information on the crystal structure of the phases and bonding present. The first peak labeled in Figure 4.13 is for the Zn-O radial bond distance and the second peak labeled is the Zn-Zn bonding distance.

For the case of the 150 °C annealed sample, the Zn-O peak is consistent with the bond distance in the bulk ZnO standard, and does not change in distance or intensity with further annealing to 350 °C. All the zinc atoms, therefore, are terminated by oxygen atoms. This is in agreement with the fact that the zinc ions coordinate to the oxygen of the carboxylate during deposition. The attenuation of the Zn-Zn peak in the 150 °C annealed sample indicates a reduction in the coordination number, suggesting that the long-range ordering of the crystal

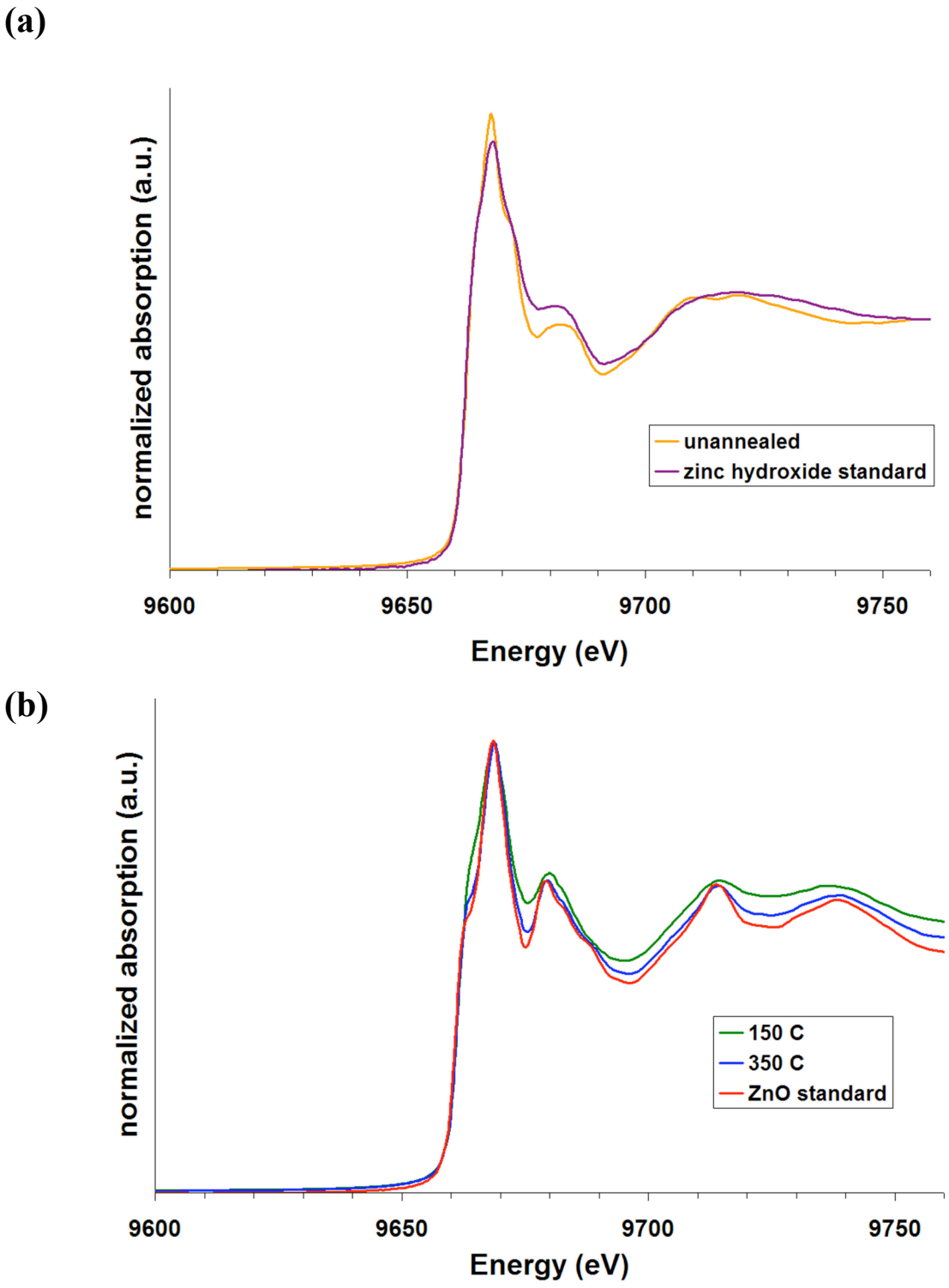

Figure 4.12. XANES spectra for electrodeposited hybrid films with PyBA. **(a)** α-$Zn(OH)_2$ powder standard and unannealed electrodeposited hybrid film with PyBA. **(b)** ZnO powder standard and annealed electrodeposited hybrid films with PyBA.

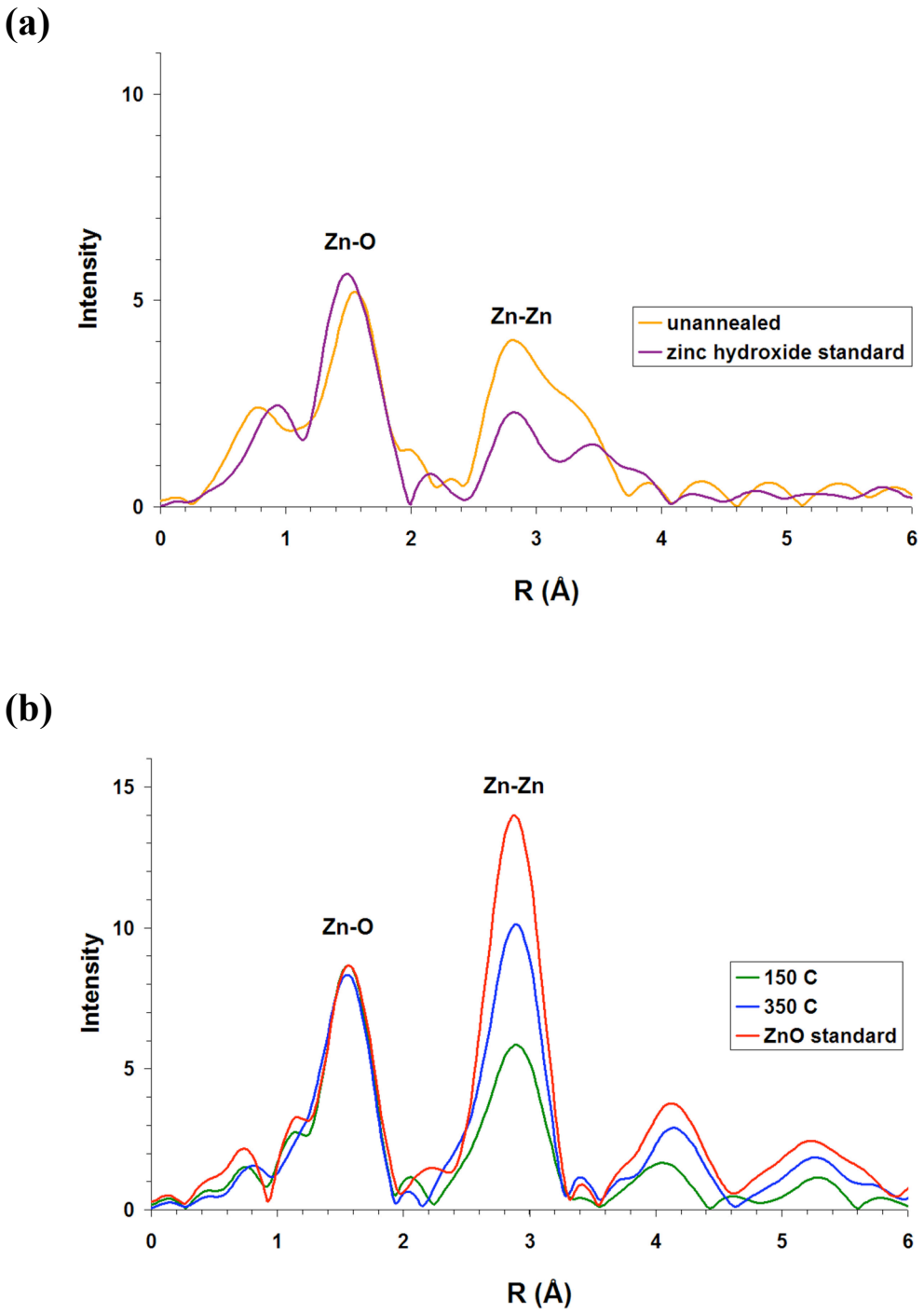

Figure 4.13. Radial bond distances (Zn-O and Zn-Zn) as a function of intensity calculated from normalized EXAFS spectra for **(a)** $Zn(OH)_2$ powder standard and unannealed electrodeposited hybrid film with PyBA, and **(b)** ZnO powder standard and annealed electrodeposited hybrid films with PyBA.

structure is affected by both a degree of disorder, as well as the limited dimension and 1D confinement of the Zn-rich layers. The 0.8-1.0 nm width of the inorganic layers would allow only a few atomic repeat distances to exist, and therefore, should in part cause this attenuation observed. This attenuation is lessened when the sample is annealed to 350 °C and the organic is decomposed, although the peak does not fully recover to the intensity of that of bulk ZnO, further elucidating the strong binding that exists between the inorganic and organic phases.

4.4.3 High-resolution TEM and electron diffraction

According to high-resolution TEM and electron diffraction, the zinc hydroxide phase present in the unannealed hybrid films is crystalline with a preferred orientation (see Figure 4.14). While the diffraction spots cannot be assigned to a specific zinc hydroxide crystal structure, the XAS results are similar to the layered α-$Zn(OH)_2$ nitrate crystal structure (see Figure 4.12 (a) and Figure 4.13 (a)). In the 150 °C annealed sample of PyBA/ZnO, TEM (see Figure 4.15) reveals that in fact the lamellar morphology is retained, however, it is not as regular as for the zinc hydroxide phase and while some regions exist with lattice fringes similar in value to the wurtzite ZnO peaks (see Figure 4.15 (b)), other regions appear to be amorphous (see Figure 4.15 (a)). This observation is similar to that revealed in the EXAFS measurements. No electron diffraction pattern was obtained, due in part to the fairly thin (< 1 nm) width of the ZnO stripes, as well as the partially amorphous nature.

4.4.4 Wide-angle X-ray scattering

As mentioned previously, WAXS measurements are an average of the coordination environment of all elements present, and therefore, the low concentration and dimensions of the inorganic phase coupled with the presence of the organic moieties makes the identification of

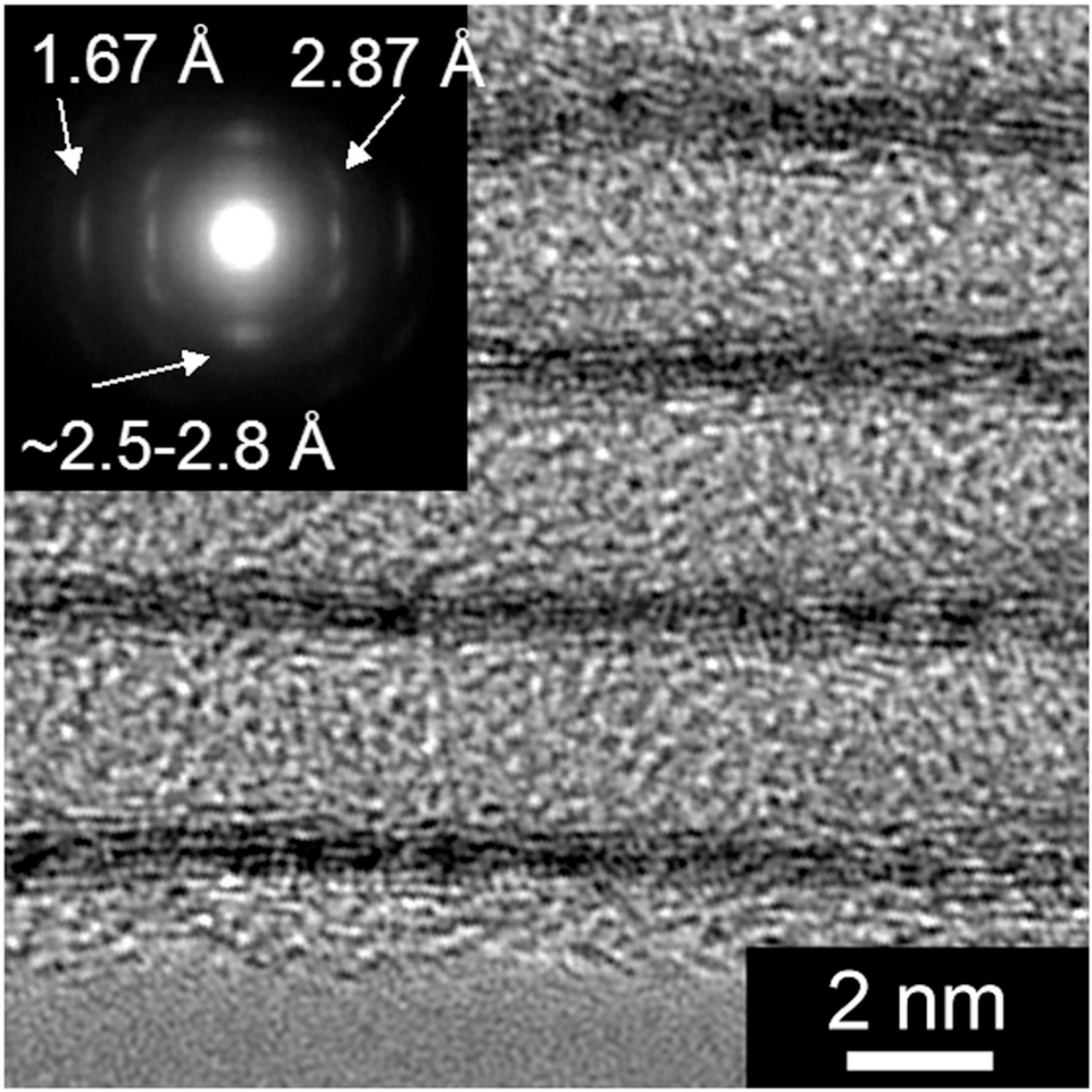

Figure 4.14. High-resolution TEM image of lamellar ordering of PyBA/$Zn(OH)_2$ hybrid (no annealing) with inset showing electron diffraction pattern.

(a)

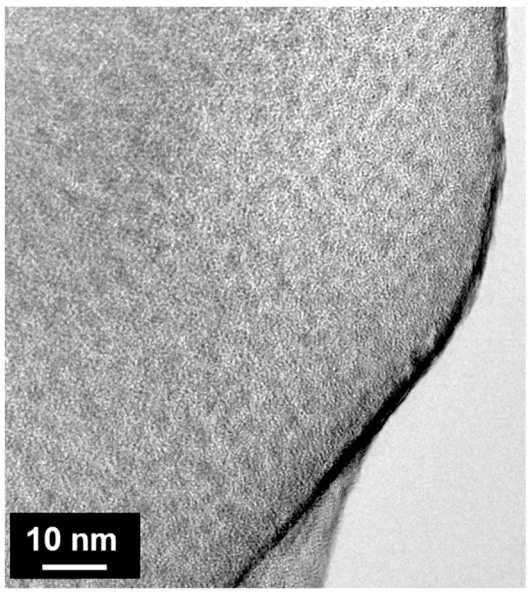

(b)

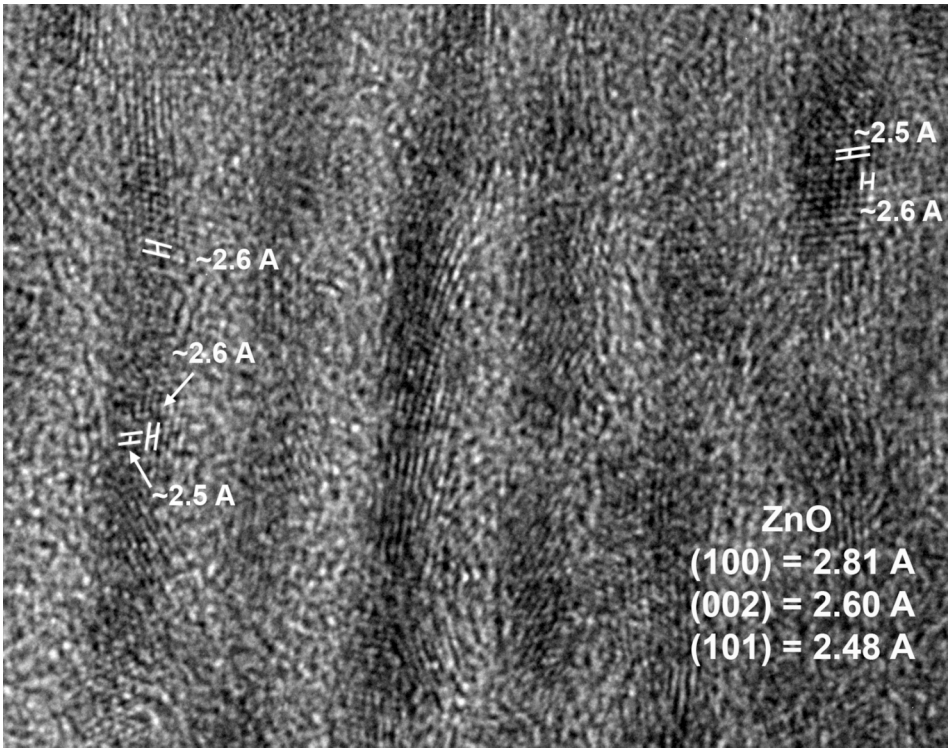

Figure 4.15. **(a)** TEM image of lamellar ordering of PyBA/ZnO hybrid (150 °C annealing). **(b)** High-resolution TEM image of PyBA/ZnO hybrid with indexing of lattice fringes.

peaks difficult. The spectra for both unannealed and annealed PyBA hybrid films are consistent, however, with the high resolution TEM and ED results (see Figure 4.16). The unannealed sample reveals a number of broad peaks, including ones in the 2.5-2.7 Å regime, whereas no identifiable peaks are present in the 150 °C annealed sample, due to both the decrease in crystallinity and domain size.

4.5 Influence of Organic Surfactant on Hybrid Self-Assembly

4.5.1 Hybrid nanostructure from non-conjugated surfactants

Non-conjugated surfactants were also used in the electrochemical synthesis in an effort to elucidate the role of the conjugated moiety on the overall nanostructure, as well as its integrity upon annealing. For this purpose, SDS (see Figure 4.17 (a)), which has previously been used in the literature in a similar electrochemical synthesis, was initially explored.[90, 144] The solvent mixture 1:1 (v/v) H_2O/DMSO resulted in no hybrid nanostructure being formed, and therefore, an aqueous solution was used instead. SDS, as opposed to PyBA, is fully soluble in water. The SAXS spectrum identified the presence of two lamellar phases, the first with a periodicity of 3.1 nm, and the second with a periodicity of 2.8 nm (see Figure 4.17 (b)). The XANES spectrum further confirms in Figure 4.17 (c) that the despite what was previously reported,[90, 144] SDS also generates zinc hydroxide, and not zinc oxide, at room temperature. Annealing to 150 °C, in this case, however, leads to a complete collapse of the nanostructure and the lamellar ordering is no longer retained. These results are consistent with the formation of layered zinc hydroxide in an aqueous solution of SDS at room temperature reported when using a pulsed-laser ablation synthesis rather than electrodeposition.[145] As reported by the authors, annealing to 150 °C was

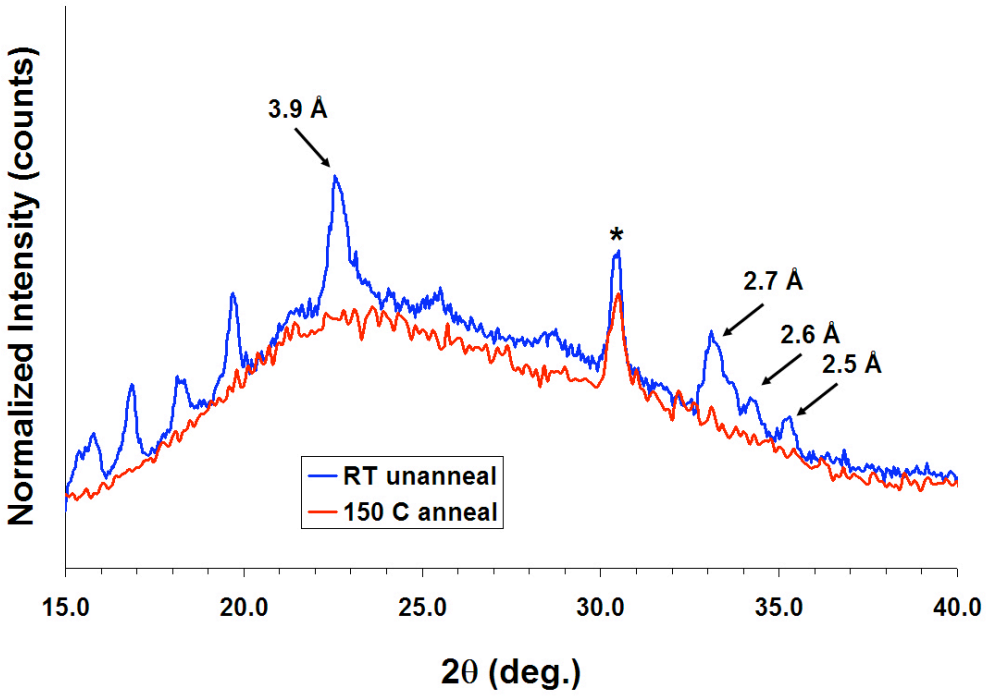

Figure 4.16. WAXS spectra of electrodeposited hybrid film of 0.05 wt% PyBA in 1:1 (v/v) H_2O/DMSO 0.02 M $Zn(NO_3)_2$ solution before and after annealing. Asterisk indicates peak due to ITO substrate.

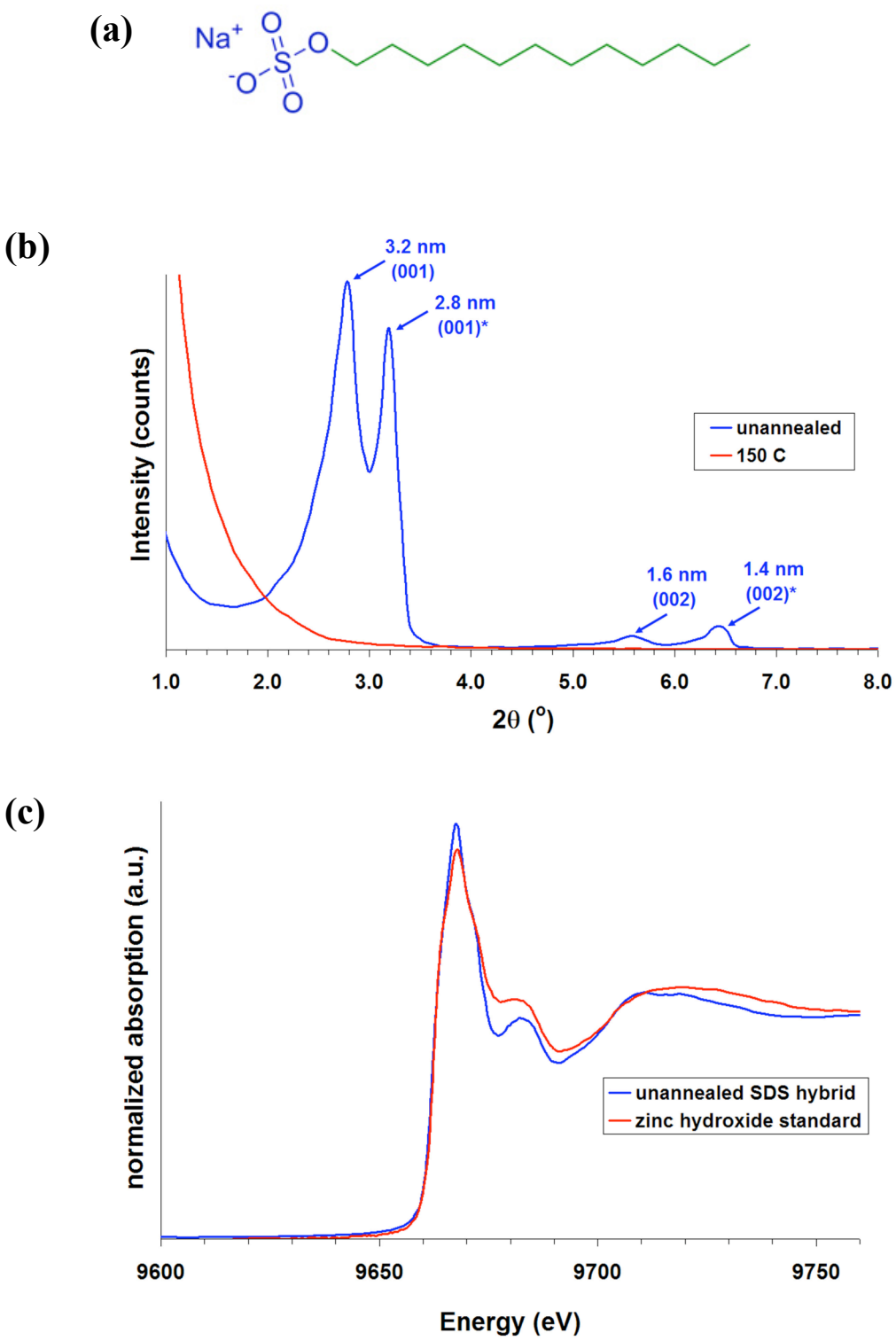

Figure 4.17. **(a)** Chemical structure of SDS. **(b)** SAXS spectra of electrodeposited hybrid film with SDS before and after heat treatment. **(c)** XANES spectra of $Zn(OH)_2$ powder standard and of electrodeposited hybrid film with SDS and no heat treatment.

also required with that synthetic approach for conversion, leading to a collapse of the overall nanostructure.[145]

For a more direct comparison to the PyBA, dodecanoic acid, which also has a carboxylic acid end group, but again lacks a conjugated moiety (see Figure 4.18 (a)) was also tested. At 0.05 wt%, the dodecanoic acid was near its solubility limit in water. The SAXS spectrum of the as-deposited hybrid film reveals a number of peaks (see Figure 4.18 (b)). These peaks could be indexed to three separate lamellar phases. While the peaks do not match the indexing of any common cubic phases, it is possible that a higher ordered cubic phase is instead generated. Nonetheless, most of the peaks disappear at 150 °C, and at 200 °C, only the 1.5 nm peak is present. This result suggests that while the carboxylate binds more strongly to the growing inorganic phase compared to sulfate, the π-π conjugation stacking is crucial to the stability of the overall nanostructure and thermal robustness of the hybrids formed.

4.5.2 Influence of alkyl chain on overall assembly

When the alkyl tail of the PyBA was eliminated and the shorter-length and more rigid surfactant, pyrenecarboxylic acid (PyCA), was used, platelet nanostructures with lamellar ordering were also generated (see Figure 4.19). The decrease in the extended length of the surfactant (0.9 nm) also resulted in a decrease in the periodicity of the lamellae (2.5 nm). Annealing to 150 °C also led to a disappearance in the higher order lamellar peaks and an increase in the first-order peak width. Film deposition was slower, however, which may be attributed to a difference in the pKa value of PyCA compared to PyBA since the driving force for deposition is an increase in the local pH of the solution.

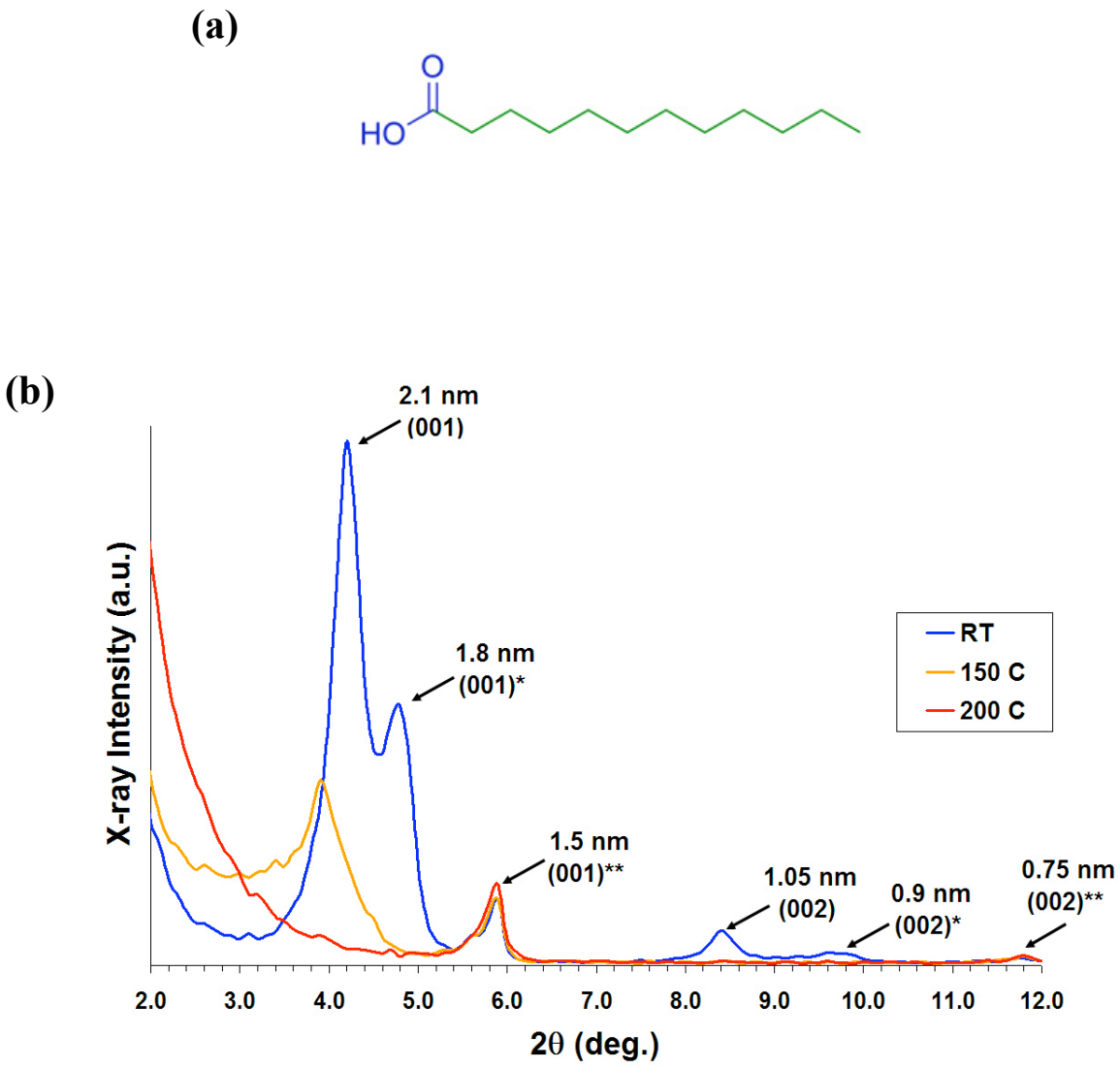

Figure 4.18. **(a)** Chemical structure of dodecanoic acid. **(b)** SAXS spectra of electrodeposited hybrid film with dodecanoic acid before and after heat treatment.

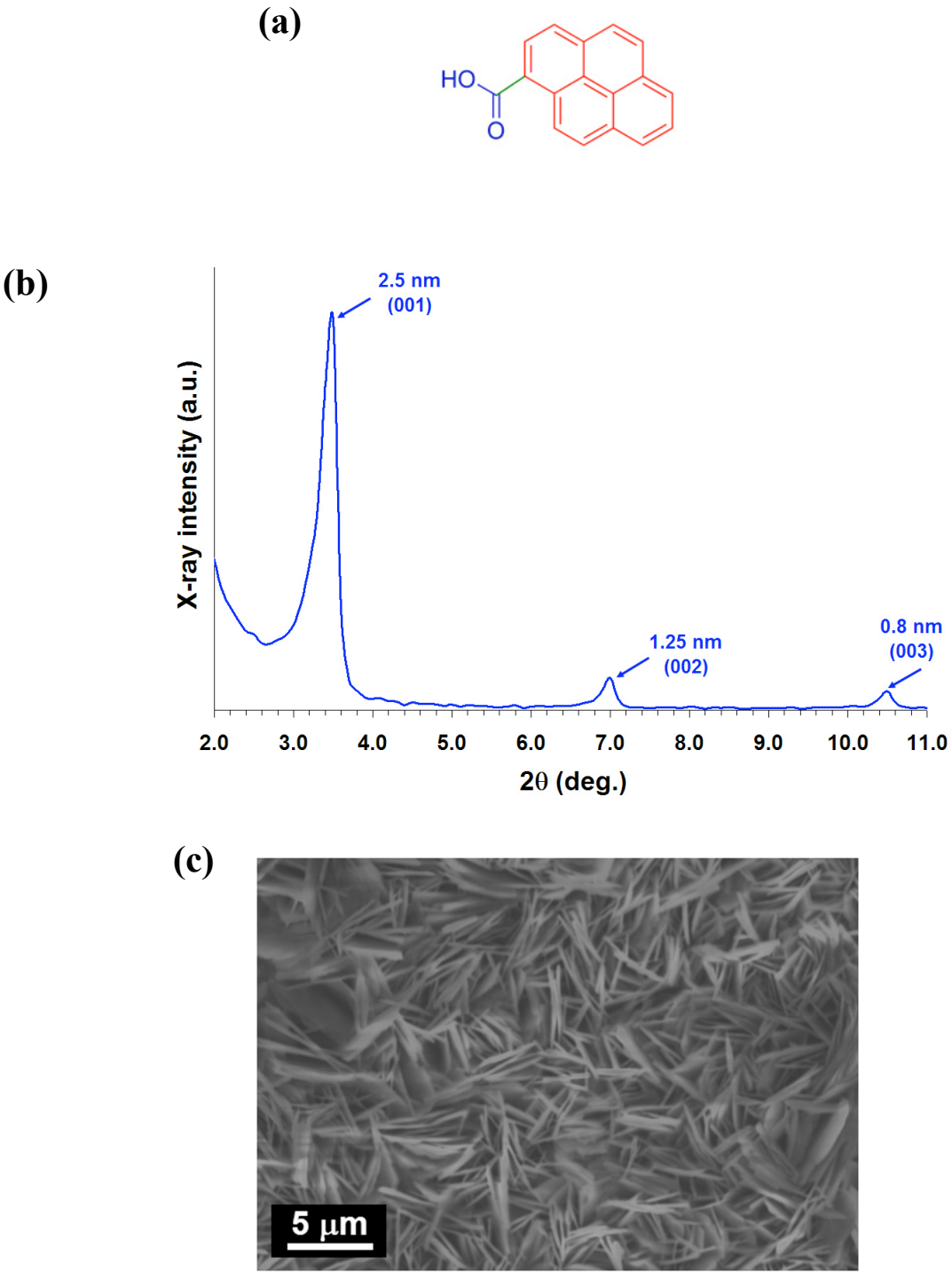

Figure 4.19. **(a)** Chemical structure of PyCA molecule. **(b)** SAXS spectrum of electrodeposited hybrid film from 0.05 wt% PyCA in 1:1 (v/v) H_2O/DMSO 0.02 M $Zn(NO_3)_2$ solution. **(c)** SEM image of platelets generated.

4.5.3 Structural characterization with thiophene moieties

Because both pyrene and ZnO absorbs in the UV range, it is necessary to substitute the pyrene chromophore with one that absorbs in the visible range in order to capture a larger region of the solar spectrum. In addition, a moiety that absorbs at lower energies that ZnO will allow the study of the influence of the organic substituent on the conducting properties of the hybrid materials Thiophene derivatives have previously been used with ZnO in the design of hybrid solar cells.[146] To first confirm that hybrid lamellar ordering could be attained by simply changing the chromophore segment, a terthiophene carboxylic acid (3T-CA) was tested (see Figure 4.20 (a)). As expected, lamellar ordering was obtained with a slight increase in the periodicity (4.0 nm) due to an increase in the extended molecular length (1.3 nm). The presence of sulfur in the organic chain allowed for EDS analysis to be performed. Remarkably, a periodicity is observed in the zinc profile (see Figure 4.21) that closely matches that of the lamellar periodicity. The atomic ratio of S:Zn is determined to be 1.77:1 (+/- 0.16). This corresponds to an average of 0.59 (+/- 0.05) 3T-CA molecules per 1 atom of zinc.

Based on the results of the terthiophene derivative, a thiophene moiety with an absorption beyond 400 nm was targeted for future photovoltaic testing. For this purpose, the dicarboxylic acid 3-methyl-quinquethiophene (5T-DCA) bolaamphiphile was synthesized with details of the synthesis described in detail in Appendix I.3 (see Figure 4.22). The 5T-DCA was synthesized as a bolaamphiphile in order to aid in the solubility of the quinquiethiophene segment. In addition, the carboxylic acids were added to the ends of the conjugated block because attempts at electrodepositing nanostructures from surfactants that were mid-functionalized proved unsuccessful. Due to the presence of two binding sites, the concentration of surfactant was

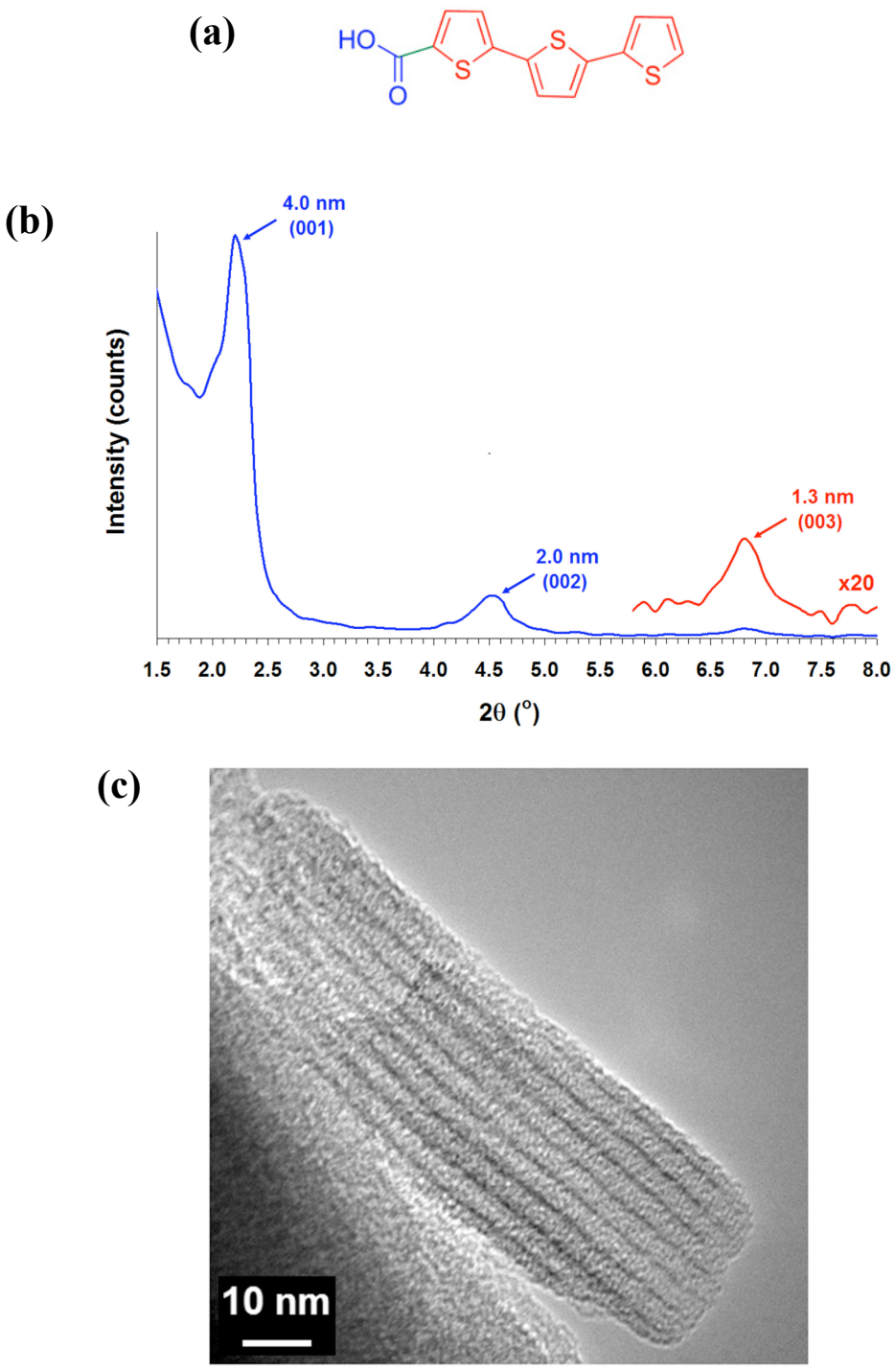

Figure 4.20. **(a)** Chemical structure of 3T-CA molecule. **(b)** SAXS spectrum of electrodeposited hybrid film from 0.05 wt% 3T-CA in 1:1 (v/v) H_2O/DMSO 0.02 M $Zn(NO_3)_2$ solution. **(c)** TEM image of lamellae generated.

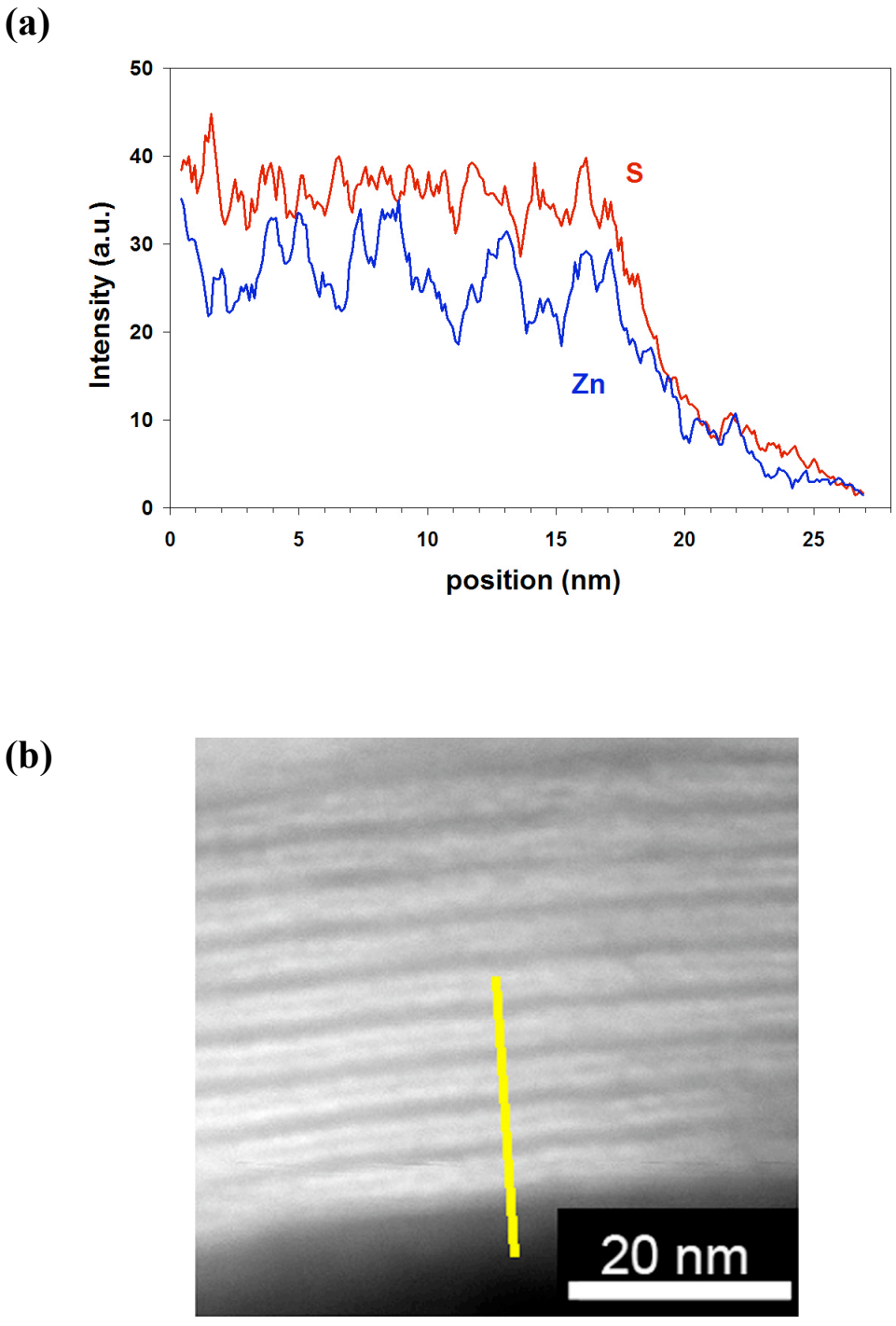

Figure 4.21. **(a)** EDS line spectrum along hybrid lamellae of electrodeposited film from 3T-CA and **(b)** TEM image showing line profile used.

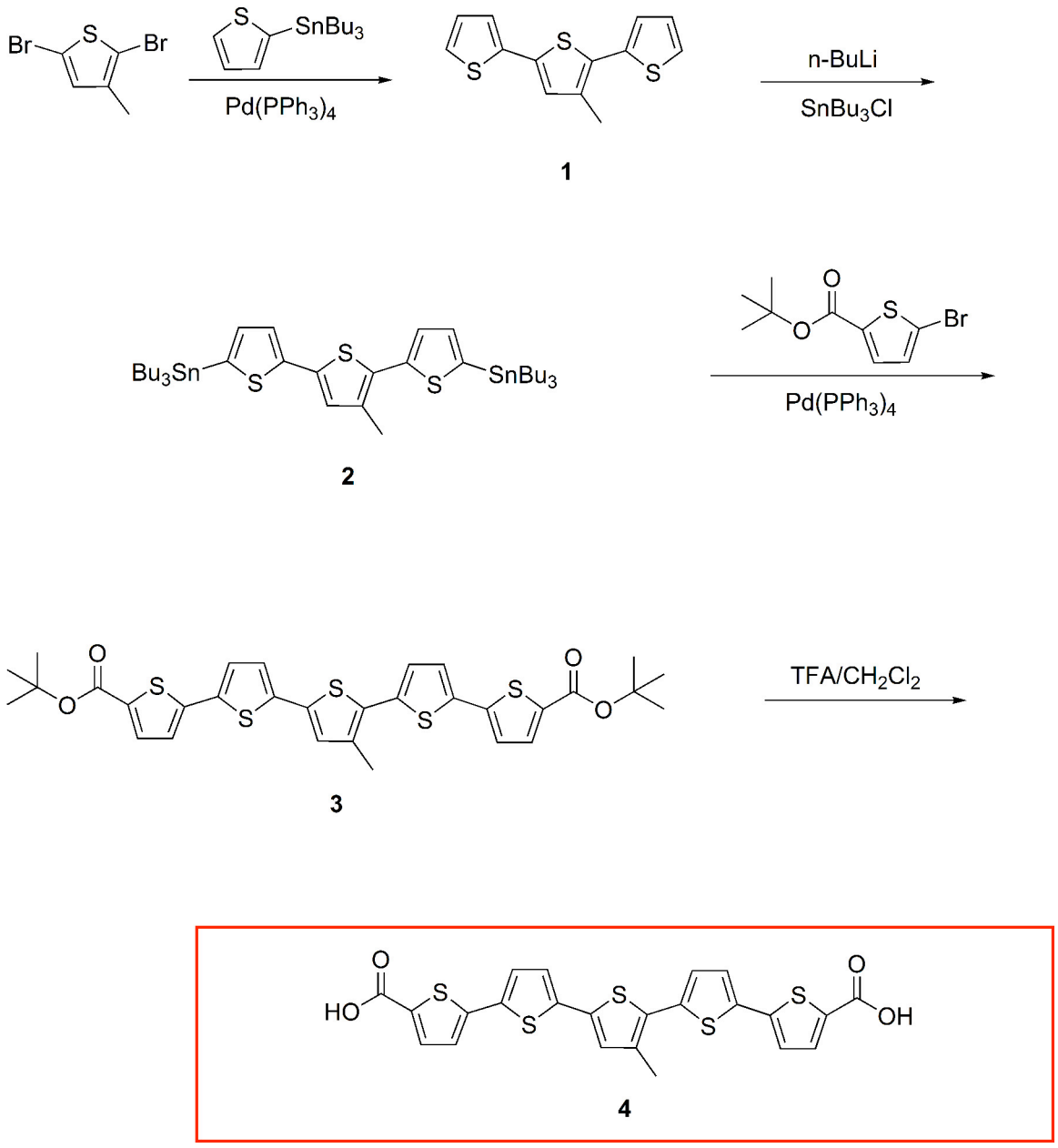

Figure 4.22. Chemical synthetic scheme for 5T-DCA. The four step reaction has an overall yield of ~73%. (prepared by David Stone).

proportionally decreased by a factor of two. Lamellar ordering is attained, as characterized by SAXS and STEM in Figure 4.23, with a periodicity of 2.5 nm. The smaller spacing is attributed to the fact that the organic region is composed of single layers, as opposed to bilayers when only one binding site existed. In this case, the inorganic phase binds to both ends of the surfactant. In addition, the greater atomic number of sulfur leads to less contrast difference between the organic and inorganic domains. EDS analysis of the average of 10 random lamellar sheets yielded a S:Zn atomic ratio of 3.04 : 1 (+/- 0.17) This corresponds to an average of 0.61 (+/- 0.03) molecules of 5T-DCA per 1 atom of Zn. Interestingly these numbers are statistically the same as the ones obtained for 3T-CA. This ratio of molecules is greater than the density of molecules in the α–$Zn(OH)_2$ crystal structure stoichiometry ($Zn_5(OH)_8(NO_3)_2$).

4.6 Optical and Electronic Properties of Hybrid Nanostructures

As a preliminary investigation of the optical and electronic properties of the hybrid nanostructures, the effects of the annealing process were studied. Specifically, I-V measurements were made on both the as-deposited hybrid film at room temperature and subsequently upon annealing to 150 °C and conversion of the $Zn(OH)_2$ phase to ZnO (see Figure 4.24). A significant increase in the conductivity is observed with this conversion. In addition, the fluorescence of the pyrene is quenched by two orders of magnitude (see Figure 4.25), as is evident when illuminating a device with UV light. As shown in Figure 4.26, the ZnO phase is further observed to be photoconductive in the hybrid nanostructure. Preliminary photovoltaics measurements displayed relatively weak performance due in large part to lack of a sufficient electron-blocking layer to prevent shorting by sufficiently coating the ZnO so that the top metal layer contacts the organic surfactant without contacting the ZnO. The use of P3HT is currently

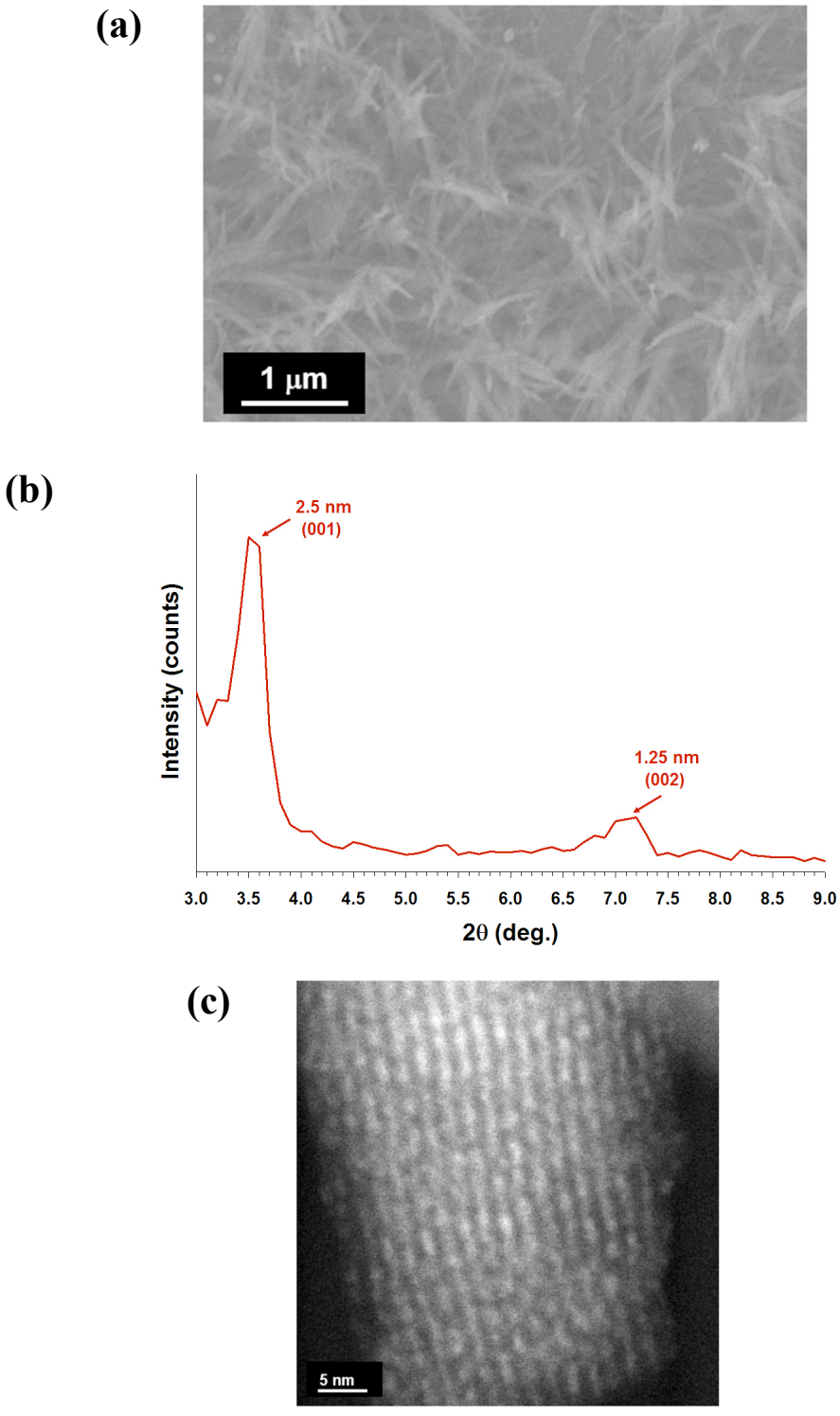

Figure 4.23. **(a)** SEM image of platelet structures generated by electrodeposited hybrid film from 0.025 wt% 5T-DCA in 1:1 (v/v) H_2O/DMSO 0.02 M $Zn(NO_3)_2$ solution. **(b)** SAXS spectrum indicating lamellar ordering. **(c)** STEM image of lamellae generated.

(a)

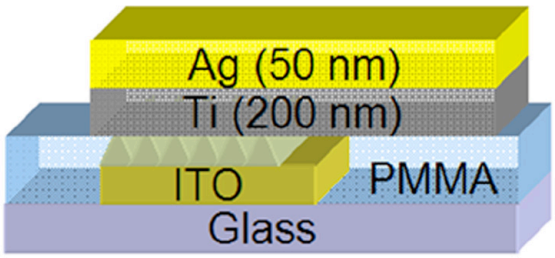

(b)

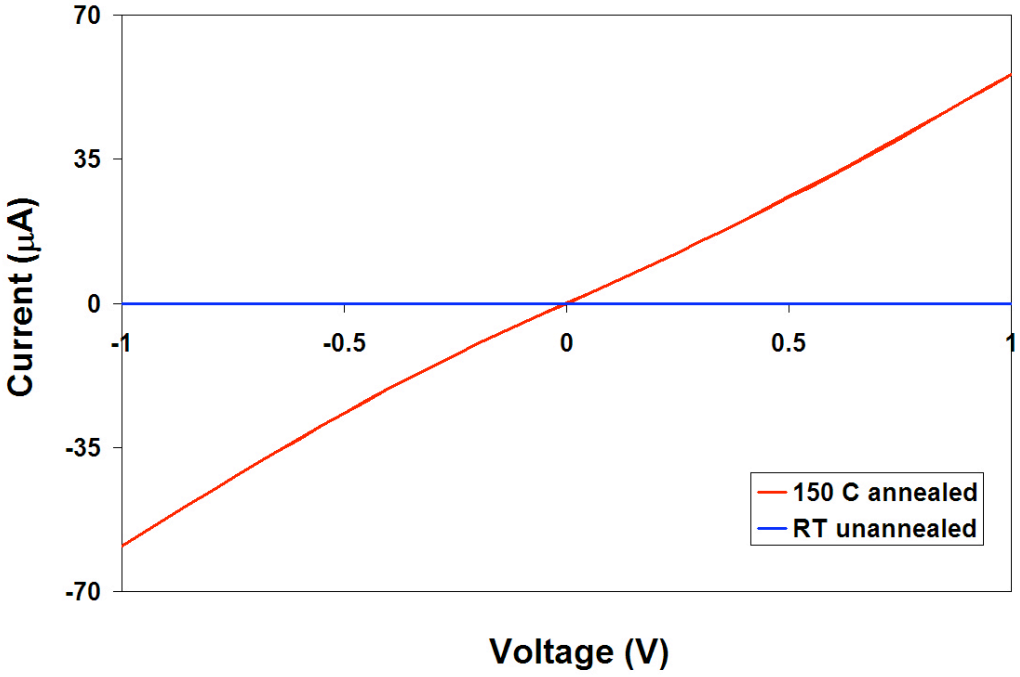

Figure 4.24. **(a)** Schematic illustration of device with electrodeposited hybrid active matrix with PyBA and patterned ITO and Ti/Ag electrodes. **(b)** I-V measurements of hybrid as-deposited film at room temperature (blue) and after annealing at 150 °C and conversion of $Zn(OH)_2$ to ZnO (red).

(a)

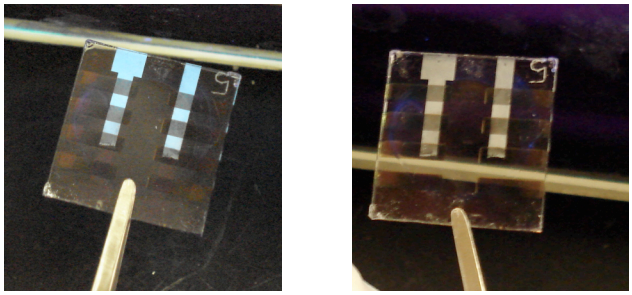

(b)

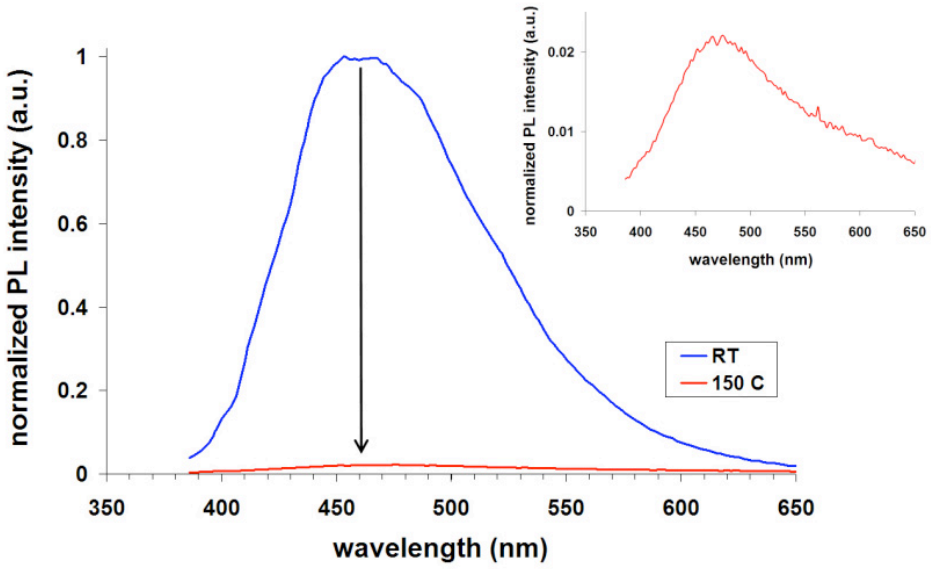

Figure 4.25. **(a)** Photographs of electrodeposited hybrid films with PyBA on patterned ITO devices under UV-light illumination of as-deposited film at room temperature (right) and film after annealing at 150 °C and conversion of $Zn(OH)_2$ to ZnO (left). **(b)** PL emission of PyBA for hybrid film before and after annealing (ex. 342 nm) with intensity showing magnified view of PyBA/ZnO hybrid.

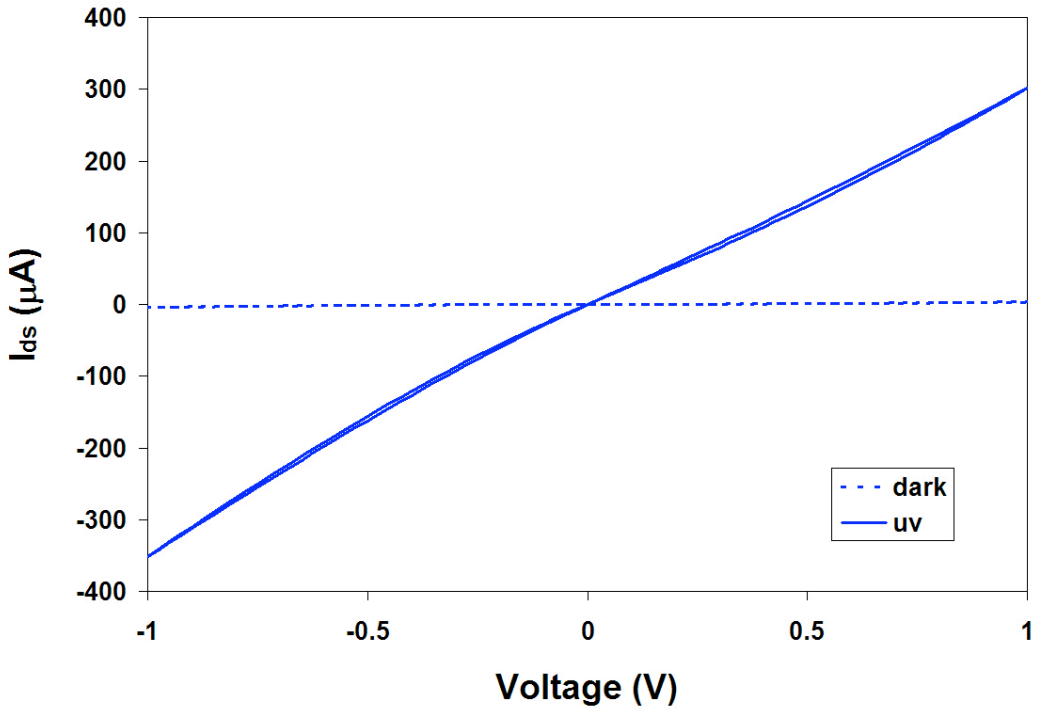

Figure 4.26. I-V measurement of electrodeposited hybrid films with PyBA/ZnO under dark and UV light (365 nm) illumination indicating photoconductivity of ZnO.

being investigated as an electron-blocking layer and device fabrication being optimized for testing of both the PyBA and the 5T-DCA hybrids.

4.7 Summary and Outlook

The growth of dense, high-aspect-ratio features of hybrid electronically active materials consisting of alternating layers of n-type inorganic and p-type organic layers is a promising target for photovoltaics. Toward this goal, self-assembled lamellar nanostructures of n-type ZnO sheets separated by sheets of p-type organic surfactants attached to carboxylic acid end groups, have been attained. Annealing to 150 °C is necessary to convert the as-deposited lamellar sheets of $Zn(OH)_2$ intercalated with the organic surfactants into ZnO via water loss. Remarkably, the lamellar ordering is still present with the ZnO phase upon this conversion. The conjugated aromatic p-type segment is discovered to not only be important for further optical applications, but also in the retention of the lamellar ordering upon conversion to ZnO. The use of non-conjugated surfactants resulted in a collapse of the nanostructure when annealed. Furthermore, preliminary electrical measurements show that the ZnO sheets formed are electronically active and photoconductive. This approach is also successful in optimizing the properties of the organic moiety by simply changing the chemical identity. This methodology should be capable of being extending into a wide array of hybrid vertically oriented lamellar materials comprised of conducting n-type inorganic and p-type organic layers. The challenge now is in growing these alternating n-type and p-type layers so that they lie perpendicular to the electrode, creating continuous pathways for charge transport and collection (see Figure 4.27). We postulate that we can achieve such vertically oriented growth when there is a high density of growing crystallites for two possible reasons. First, the rate of electrochemical deposition is influenced by the flux of

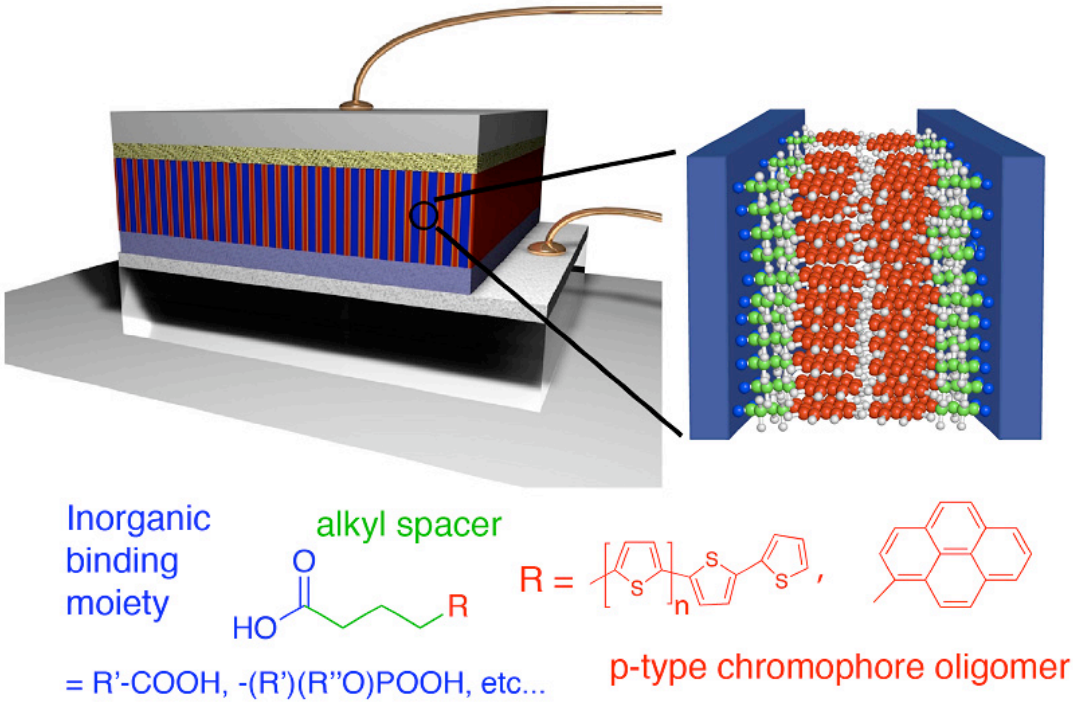

Figure 4.27. Schematic illustration of a photovoltaic device consisting of an active matrix of all vertically-oriented alternating lamellar sheets of the n-type ZnO inorganic phase (blue) and a p-type organic phase (red) with zoomed in molecular graphics of one of the lamellae and general structure of the p-type organic surfactants used.

precursor molecules to the growing liquid-solid interface. Crystallites having a growth direction oriented perpendicular to the substrate should see a greater flux of unreacted precursors during growth, and consequently grow faster and larger. Second, crystallites that are oriented in an off-vertical direction will eventually collide with another growing crystallite and either terminate or reorient. These two effects have been shown to play a role in ZnO nanowires.[147, 148]

4.8 Experimental

Oligothiophene amphiphiles were synthesized by David Stone and Weiwen Tsai of the author's laboratory. Characterization of the hybrid films was carried out in collaboration with Dr. Joshua Goldberger, also of the author's lab, who performed device measurements and some of the structural characterization.

4.8.1 Organic surfactant synthesis

The terthiophene carboxylic acid (3T-CA) amphiphile was synthesized by Weiwen Tsai, of the author's laboratory, by a procedure adapted from the literature.[140] The dicarboxylic acid 3-methyl-quinquethiophene (5T-DCA) bolaamphiphile was synthesized by David Stone, of the author's laboratory, as described in Appendix I.3 (Figure 4.23). The remaining surfactants used were all commercially available. 1-Pyrenebutyric acid (PyBA) (97% purity) and dodecanoic acid (99% purity) were purchased from Aldrich. 1-Pyrenecarboxylic acid (PyCA) (98% purity) was purchased from Alfa Aesar and sodium dodecyl sulfate (SDS) (ultrapure bioreagent) was purchased from J.T. Baker.

4.8.2 Electrochemical synthesis

The electrochemical syntheses were run on a computer controlled EG&G Princeton Applied Research potentiostat model 263A using a conventional three-electrode set-up in an

undivided cell. For device measurements, the working electrodes used were 2.0 cm^2 glass substrates with pre-patterned indium-doped tin oxide (ITO) (140 nm thick, ~50 Ω sheet resistance, Kintek). Substrates were cleaned prior to use by gently scrubbing with a 2% alkinox soap solution using a cotton swab, rinsing with water (Millipore Milli-Q-purified, 18.3 MΩ cm) three times, and UV-zone treating for 20 minutes. For all other characterization, the working electrodes used were 2.5 cm x 2 cm ITO-glass (120 nm thick, ~100 Ω sheet resistance, Applied Thin Films) or FTO-glass (TEC#8/3, ~9Ω sheet resistance, Hartford Glass). Substrates were cleaned prior to use by sequential ultrasonication (10 min. each) in acetone, isopropanol, and 2% alkinox soap solution. Rinsing in water (Millipore Milli-Q-purified, 18.3 MΩ cm) was followed by a 15 sec. dip in 5M HCl and subsequent rinsing in water. Substrates were then dried under a stream of dry N_2.

Solutions were prepared by dissolving 1.5-3.0 mg of surfactant in 6 mL of 0.02 M zinc nitrate hexahydrate ($Zn(NO)_3 \cdot 6H_2O$) (98% purity, Aldrich) in a glass cell vial (BAS Inc. model MF-1082). Solutions, therefore, consisted of 0.025-0.05 wt% surfactant. To remove all trace metal and organic impurities, the cell vials were cleaned in an aqua regia solution ((3:1 (v/v) HCl/HNO_3) for 15 min., rinsed three times with water (Millipore Milli-Q-purified, 18.3 MΩ cm), dried under a stream of dry N_2, and stored in an oven at 110 °C to remove residual water. Unless otherwise noted, the zinc nitrate solution was a 1:1 (v/v) mixture of $DMSO/H_2O$. The water used was purified by a Millipore filtration system to a resistivity of 18.3 MΩ cm. Solutions were ultra-sonicated to insure full mixing of the surfactant into the electrolyte solution. Prior to electrodeposition, solutions were purged for 20 min. with Ar under constant magnetic stirring at 80 °C.

Unless otherwise noted, the following electrodeposition procedure was used. Working electrode substrates were placed upright in the glass cell vial not touching but within 2.5 cm (vial diameter) from the counter electrode (1.0 mm diameter-Zn wire (99.9997% purity, Alfa Aesar)) and the reference electrode (Ag/AgCl in a 3 M NaCl solution (BAS Inc. model RE-5B)). To prevent solvent evaporation during deposition, all three electrodes were inserted into the cell vial through the three openings of a teflon cell top (BAS Inc. model MR-3750). Deposition was achieved potentiostatically at -0.9 V for 30 min.-24 hr., depending on the growth time. The cell vial was kept under constant magnetic stirring at 80 °C throughout the deposition. All deposited films were rinsed by water and ethanol and then dried under a stream of dry N_2. For temperature-dependent studies, unless otherwise noted, deposited films were subsequently annealed under N_2 for 12 hr. at the designated temperature.

4.8.3 Synthesis of powder standards

ZnO nanoparticles (99.999%, Nanotek) as a standard for FT-IR, powder XRD, and XANES measurements were purchased from Aldrich. Layered α-$Zn(OH)_2$ and β-$Zn(OH)_2$ standards were synthesized from the procedure reported by Ogata et al.[149] All solutions were prepared using DI H_2O (18.2 MΩ) that was degassed by bubbling Ar for 1 hr. Two 60 mL 0.17 M aqueous solutions of $Zn(NO)_3 \bullet 6H_2O$ (99.9% purity, Aldrich) were prepared. The solutions were stirred at 5 °C while either 36 mL or 60 mL of a 0.23 M NaOH solution was prepared to synthesize either α-$Zn(OH)_2$ or β-$Zn(OH)_2$, respectively. Both solutions were stirred at 5 °C for 1 hr. and cloudy white suspensions were obtained. The products were filtered, washing three times with H_2O. The resulting precipitates were dried at room temperature for 24 hrs. The β-$Zn(OH)_2$ sample was annealed at 60 °C for 4 hr. Small and wide-angle XRD analysis showed a

homogeneous single phase of the α-$Zn(OH)_2$ nitrate derivative (actual stoichiometry: $Zn_5(OH)_8(NO_3)_2 \bullet 2H_2O$)[150] for the α-$Zn(OH)_2$ synthesis procedure. The β-$Zn(OH)_2$ product showed trace impurity reflections (Intensity < 5%) that could be assigned to the δ-$Zn(OH)_2$ phase. The δ-$Zn(OH)_2$ structure is thought to be a H_2O intercalated version of the layered β-$Zn(OH)_2$, exhibiting the same Zn coordination environment.[151] Therefore, the presence of trace δ-$Zn(OH)_2$ impurities is not expected to interfere with the XAS measurements.

4.8.4 Electron and optical microscopy

SEM was performed on a Hitachi S-4800-II cFEG, a LEO Gemini 1525 sFEG, and a FEI Quanta sFEG operating at 5-25 kV. Images were captured by a CCD camera.

TEM samples were prepared on lacey formvar/carbon 300 mesh Cu grids (Ted Pella, Inc.) by gently contacting the grid with the carbon-coated side face down over the deposited film for transfer. Grid coverage was inspected with an optical microscope. Samples were imaged at 200 kV on a JEOL JEM-2100F TEM. Images and electron diffraction patterns were recorded using a Gatan CCD camera. Electron diffraction patterns were calibrated against a gold standard, and measured digitally in Adobe Photoshop. EDS line and map scans were performed using the Inca Software.

Optical microscopy images were prepared using a Nikon Eclipse ME600 microscope and attached CCD camera.

4.8.5 X-ray scattering

XRD patterns were recorded using a Rigaku ATX-G X-ray diffractometer at an operating power of 50 kV and 240 mA with a CuKα (8.05 keV, 1.54 Å) source.

4.8.6 FT-IR spectroscopy

Approximately 5 mg of ZnO and PyBA standard powders were ground for 10 min. in a mortar and pestle with 0.5-1.0 g of KBr salt and pressed into a 7 mm diameter pellet. For PM-IRRAS measurement, samples were electrochemically deposited onto a 100 nm Ag thin film thermally evaporated onto a 3 in. x 1 in. glass slide that was O_2 RIE-cleaned (5 min. on both sides at 100 W, 50 sccm O_2).

Measurements were made using a Thermo Nicolet, Nexus 870 FTIR spectrometer. The FTIR data was collected at 4 cm^{-1} resolution in transmission mode for the ZnO and PyBA standards, and in polarization modulation-infrared reflection-absorption spectroscopy (PM-IRRAS) mode for the electrodeposited films. 128 and 1024 scans were collected and averaged for each transmission and PM-IRRAS spectrum, respectively. PM-IRRAS spectra were recorded at grazing incidence reflection mode using a tabletop optics module (TOM). The spectrometer and TOM were purged with nitrogen gas, and the incident angle of the polarization-modulated light was set to 80° relative to the surface normal.

4.8.7 X-ray absorption spectroscopy

XANES/EXAFS measurements were carried out at the 5-BM-D beam line of the APS using an Oxford-Danfysik ion chamber to monitor the incident beam intensity and a 13 element Ge solid state detector to detect the Zn Kα fluorescence. The monochromater consisted of two Si(111) crystals. Samples were measured in fluorescence mode and mounted at a 45° angle from the detector with an incident slit of 2 mm x 5 mm (v x h). Powder standards were smeared onto a piece of scotch tape and measured in transmission mode. The energy was calibrated using a Zn reference foil spectrum. All spectra were merged, background-subtracted and normalized to

maximum absorption using Athena, Version: 08.53 (Bruce Ravel, U. Chicago, 2007).

4.8.8 Photoluminescence spectroscopy

Photoluminescence spectra were measured using a Horiba Jobin-Yvon (Edison, NJ) Nanolog-3 fluorimeter with band pass slit widths set to 0.5 nm (excitation) and 1 nm (emission). Samples were mounted at an angle of 60° from the detector to minimize direct scatter of the excitation beam into the detector. The same area of the samples was measured before and after annealing.

4.8.9 Conductivity measurements

For direct conductivity measurements, after the ZnO/PyBA active layer was electrochemically deposited onto the pre-patterned ITO anode substrate, a photoresist protective layer (PMMA, Microchem Corp.) was spun-cast onto the sample and dried under vacuum for 4-24 hr. to remove solvent to prevent shorting between the top metal and bottom ITO electrode. The substrates were then RIE cleaned in 50 sccm O_2 at 100W for 1 min, and immediately loaded into an electron beam evaporator equipped with a substrate temperature monitor. For the top electrode, 400 nm/150 nm (Ti / Ag or Al) contacts were evaporated through a shadow mask. The maximum temperature of the substrate during evaporation was 61 °C.

Two probe conductivity measurements were collected using a Keithley Source Meter measurement setup. A homebuilt substrate holder with Au-coated spring pins was used to clamp the substrate and contact the two electrodes. For photoconductivity measurements a handheld 365 nm UV light source was used to irradiate the substrate.

Concluding Remarks

Molecular self-assembly and supramolecular chemistry offer a facile and powerful means of achieving organic-inorganic hybrid materials with long-range nanoscale ordering by mineralization of the inorganic using amphiphilic organic molecules as templates. In this work, electronic function is added to the organic phase by using amphiphiles containing electronically-active aromatic oligomers in the mineralization and growth of inorganic phases of ZnO and silica. When investigating the self-assembly of the organic phase alone, our results demonstrate that for amphiphilic organic semiconductors containing hydrophilic, non-ionic poly(ethylene glycol) (PEG), the amphiphilicity and structural dominance of the PEG can provide critical control over the aggregation and exciton migration of the chromophores. In addition, we demonstrate that electronically active amphiphiles containing either cationic or anionic head groups can be employed to rationally design hybrid nanostructures with long-range periodicities. The hybrid nanostructures generated from the electrodeposition of ZnO, in particular, hold special promise for use in photovoltaics as the dimensions of the nanoscale lamellar domains (3-4 nm) generated meet the spatial demands for efficient exciton splitting and charge transport. Most importantly, the discovery is made in this dissertation that the aromatic segment in the organic phase not only adds a second conductive and electronically active component, but also serves to thermally stabilize the overall nanostructure and convert the mineralized inorganic phase $Zn(OH)_2$ to the desired ZnO. In previous examples in the literature using non-conjugated amphiphiles for electrodeposition of hybrid nanostructures, overall ordering collapsed upon annealing for the necessary conversion of the inorganic phase into ZnO at 150 °C. Consequently, the methodology, described here, can now be applied to a wide variety of

electronic applications in addition to photovoltaics by simply modifying the aromatic conjugated segment of the organic moiety, the identity of the inorganic phase, or both.

REFERENCES AND NOTES

REFERENCES AND NOTES

1. Addadi, L.; Weiner, S., Biomineralization - A pavement of pearl. *Nature* **1997,** 389, (6654), 912-914.

2. Lowenstam, H. A.; Weiner, S., *On Biomineralization*. ed.; Oxford University Press: Oxford, 1989.

3. Gomez-Romero, P.; Sanchez, C., *Functional Hybrid Materials*. ed.; Wiley-VCH: Weinheim, 2004; 1-10.

4. Sharp, K. G., Inorganic/organic hybrid materials. *Adv. Mater.* **1998,** 10, (15), 1243-1248.

5. Beck, J. S.; Vartuli, J. C.; Roth, W. J.; Leonowicz, M. E.; Kresge, C. T.; Schmitt, K. D.; Chu, C. T. W.; Olson, D. H.; Sheppard, E. W.; McCullen, S. B.; Higgins, J. B.; Schlenker, J. L., A New Family of Mesoporous Molecular-Sieves Prepared with Liquid-Crystal Templates. *J. Am. Chem. Soc.* **1992,** 114, (27), 10834-10843.

6. Kresge, C. T.; Leonowicz, M. E.; Roth, W. J.; Vartuli, J. C.; Beck, J. S., Ordered Mesoporous Molecular-Sieves Synthesized by a Liquid-Crystal Template Mechanism. *Nature* **1992,** 359, (6397), 710-712.

7. Sanchez, C.; Lebeau, B.; Chaput, F.; Boilot, J. P., Optical properties of functional hybrid organic-inorganic nanocomposites. *Adv. Mater.* **2003,** 15, (23), 1969-1994.

8. Caseri, W., Nanocomposites of polymers and metals or semiconductors: Historical background and optical properties. *Macromol. Rapid Commun.* **2000,** 21, (11), 705-722.

9. Colvin, V. L.; Schlamp, M. C.; Alivisatos, A. P., Light-Emitting-Diodes Made from Cadmium Selenide Nanocrystals and a Semiconducting Polymer. *Nature* **1994,** 370, (6488), 354-357.

10. Konenkamp, R.; Word, R. C.; Godinez, M., Ultraviolet electroluminescence from ZnO/polymer heterojunction light-emitting diodes. *Nano Lett.* **2005,** 5, (10), 2005-2008.

11. Lee, T. W.; Park, O. O.; Yoon, J. H.; Kim, J. J., Polymer-layered silicate nanocomposite light-emitting devices. *Adv. Mater.* **2001,** 13, (3), 211-213.

12. Coakley, K. M.; McGehee, M. D., Photovoltaic cells made from conjugated polymers infiltrated into mesoporous titania. *Appl. Phys. Lett.* **2003,** 83, (16), 3380-3382.

13. Huynh, W. U.; Dittmer, J. J.; Libby, W. C.; Whiting, G. L.; Alivisatos, A. P., Controlling the morphology of nanocrystal-polymer composites for solar cells. *Adv. Funct. Mater.* **2003,** 13, (1), 73-79.

14. O'Regan, B.; Gratzel, M., A Low-Cost, High-Efficiency Solar-Cell Based on Dye-Sensitized Colloidal Tio2 Films. *Nature* **1991,** 353, (6346), 737-740.

15. Brinker, C. J.; Scherer, G. W., *Sol-Gel Science*. ed.; Academic Press: San Diego, 1990.

16. Avnir, D.; Levy, D.; Reisfeld, R., The Nature of the Silica Cage as Reflected by Spectral Changes and Enhanced Photostability of Trapped Rhodamine-6g. *J. Phys. Chem.* **1984,** 88, (24), 5956-5959.

17. Sanchez, C.; Soler-Illia, G.; Ribot, F.; Lalot, T.; Mayer, C. R.; Cabuil, V., Designed hybrid organic-inorganic nanocomposites from functional nanobuilding blocks. *Chem. Mater.* **2001,** 13, (10), 3061-3083.

18. van Bommel, K. J. C.; Friggeri, A.; Shinkai, S., Organic templates for the generation of inorganic materials. *Angew. Chem., Int. Ed. Engl.* **2003,** 42, (9), 980-999.

19. Whitesides, G. M.; Mathias, J. P.; Seto, C. T., Molecular Self-Assembly and Nanochemistry - a Chemical Strategy for the Synthesis of Nanostructures. *Science* **1991,** 254, (5036), 1312-1319.

20. Whitesides, G. M.; Grzybowski, B., Self-assembly at all scales. *Science* **2002,** 295, (5564), 2418-2421.

21. Kumar, S., *Liquid Crystals: Experimental Study of Physical Properties and Phase Transitions*. ed.; Cambridge University Press: Cambridge, 2001.

22. de Gennes, P. G., *The Physics of liquid Crystals*. ed.; Oxford University Press: New York 1993.

23. Collins, P. J., *Liquid crystals : nature's delicate phase of matter* ed.; Princeton University Press: Princeton, NJ, 2002.

24. Wennerstrom, H., Relation between Micelle Size and Shape and the Stability of Liquid-Crystalline Phases in Surfactant Systems. *J. Colloid Interface Sci.* **1979,** 68, (3), 589-590.

25. Israelachvili, J., *Intermolecular and Surface Forces*. ed.; Elsevier Science: London, 2002.

26. Khetrapal, C. L., *Nuclear Magnetic Resonance Studies in Lyotropic Liquid Crystals*. ed.; Springer-Verlag: New York, 1975; 189.

27. Lehn, J. M., *Supramolecular Chemistry*. ed.; VCH Press: New York, 1995; 234.

28. Vogtle, F., *Supramolecular Chemistry: An Introduction*. ed.; John Wiley & Sons: New York, 1991.

29. Lehn, J. M., Toward self-organization and complex matter. *Science* **2002,** 295, (5564), 2400-2403.

30. Brunsveld, L.; Folmer, B. J. B.; Meijer, E. W.; Sijbesma, R. P., Supramolecular polymers. *Chem. Rev.* **2001,** 101, (12), 4071-4097.

31. Moore, J. S., Supramolecular materials. *MRS Bull.* **2000,** 25, (4), 26-26.

32. Percec, V.; Ahn, C. H.; Ungar, G.; Yeardley, D. J. P.; Moller, M.; Sheiko, S. S., Controlling polymer shape through the self-assembly of dendritic side-groups. *Nature* **1998,** 391, (6663), 161-164.

33. Zimmerman, S. C.; Zeng, F. W.; Reichert, D. E. C.; Kolotuchin, S. V., Self-assembling dendrimers. *Science* **1996,** 271, (5252), 1095-1098.

34. Stupp, S. I.; Pralle, M. U.; Tew, G. N.; Li, L. M.; Sayar, M.; Zubarev, E. R., Self-assembly of organic nano-objects into functional materials. *MRS Bull.* **2000,** 25, (4), 42-48.

35. Kasha, M.; Rawls, H. R.; El-Bayoumi, M. A., The Exciton Model in Molecular Spectroscopy. *Pure Appl. Chem.* **1965,** 11, 371-392.

36. Wasielewski, M. R., Photoinduced Electron-Transfer in Supramolecular Systems for Artificial Photosynthesis. *Chem. Rev.* **1992,** 92, (3), 435-461.

37. Herz, L. M.; Daniel, C.; Silva, C.; Hoeben, F. J. M.; Schenning, A. P. H. J.; Meijer, E. W.; Friend, R. H.; Phillips, R. T., Fast exciton diffusion in chiral stacks of conjugated pphenylenevinylene oligomers. *Phys. Rev. B: Solid State* **2003,** 68, 45203.

38. O'Neill, M.; Kelly, S. M., Liquid Crystals for Charge Transport, Luminescence, and Photonics. . *Adv. Mater.* **2003,** 15, 1135-1146.

39. Kline, R. J.; McGehee, M. D., Morphology and charge transport in conjugated polymer. *Polymer Reviews* **2006,** 46, (1), 27-45.

40. Schmidt-Mende, L.; Fechtenkotter, A.; Mullen, K.; Moons, E.; Friend, R. H.; MacKenzie, J. D., Self-organized discotic liquid crystals for high-efficiency organic photovoltaics. *Science* **2001,** 293, (5532), 1119-1122.

41. Oguma, J.; Dai, X. M.; Akagi, K., Synthesis and Properties of Ferroelectric Liquid Crystalline Poly(p-Phenylene Vinylene) Derivatives. *Mol. Cryst. Liq. Cryst.* **2001,** 365, 1287-1295.

42. Wang, H. B.; Wang, H. H.; Uran, V. S.; Littrell, K. C.; Thiyagarajan, P.; Yu, L. P., Syntheses of Amphiphilic Diblock Copolymers Containing a Conjugated Block and Their Self-Assembling Properties. *J. Am. Chem. Soc.* **2000,** 122, 6855-6861.

43. Zhu, W.; Li, W. J.; Yu, L. P., Investigation of the Liquid Crystalline Isotropic Phase Transition in Oligo(phenylenevinylene) with Alkyl Side Chains. *Macromolecules* **1997,** 30, 6274-6279.

44. Precup-Blaga, F. S.; Schenning, A. P. H. J.; Meijer, E. W., Liquid Crystalline Oligo(p-Phenylene Vinylene)-Terminated Poly(Propylene Imine) Dendrimers. Synthesis and Characterization. . *Macromolecules* **2003,** 36, 565-572.

45. Hulvat, J. F.; Sofos, M.; Tajima, K.; Stupp, S. I., Self-assembly and luminescence of oligo(p-phenylene vinylene) amphiphiles. *J. Am. Chem. Soc.* **2005,** 127, (1), 366-372.

46. Goto, H.; Akagi, K.; Dai, X. M.; Narihiro, H., Synthesis and dielectric property of a ferroelectric liquid crystalline polythiophene derivative. *Ferroelectrics* **2007,** 348, 551-555.

47. McCulloch, I.; Heeney, M.; Bailey, C.; Genevicius, K.; Macdonald, I.; Shkunov, M.; Sparrowe, D.; Tierney, S.; Wagner, R.; Zhang, W. M.; Chabinyc, M. L.; Kline, R. J.; McGehee, M. D.; Toney, M. F., Liquid-crystalline semiconducting polymers with high charge-carrier mobility. *Nat. Mater.* **2006,** 5, (4), 328-333.

48. Liu, P.; Zhang, Y. M.; Feng, G. J.; Hu, J. H.; Zhou, X. P.; Zhao, Q. H.; Xu, Y. H.; Tong, Z.; Deng, W. J., Synthesis and liquid crystal properties of a novel family of oligothiophene derivatives. *Tetrahedron* **2004,** 60, (24), 5259-5264.

49. Schenning, A.; Kilbinger, A. F. M.; Biscarini, F.; Cavallini, M.; Cooper, H. J.; Derrick, P. J.; Feast, W. J.; Lazzaroni, R.; Leclere, P.; McDonell, L. A.; Meijer, E. W.; Meskers, S. C. J., Supramolecular organization of alpha,alpha '-disubstituted sexithiophenes. *J. Am. Chem. Soc.* **2002,** 124, (7), 1269-1275.

50. Liu, P.; Nakano, H.; Shirota, Y., Synthesis and mesogenic properties of a novel family of oligothiophene derivatives. *Liquid Crystals* **2001,** 28, (4), 581-589.

51. Wu, L. H.; Wang, Y. C.; Hsu, C. S., Synthesis and characterization of thiophene-containing liquid crystals. *Liquid Crystals* **2000,** 27, (11), 1503-1513.

52. Mu llen, K.; Wegner, G., *Electronic Materials: The Oligomer Approach*. Weinham: New York, 1998; 360.

53. van Hutten, P. F.; Krasnikov, V. V.; Hadziioannou, G., A Model Oligomer Approach to Light-Emitting Semiconducting Polymers. *Acc. Chem. Res.* **1999,** 32, 257-265.

54. Gill, R. E.; Hilberer, A.; van Hutten, P. G.; Berentschot, G.; Werts, M. P. L.; Meetsma, A.; Wittmann, J.-C.; Hadzioannou, G., Model Compounds for Light-Emitting PPV's: Optical and Structural Data of Substituted Oligomers. . *Synth. Met.* **1997,** 84, 637-638.

55. Leclere, P.; Surin, M.; Viville, P.; Lazzaroni, R.; Kilbinger, A. F. M.; Henze, O.; Feast, W. J.; Cavallini, M.; Biscarini, F.; Schenning, A.; Meijer, E. W., About oligothiophene self-assembly: From aggregation in solution to solid-state nanostructures. *Chem. Mater.* **2004,** 16, (23), 4452-4466.

56. Goodson, T.; Li, W.; Gharavi, A.; Yu, L., Oligophenylenevinylenes for Light-Emitting Diodes. *Adv. Mater.* **1997,** 9, 639-643.

57. Gebhardt, V.; Bacher, A.; Thelakkat, M.; Stalmach, U.; Meier, H.; Schmidt, H.-W.; Haarer, D., Light-Emitting Didoes Based on Phenylenevinylene Oligomers with Defined Chain Lengths. *Synth. Met.* **1997,** 90, 123-126.

58. Geens, W.; Portmans, J.; Jain, S. C.; Nijs, J.; Mertens, R.; Veenstra, S. C.; Krasnikov, V. V.; Hadziioanou, G., Analytical Study of PPV-Oligomer-and-C60 Based Devices for Optimizing Organic Solar Cells. . *Sol. Energy Mater. Sol. Cell* **2000,** 61, 43-51.

59. Messmore, B. W.; Hulvat, J. F.; Sone, E. D.; Stupp, S. I., Synthesis, self-assembly, and characterization of supramolecular polymers from electroactive dendron rodcoil molecules. *J. Am. Chem. Soc.* **2004,** 126, (44), 14452-14458.

60. Sirringhaus, H.; Brown, P. J.; Friend, R. H.; Nielsen, M. M.; Bechgaard, K.; Langeveld-Voss, B. M. W.; Spiering, A. J. H.; Janssen, R. A. J.; Meijer, E. W.; Herwig, P.; de Leeuw, D. M., Two-dimensional charge transport in self-organized, high-mobility conjugated polymers. *Nature* **1999,** 401, (6754), 685-688.

61. Antonietti, M., Surfactants for novel templating applications. *Curr. Opin. Colloid Interface Sci.* **2001,** 6, (3), 244-248.

62. Mann, S.; Ozin, G. A., Synthesis of inorganic materials with complex form. *Nature* **1996,** 382, (6589), 313-318.

63. Stupp, S. I.; Braun, P. V., Molecular manipulation of microstructures: Biomaterials, ceramics, and semiconductors. *Science* **1997,** 277, (5330), 1242-1248.

64. Estroff, L. A.; Hamilton, A. D., At the interface of organic and inorganic chemistry: Bioinspired synthesis of composite materials. *Chem. Mater.* **2001,** 13, (10), 3227-3235.

65. Mann, S.; Burkett, S. L.; Davis, S. A.; Fowler, C. E.; Mendelson, N. H.; Sims, S. D.; Walsh, D.; Whilton, N. T., Sol-gel synthesis of organized matter. *Chem. Mater.* **1997,** 9, (11), 2300-2310.

66. Weiner, S.; Addadi, L., Design strategies in mineralized biological materials. *J. Mat. Chem.* **1997,** 7, (5), 689-702.

67. Mann, S., Molecular Tectonics in Biomineralization and Biomimetic Materials Chemistry. *Nature* **1993,** 365, (6446), 499-505.

68. Braun, P. V.; Osenar, P.; Stupp, S. I., Semiconducting Superlattices Templated by Molecular Assemblies. *Nature* **1996,** 380, 325-328.

69. Braun, P. V.; Osenar, P.; Tohver, V.; Kennedy, S. B.; Stupp, S. I., Nanostructure Templating in Inorganic Solids with Organic Lyotropic Liquid Crystals. *J. Am. Chem. Soc.* **1999,** 121, 7302-7309.

70. Tohver, V.; Braun, P. V.; Pralle, M. U.; Stupp, S. I., Counterion effects in liquid crystal. Templating of nanostructured CdS. *Chem. Mater.* **1997,** 9, (7), 1495-1498.

71. Rabatic, B. M.; Pralle, M. U.; Tew, G. N.; Stupp, S. I., Nanostructured Semiconductors Templated by Cholesteryl-Oligo(Ethylene Oxide) Amphiphiles. *Chem. Mater.* **2003,** 15, 1249-1255.

72. Osenar, P.; Braun, P. V.; Stupp, S. I., Lamellar Semiconductor-Organic Nanostructures from Self-Assembled Templates. . *Adv. Mater.* **1996,** 8, 1022-1025.

73. Sone, E. D.; Zubarev, E. R.; S.I., S., Semiconductor Nanohelices Templated by Supramolecular Ribbons. . *Angew. Chem., Int. Ed. Engl.* **2002,** 41, 1705-1709.

74. Sone, E. D.; Zubarev, E. R.; Stupp, S. I., Supramolecular templating of single and double nanohelices of cadmium sulfide. *Small* **2005,** 1, (7), 694-697.

75. Braun, P. V.; Osenar, P.; Twardowski, M.; Tew, G. N.; Stupp, S. I., Macroscopic nanotemplating of semiconductor films with hydrogen-bonded lyotropic liquid crystals. *Adv. Funct. Mater.* **2005,** 15, (11), 1745-1750.

76. Luo, H. M.; Zhang, J. F.; Yan, Y. S., Electrochemical deposition of mesoporous crystalline oxide semiconductor films from lyotropic liquid crystalline phases. *Chem. Mater.* **2003,** 15, (20), 3769-3773.

77. Attard, G. S.; Bartlett, P. N.; Coleman, N. R. B.; Elliott, J. M.; Owen, J. R.; Wang, J. H., Mesoporous platinum films from lyotropic liquid crystalline phases. *Science* **1997,** 278, (5339), 838-840.

78. Attard, G. S.; Leclerc, S. A. A.; Maniguet, S.; Russell, A. E.; Nandhakumar, I.; Bartlett, P. N., Mesoporous Pt/Ru alloy from the hexagonal lyotropic liquid crystalline phase of a nonionic surfactant. *Chem. Mater.* **2001,** 13, (5), 1444-1446.

79. Luo, H. M.; Sun, L.; Lu, Y. F.; Yan, Y. S., Electrodeposition of mesoporous semimetal and magnetic metal films from lyotropic liquid crystalline phases. *Langmuir* **2004,** 20, (23), 10218-10222.

80. Huo, Q. S.; Margolese, D. I.; Ciesla, U.; Feng, P. Y.; Gier, T. E.; Sieger, P.; Leon, R.; Petroff, P. M.; Schuth, F.; Stucky, G. D., Generalized Synthesis of Periodic Surfactant Inorganic Composite-Materials. *Nature* **1994,** 368, (6469), 317-321.

81. Zhao, D. Y.; Feng, J. L.; Huo, Q. S.; Melosh, N.; Fredrickson, G. H.; Chmelka, B. F.; Stucky, G. D., Triblock copolymer syntheses of mesoporous silica with periodic 50 to 300 angstrom pores. *Science* **1998,** 279, (5350), 548-552.

82. Ogawa, M., A simple set-gel route for the preparation of silica-surfactant mesostructured materials. *Chem. Comm.* **1996**, (10), 1149-1150.

83. Yang, H.; Coombs, N.; Sokolov, I.; Ozin, G. A., Free-standing and oriented mesoporous silica films grown at the air-water interface. *Nature* **1996,** 381, (6583), 589-592.

84. Yang, H.; Kuperman, A.; Coombs, N.; MamicheAfara, S.; Ozin, G. A., Synthesis of oriented films of mesoporous silica on mica. *Nature* **1996,** 379, (6567), 703-705.

85. Nicole, L.; Boissiere, C.; Grosso, D.; Quach, A.; Sanchez, C., Mesostructured hybrid organic-inorganic thin films. *J. Mat. Chem.* **2005,** 15, (35-36), 3598-3627.

86. Brinker, C. J.; Lu, Y. F.; Sellinger, A.; Fan, H. Y., Evaporation-induced self-assembly: Nanostructures made easy. *Adv. Mater.* **1999,** 11, (7), 579-585.

87. Fan, H. Y.; Brinker, J., Evaporation-induced self-assembly to functional nanostructures. In *Mesoporous Crystals and Related Nano-Structured Materials*, 2004; 213-240.

88. Lu, Y. F.; Ganguli, R.; Drewien, C. A.; Anderson, M. T.; Brinker, C. J.; Gong, W. L.; Guo, Y. X.; Soyez, H.; Dunn, B.; Huang, M. H.; Zink, J. I., Continuous formation of supported cubic and hexagonal mesoporous films by sol gel dip-coating. *Nature* **1997,** 389, (6649), 364-368.

89. Choi, K. S.; McFarland, E. W.; Stucky, G. D., Electrocatalytic properties of thin mesoporous platinum films synthesized utilizing potential-controlled surfactant assembly. *Adv. Mater.* **2003,** 15, (23), 2018-2021.

90. Tan, Y. W.; Steinmiller, E. M. P.; Choi, K. S., Electrochemical tailoring of lamellar-structured ZnO films by interfacial surfactant templating. *Langmuir* **2005,** 21, (21), 9618-9624.

91. Hoppe, H.; Sariciftci, N. S., Organic solar cells: An overview. *Journal of Materials Research* **2004,** 19, (7), 1924-1945.

92. Nelson, J., Organic photovoltaic films. *Curr. Opin. Solid State Mater. Sci.* **2002,** 6, (1), 87-95.

93. Brabec, C. J.; Sariciftci, N. S.; Hummelen, J. C., Plastic solar cells. *Adv. Funct. Mater.* **2001,** 11, (1), 15-26.

94. Schweitzer, B.; Bassler, H., Excitons in conjugated polymers. *Synth. Met.* **2000,** 109, (1-3), 1-6.

95. Scholes, G. D.; Rumbles, G., Excitons in nanoscale systems. *Nat. Mater.* **2006,** 5, (9), 683-696.

96. Gregg, B. A., Excitonic solar cells. *J. Phys. Chem. B* **2003,** 107, (20), 4688-4698.

97. Forrest, S. R., The limits to organic photovoltaic cell efficiency. *MRS Bull.* **2005,** 30, (1), 28-32.

98. Bozano, L.; Carter, S. A.; Scott, J. C.; Malliaras, G. G.; Brock, P. J., Temperature- and field-dependent electron and hole mobilities in polymer light-emitting diodes. *Appl. Phys. Lett.* **1999,** 74, (8), 1132-1134.

99. Gratzel, M., Dye-sensitized solid-state heterojunction solar cells. *MRS Bull.* **2005,** 30, (1), 23-27.

100. Huynh, W. U.; Dittmer, J. J.; Alivisatos, A. P., Hybrid nanorod-polymer solar cells. *Science* **2002,** 295, (5564), 2425-2427.

101. Huynh, W. U.; Peng, X. G.; Alivisatos, A. P., CdSe nanocrystal rods/poly(3-hexylthiophene) composite photovoltaic devices. *Adv. Mater.* **1999,** 11, (11), 923-927.

102. Sun, B. Q.; Snaith, H. J.; Dhoot, A. S.; Westenhoff, S.; Greenham, N. C., Vertically segregated hybrid blends for photovoltaic devices with improved efficiency. *J. Appl. Phys.* **2005,** 97, (1).

103. Coakley, K. M.; Liu, Y. X.; McGehee, M. D.; Frindell, K. L.; Stucky, G. D., Infiltrating semiconducting polymers into self-assembled mesoporous titania films for photovoltaic applications. *Adv. Funct. Mater.* **2003,** 13, (4), 301-306.

104. Beek, W. J. E.; Slooff, L. H.; Wienk, M. M.; Kroon, J. M.; Janssen, R. A. J., Hybrid solar cells using a zinc oxide precursor and a conjugated polymer. *Adv. Funct. Mater.* **2005,** 15, (10), 1703-1707.

105. Beek, W. J. E.; Wienk, M. M.; Janssen, R. A. J., Efficient hybrid solar cells from zinc oxide nanoparticles and a conjugated polymer. *Adv. Mater.* **2004,** 16, (12), 1009-1013.

106. Beek, W. J. E.; Wienk, M. M.; Janssen, R. A. J., Hybrid polymer solar cells based on zinc oxide. *J. Mat. Chem.* **2005,** 15, (29), 2985-2988.

107. Beek, W. J. E.; Wienk, M. M.; Kemerink, M.; Yang, X. N.; Janssen, R. A. J., Hybrid zinc oxide conjugated polymer bulk heterojunction solar cells. *J. Phys. Chem. B* **2005,** 109, (19), 9505-9516.

108. Meulenkamp, E. A., Synthesis and growth of ZnO nanoparticles. *J. Phys. Chem. B* **1998,** 102, (29), 5566-5572.

109. Okuya, M.; Nakade, K.; Kaneko, S., Porous TiO2 thin films synthesized by a spray pyrolysis deposition (SPD) technique and their application to dye-sensitized solar cells. *Sol. Energy Mater. Sol. Cells* **2002,** 70, (4), 425-435.

110. Yang, R.; Yang, X. R.; Evans, D. F.; Hendrickson, W. A.; Baker, J., Scanning Tunneling Microscopy Images of Poly(Ethylene Oxide) Polymers - Evidence for Helical and Superhelical Structures. *J. Phys. Chem.* **1990,** 94, (15), 6123-6125.

111. Cullity, B. D.; Stock, S. R., *Elements of X-Ray Diffraction*. Third ed.; Prentice Hall: Upper Saddle River, NJ, 2001; 619.

112. Brinker, C. J., Evaporation-induced self-assembly: Functional nanostructures made easy. *MRS Bull.* **2004,** 29, (9), 631-640.

113. Doshi, D. A.; Gibaud, A.; Goletto, V.; Lu, M. C.; Gerung, H.; Ocko, B.; Han, S. M.; Brinker, C. J., Peering into the self-assembly of surfactant templated thin-film silica mesophases. *J. Am. Chem. Soc.* **2003,** 125, (38), 11646-11655.

114. Gibaud, A.; Grosso, D.; Smarsly, B.; Baptiste, A.; Bardeau, J. F.; Babonneau, F.; Doshi, D. A.; Chen, Z.; Brinker, C. J.; Sanchez, C., Evaporation-controlled self-assembly of silica surfactant mesophases. *J. Phys. Chem. B* **2003,** 107, (25), 6114-6118.

115. Aida, T.; Tajima, K., Photoluminescent silicate microsticks containing aligned nanodomains of conjugated polymers by sol-gel-based in situ polymerization. *Angew. Chem., Int. Ed. Engl.* **2001,** 40, (20), 3803-3806.

116. Ikegame, M.; Tajima, K.; Aida, T., Template synthesis of polypyrrole nanofibers insulated within one-dimensional silicate channels: Hexagonal versus lamellar for recombination of polarons into bipolarons. *Angew. Chem., Int. Ed. Engl.* **2003,** 42, (19), 2154-2157.

117. Lu, Y. F.; Yang, Y.; Sellinger, A.; Lu, M. C.; Huang, J. M.; Fan, H. Y.; Haddad, R.; Lopez, G.; Burns, A. R.; Sasaki, D. Y.; Shelnutt, J.; Brinker, C. J., Self-assembly of mesoscopically ordered chromatic polydiacetylene/silica nanocomposites. *Nature* **2001,** 410, (6831), 913-917.

118. Yang, Y.; Lu, Y. F.; Lu, M. C.; Huang, J. M.; Haddad, R.; Xomeritakis, G.; Liu, N. G.; Malanoski, A. P.; Sturmayr, D.; Fan, H. Y.; Sasaki, D. Y.; Assink, R. A.; Shelnutt, J. A.; van Swol, F.; Lopez, G. P.; Burns, A. R.; Brinker, C. J., Functional nanocomposites prepared by self-assembly and polymerization of diacetylene surfactants and silicic acid. *J. Am. Chem. Soc.* **2003,** 125, (5), 1269-1277.

119. Bhongale, C. J.; Hsu, C. S., Emission enhancement by formation of aggregates in hybrid chromophoric surfactant amphiphile/silica nanocomposites. *Angew. Chem., Int. Ed. Engl.* **2006,** 45, (9), 1404-1408.

120. Tsai, F. Y.; Tu, H. L.; Mou, C. Y., Nonionic fluorescent oligomeric surfactant for ordered mesoporous silica structure. *J. Mat. Chem.* **2006,** 16, (4), 348-350.

121. Wahab, M. A.; Sellinger, A., Photoluminescent surfactants: Mesostructured organosilica nanocomposites via evaporation-induced self assembly (EISA). *Chemistry Letters* **2006,** 35, (11), 1240-1241.

122. Clark, A. P. Z.; Shen, K. F.; Rubin, Y. F.; Tolbert, S. H., An amphiphilic poly(phenylene ethynylene) as the structure-directing agent for periodic nanoscale silica composite materials. *Nano Lett.* **2005,** 5, (9), 1647-1652.

123. Tajima, K.; Li, L.-S.; Stupp, S. I., Nanostructured Oligo(p-phenylene vinylene)/Silicate Hybrid Films: One-Step Fabrication and Energy Transfer Studies. *J. Am. Chem. Soc.* **2006,** 128, 5488-5495.

124. Sun, J. Z.; Sun, J. Q.; Ma, Y. G.; Zhang, X.; Shen, J. C., Blue emitting diodes based on self-assembled multilayers of cationic oligo(p-phenylene vinylene) and sulfonated polyaniline. *Mater. Sci. Eng., C* **1999,** 10, (1-2), 83-86.

125. Locklin, J.; Youk, J. H.; Xia, C. J.; Park, M. K.; Fan, X. W.; Advincula, R. C., Nanostructured ultrathin films of water-soluble sexithiophene bolaform amphiphiles prepared by layer-by-layer self-assembly. *Langmuir* **2002,** 18, (3), 877-883.

126. Xia, C.; Locklin, J.; Youk, J. H.; Fulghum, T.; Advincula, R. C., Distinct aggregation and fluorescence properties of a water-soluble oligothiophene (6TN) bolaform amphiphile. *Langmuir* **2002,** 18, (3), 955-957.

127. Fan, X. W.; Locklin, J.; Youk, J. H.; Blanton, W.; Xia, C. J.; Advincula, R., Nanostructured sexithiophene/clay hybrid mutilayers: A comparative structural and morphological characterization. *Chem. Mater.* **2002,** 14, (5), 2184-2191.

128. Hillhouse, H. W.; van Egmond, J. W.; Tsapatsis, M.; Hanson, J. C.; Larese, J. Z., The interpretation of X-ray diffraction data for the determination of channel orientation in mesoporous films. *Microporous and Mesoporous Mater.* **2001,** 44, 639-643.

129. Grosso, D.; Babonneau, F.; Albouy, P. A.; Amenitsch, H.; Balkenende, A. R.; Brunet-Bruneau, A.; Rivory, J., An in situ study of mesostructured CTAB-silica film formation during dip coating using time-resolved SAXS and interferometry measurements. *Chem. Mater.* **2002,** 14, (2), 931-939.

130. Grosso, D.; Cagnol, F.; Soler-Illia, G.; Crepaldi, E. L.; Amenitsch, H.; Brunet-Bruneau, A.; Bourgeois, A.; Sanchez, C., Fundamentals of mesostructuring through evaporation-induced self-assembly. *Adv. Funct. Mater.* **2004,** 14, (4), 309-322.

131. Doshi, D. A.; Gibaud, A.; Liu, N. G.; Sturmayr, D.; Malanoski, A. P.; Dunphy, D. R.; Chen, H. J.; Narayanan, S.; MacPhee, A.; Wang, J.; Reed, S. T.; Hurd, A. J.; van Swol, F.; Brinker, C. J., In-situ X-ray scattering study of continuous silica-surfactant self-assembly during steady-state dip coating. *J. Phys. Chem. B* **2003,** 107, (31), 7683-7688.

132. Paleos, C. M., Thermotropic Liquid-Crystals Derived from Amphiphilic Mesogens. *Molecular Crystals and Liquid Crystals Science and Technology Section a-Molecular Crystals and Liquid Crystals* **1994,** 243, 159-183.

133. Kiessig, H., *Ann. Phys.* **1931,** 10, 769.

134. Daillant, J.; Gibaud, A., *X-Ray and Neutron Reflectivity: Principles and Applications*. ed.; Springer: Berlin, 1999; 87-120.

135. Tolan, M., *X-Ray Scattering from Soft-Matter Thin Films: Materials Science and Basic Research*. ed.; Springer: Berlin, 1999; 148.

136. Gibaud, A.; Baptiste, A.; Doshi, D. A.; Brinker, C. J.; Yang, L.; Ocko, B., Wall thickness and core radius determination in surfactant templated silica thin films using GISAXS and X-ray reflectivity. *Europhys. Lett.* **2003,** 63, (6), 833-839.

137. Yoshida, T.; Komatsu, D.; Shimokawa, N.; Minoura, H., Mechanism of cathodic electrodeposition of zinc oxide thin films from aqueous zinc nitrate baths. *Thin Solid Films* **2004,** 451-52, 166-169.

138. Yoshida, T.; Minoura, H., Electrochemical self-assembly of dye-modified zinc oxide thin films. *Adv. Mater.* **2000,** 12, (16), 1219-1222.

139. Yoshida, T.; Tochimoto, M.; Schlettwein, D.; Wohrle, D.; Sugiura, T.; Minoura, H., Self-assembly of zinc oxide thin films modified with tetrasulfonated metallophthalocyanines by one-step electrodeposition. *Chem. Mater.* **1999,** 11, (10), 2657-2667.

140. Kagan, J.; Arora, S. K.; Ustunol, A., 2,2'-5',2''-Terthiophene-5-Carboxylic Acid and 2,2'-5',2''-Terthiophene-5,5''-Dicarboxylic Acid. *J. Org. Chem.* **1983,** 48, (22), 4076-4078.

141. Kilbinger, A. F. M.; Schenning, A.; Goldoni, F.; Feast, W. J.; Meijer, E. W., Chiral aggregates of alpha,omega-disubstituted sexithiophenes in protic and aqueous media. *J. Am. Chem. Soc.* **2000,** 122, (8), 1820-1821.

142. Teo, B. K.; Joy, D. C., *EXAFS Spectroscopy: Techniques and Applications*. ed.; Plenum Press: New York, 1981.

143. Han, S. W., X-ray absorption fine structure and nanostructures. *International Journal of Nanotechnology* **2006,** 3, (2-3), 396-413.

144. Choi, K. S.; Lichtenegger, H. C.; Stucky, G. D.; McFarland, E. W., Electrochemical synthesis of nanostructured ZnO films utilizing self-assembly of surfactant molecules at solid-liquid interfaces. *J. Am. Chem. Soc.* **2002,** 124, (42), 12402-12403.

145. Liang, C. H.; Shimizu, Y.; Masuda, M.; Sasaki, T.; Koshizaki, N., Preparation of layered zinc hydroxide/surfactant nanocomposite by pulsed-laser ablation in a liquid medium. *Chem. Mater.* **2004,** 16, (6), 963-965.

146. Beek, W. J. E.; Wienk, M. M.; Janssen, R. A. J., Hybrid solar cells from regioregular polythiophene and ZnO nanoparticles. *Adv. Funct. Mater.* **2006,** 16, (8), 1112-1116.

147. Greene, L. E.; Law, M.; Goldberger, J.; Kim, F.; Johnson, J. C.; Zhang, Y. F.; Saykally, R. J.; Yang, P. D., Low-temperature wafer-scale production of ZnO nanowire arrays. *Angew. Chem., Int. Ed. Engl.* **2003,** 42, (26), 3031-3034.

148. Vayssieres, L., Growth of arrayed nanorods and nanowires of ZnO from aqueous solutions. *Adv. Mater.* **2003,** 15, (5), 464-466.

149. Ogata, S.; Tagaya, H.; Karasu, M.; Kadokawa, J., New preparation method for organic-inorganic layered compounds by organo derivatization reaction of Zn(OH)(2) with carboxylic acids. *J. Mat. Chem.* **2000,** 10, (2), 321-327.

150. Staehlin, W.; Oswald, H. R., Crystal structure of zinc hydroxide nitrate, Zn5(OH)8(NO3)2.2H2O. *Acta Crystallographica, Sec. B: Structural Crystallography and Crystal Chem.* **1970,** 26, (Pt. 6), 860-3.

151. Oswald, H. R.; Asper, R., Bivalent Metal Hydroxides. In *Preparation and Crystal Growth of Materials with Layered Structures*, ed.; Lieth, R. M. A., D. Riedel Publishing Company: 1977; '71-140.

APPENDIX ONE

Synthesis of Oligothiophene Amphiphiles

APPENDIX I. Synthesis of Oligothiophene Amphiphiles

All oligothiophene amphiphiles were synthesized by David Stone of the author's laboratory, according to the following procedures. Unless otherwise noted, all starting materials were obtained from commercial suppliers and used without further purification. ^{1}H NMR and ^{13}C NMR spectra were recorded in a Varian Inova 500 (500 MHz for ^{1}H and 120 MHz for ^{13}C NMR) spectrometer using the solvent proton signal as standard. Mass spectra were obtained on a Micromass Quattro II atmospheric pressure ionization (API) triple quadrupole mass spectrometer. Matrix-assisted laser desorption ionization-time-of-flight mass spectrometry (MALDI-TOF MS) was performed on an Applied Biosystems Voyager-DE Pro.

Appendix I.1. Synthesis of Quinquethiophene-PEG (5T-PEG-24) Amphiphile

2-octadecyl-5-(thiophen-2-yl)thiophene (9).

In a flame dried flask, 2,2'-bithiophene (3.0 g, 18 mmol) was dissolved in anhydrous THF (150 mL) and cooled to 0 °C. n-Butyl Lithium in a 2.5 M solution in cyclochexane (7.2 mL) was added drop wise to the solution. The reaction was stirred for 30 minutes. Then 1-bromooctadecane (7.3 g, 22mmol) in 20 mL dry THF was added drop wise into the reaction mix. The reaction was warmed to room temperature and stirred for 16 hr. The reaction was quenched with water and then extracted 3x with sat. NaCl (aq). The organic layer was dried with Na_2SO_4 and concentrated. The crude product was purified by column chromatography (silica gel; chloroform/hexanes, 10/90) and recrystalied from $CHCl_3$/MeOH to yield 4.19 g (47%) the desired product as a yellow solid. . ^{1}H NMR ($CDCl_3$, ppm): δ 7.18 (d, 1H, *J* = 5.0 Hz), 7.11 (d, 1H, *J* = 3.5 Hz), 7.01-6.99 (m, 2H), 6.68 (d, 1H, *J* = 4.0 Hz), 2.80 (t, 2H, *J* = 8), 1.69 (qn, 2H, *J* = 8 Hz), 1.39-1.23 (m, 30H), 0.90 (t, 3H, *J* = 6.5 Hz).

2-bromo-5-(5-octadecylthiophen-2-yl)thiophene (10).

To a solution of **9** (3.0 g, 6.0 mmol) in DMF (250 mL) was added NBS (1.3 g, 6.6 mmol) was added over 4 hrs at 0 °C. The reaction stirred in the dark for 16 hr while warming to room temperature. To remove the solvent, the reaction was diluted in $CHCl_3$ and extracted 6x with 5% citric acid (aq). The organic layer was dried with Na_2SO_4 and concentrated to yield 3.49 g (92 %) of the desired product. ^{1}H NMR ($CDCl_3$, ppm): δ 6.95 (d, 1H, *J* = 4.0Hz), 6.92 (d, 1H, *J* = 3.0 Hz), 6.84 (d, 1H, *J* = 4.0 Hz), 6.67 (d, 1H, *J* = 3.5 Hz), 2.78 (t, 2H, *J* = 7.5 Hz), 1.68 (qn, 2H, *J* = 8.0 Hz). 1.23-1.38 (m, 30H), 0.90 (t, 3H, *J*= 7 Hz).

2-octadecyl terthiophene (11).

A solution of **10** (2.0 g, 4.0 mmol) and 2-(Tributylstannyl)thiophene (1.5 g, 4.0 mmol) in DMF (50 mL) was sparged with N_2 gas for 20 minutes. Tetrakistriphenylphosphine palladium(0) (50 mg) was added to the solution. After stirring at 100 °C for 16 hours, the reaction was cooled to room temperature. The reaction mix was diluted with chloroform and extracted three times with 5% citric acid (aq). The organic layer was dried over Na_2SO_4 and the solvent was removed in vacuo. The crude product was recrystalized from $CHCl_3$/MeOH to yield 1.32 g (66%) of the desired product as a yellow solid. ^{1}H NMR ($CDCl_3$, ppm): δ 7.22 (d, 1H, *J* = 5.0Hz), 7.17 (d, 1H, *J* = 3.5 Hz), 7.07 (d, 1H, *J* = 4.0 Hz), 7.03 (t, 1H, *J* = 4.5 Hz), 7.01 (d, 1H, *J* = 3.5 Hz), 7.00 (d, 1H, *J* = 4.0 Hz), 6.70 (d, 1H, *J* = 3.5 Hz), 2.80 (t, 2H, *J* = 7.5 Hz), 1.69 (t, 2H, *J* = 7.5 Hz), 1.23-1.39 (m, 30H), 0.90 (t, 3H, *J* = 7.0).

2-octadecyl-5-tributylstannyl terthiophene (12).

A solution of **11** (0.14 g, 0.28 mmol) in THF (40 mL) in a flame dried flask was cooled to -78 °C in a dry ice/acetone bath. To the solution n-butyl Lithium in a 2.5 M solution in cyclochexane (0.14 mL) was added drop wise to the solution. The reaction was stirred for 30 minutes, then Tributyl tin chloride (0.11g, 0.33 mmol) was added. After stirring for 16 hr, the reaction was diluted with hexanes and extracted 3x with sat. NaCl (aq), dried with Na_2SO_4, and concentrated to give the desired product. The product was used in the next step with out purification.

5T-PEG-24 (13).

A solution of **12** (0.22 g, 0.28 mmol) and **8** (0.32 g, 0.23mmol) in DMF (50 mL) was sparged with N_2 gas for 20 minutes. Tetrakistriphenylphosphine palladium(0) (50 mg) was

added to the solution. After stirring at 100 °C for 16 hours, the reaction was cooled to room temperature. The reaction mix was diluted with chloroform and extracted three times with 5% citric acid (aq). The organic layer was dried over Na_2SO_4 and the solvent was removed in vacuo. The crude product was purified by column chromatography (gradient $CHCl_3$ to $CHCl_3$/5% MeOH to yield 0.40 g (80%) of the desired product as a red solid. ^{1}H NMR ($CDCl_3$, ppm): δ 7.73 (d, 1H, *J* = 4.0 Hz), 7.21 (d, 1H, *J* = 4.0 Hz), 7.15 (d, 1H, *J* = 4.0 Hz), 7.16 (ap, 2H, *J* = 4.0 Hz), 7.08 (*J* = 4.0 Hz), 7.02 (d, 1H, *J* = 3.5 Hz), 7.01 (d, 1H, *J* = 3.5 Hz), 6.70 (d, 1H, *J* = 3.5 Hz), 4.46 (t, 2H, *J* = 2 Hz), 3.83 (t, 2H, *J* = 5 Hz), 3.55-3.75 (m, 94H), 3.91 (s, 3H), 2.80 (t, 2H, *J* = 7.5), 1.69 (qt, 2H, *J* = 7.5 hz), 1.22-1.41 (m, 30H), 0.89 (t, 3H, *J* = 7 Hz).

Appendix I.2: Synthesis of Cationic Quaterthiophene Bolaamphiphile

5-Bromo-2-thiophene methanol (5).

5-bromo-2-thiophene carboxaldehyde (7.23 g, 39 mmol) was dissolved in dry THF (100 mL). The solution was cooled to 0ºC. Lithium aluminum hydride in a 1 M solution of THF (12 mL, 12 mmol) was slowly dripped into the solution. The reaction was stirred at 0 °C for 10 min. Water (7 mL), aqueous 2M NaOH (7 mL), and then water (21 mL) was added and allowed to stir for 20 min. during which time a gray precipitate was observed to form. The precipitate was filtered off, and the resulting solution was evaporated, dissolved in dichloromethane, and dried with $MgSO_4$. The solution was evaporated to give 6.63 g (34 mmol, 88% yield) of **5** as a black oil. ^{1}H NMR ($CDCl_3$, ppm): δ 6.90 (d, 1H, J = 3.5 Hz), 6.72 (d, 1H, J = 4.0 Hz), 4.68 (s, 2H), 2.58 (s, 1H). ^{13}C NMR (120 MHz, $CDCl_3$): δ 145.8, 129.8, 125. 9, 112.4, 60.2.

(5-bromothiophen-2-yl)methyl methanesulfonate.

A mixture of compound **5** (3.0 g, 15.5 mmol), triethylamine (2.26g, 23.3 mmol), and methanesulfonyl chloride (2.13 g, 18.6 mmol) in 150 mL of dichloromethane was stirred overnight at room temperature. The solution was extracted twice with HCl (2 M) and once with saturated NaCl. The organic layer was dried with $MgSO_4$, filtered, and concentrated in vacuo to give the product as a brown oil (3.60 g, 85% yield). ^{1}H NMR ($CDCl_3$, ppm): δ 6.92 (d, 1H, J = 4 Hz), 6.85 (d, 1H, J = 4.5 Hz), 4.72 (s, 2H), 3.69 (s, 3H).

2-((5-bromothiophen-2-yl)methoxy)-N,N-dimethylethanamine (6).

In a dry flask, NaH (0.76 g, 31.8 mmol) was added to 100 mL of dry THF. The solution was cooled to 0 °C. 2-(Dimethylamino)ethanol (2.83 g, 31.8 mmol) was added and the mixture was stirred for 30 min. 5-bromothiophen-2-yl)methyl methanesulfonate (3.60 g, 13.3 mmol)

dissolved in 20 mL dry THF was dripped into the solution and let stir at room temperature overnight. The reaction mixture was diluted with dichloromethane and washed three times with 2 M HCl. 4 M NaOH was added to the aqueous layer until a white precipitate was obtained. The aqueous layer was then washed three times with dichloromethane. The combined organic layer was dried with $MgSO_4$, evaporated, and the crude product was purified by column chromatography (silica gel; CH_2Cl_2/MeOH, 85:15) to give **6** (1.00 g, 28% yield) as a black oil. ^{1}H NMR ($CDCl_3$, ppm): δ 6.90 (d, 1H, *J* = 3.5 Hz), 6.73 (d, 1H, *J* = 3.5 Hz), 3.54 (t, 2H, *J* = 5.5 Hz), 2.51 (t, 2H, *J* = 5.5 Hz), 2.26 (s, 6H). ^{13}C NMR (120 MHz, $CDCl_3$): δ 143.2, 129.5, 126.9, 112.6, 67.9, 58.9, 46.0. ACPI-MS *m/z* calculated for $C_9H_{14}BrNOS$, 263.00; found, 263.99 (M^+).

2-(5-(5-5-5-((2-(Dimethylamino)ethoxy)methyl)tetrathiophene)methoxy)-N,N-dimethylethanamine (7).

In a dry flask that was purged with nitrogen, compound **6** (0.77 g, 2.9 mmol), 5,5'-bis(tributylstannyl)-2,2'-bithiophene (0.98 g, 1.3 mmol), tetrakis(triphenylphosphine)palladium (0.0015 g, 0.013 mmol) was dissolved in 10 mL DMF. The mixture was degassed by three freeze-pump-thaw cycles and then heated to 100ºC overnight. The mixture was cooled to room temperature and diluted with dichloromethane. The organic layer was extracted with saturated $NaHCO_3$ three times, dried with $MgSO_4$, and concentrated in vacuo. The crude product was purified by column chromatography (silica gel; CH_2Cl_2/MeOH, 80/20) to give the desired product (0.26 g, 39%) as a red solid. ^{1}H NMR ($CDCl_3$, ppm): δ 7.07 (m, 4H), 7.04 (d, 2H, *J* = 4 Hz), 6.92 (d, 2H, *J* = 3.5 Hz), 4.69 (t, 4H, *J* = 6.0 Hz), 2.56 (t, 4H, *J* = 5.5 Hz), 2.30 (s, 12H). ^{13}C NMR not possible due to poor solubility. MALDI-TOF MS *m/z* calculated for $C_{27}H_{32}N_2O_2S_4$, 533.81; found, 533.89 ($M + H^+$).

Cationic quaterthiophene (8).

Compound **7** (0.1 g 0.19 mmol) was dissolved in 20 mL of dry THF. A 2 M solution of methylbromide in *t*-butyl methyl ether (5 mL, 10 mmol) was added and the mixture was stirred for 1 day to room temperature. During the stirring a yellow-orange suspension was formed. The suspension was filtered to give the desired compound quantitatively as a yellow-orange solid. ^{1}H NMR (DMSO-d_6, ppm): δ 7.32 (d, 2H, J = 3.5 Hz), 7.29 (d, 2H, J = 4.0 Hz), 7.26 (d, 2H, J = 3.5 Hz), 7.09 (d, 2H, J = 4.0 Hz), 4.73 (s, 4H), 3.90 (t, 4H, J = 5.0 Hz), 3.60 (t, 4H, J = 5.0 Hz), 3.13 (s, 18H). ^{13}C NMR (DMSO-d_6, ppm): δ 140.5, 135.9, 136.1, 135.4, 128.9, 126.0, 125.8, 124.6, 67.1, 63.9, 53.7. ESI-MS m/z calculated for $C_{28}H_{38}N_2O_2S_4^{2+}$ 281.09; found, 281.49 (M^{2+}).

Appendix I.3. Synthesis of Quinquethiophene Dicarboxylic Acid (5T-DCA) Bolaamphiphile

3-methyl-2,5-di(thiophen-2-yl)thiophene (1).

In a dry and degassed flask, a solution of 2,5-Dibromo-3-methylthiophene (1.0 g, 4.0 mmol) in DMF (40 mL) was added 2-(Tributylstannyl)thiophene (3.6 g, 9.6 mmol). The solution was sparged with N_2 gas for 20 minutes. Following the N_2 sparge, tetrakistriphenylphosphine palladium(0) (52 mg) was added to the solution. After stirring at 100 °C for 16 hours, the reaction was cooled to room temperature. The reaction mix was diluted with chloroform and extracted three times with 5% citric acid (aq). The organic layer was dried over Na_2SO_4 and the solvent was removed in vacuo. The crude product was purified by column chromatography (silica gel; chloroform/hexanes, 10/90) to yield 0.86 g (88%) of the compound as a yellow oil. ^{1}H NMR ($CDCl_3$, ppm): δ 7.32 (d, 1H, *J* = 5 Hz), 7.23 (d, 1H, *J* = 5 Hz), 7.19-7.18 (m, 2H), 7.10 (at, 1H, *J* = 4 Hz), 7.04 (at, 1H, *J* = 4), 7.00 (s, 1H), 2.40 (s, 3H). ^{13}C NMR ($CDCl_3$, ppm): δ 137.39, 136.59, 134.90, 134.79, 130.29, 128.15, 128.14, 127.76, 125.65, 125.38, 124.63, 123. 84, 15.79.

2,5-bis(5-(tributylstannyl)thiophen-2-yl)-3-methylthiophene (2).

A solution of **1** (0.30 g, 1.1 mmol) in anhydrous THF (30 mL) was cooled to -78 °C. n-Butyl lithium in a 2.5M solution of cyclohexane (1.2 mL) was added and the reaction was stirred for 1hr while warming to room temperature. Tributyltin chloride (0.94 g, 2.9mmol) was added and the reaction stired for 16 hr at room temperature. The reaction was diluted with hexanes and extracted 3x with sat. $NaHCO_3$ (aq), dried with Na_2SO_4, and used without purification in the next step.

tert-butyl 5-bromothiophene-2-carboxylate.

To a solution of DMAP (0.86 g, 7.0 mmol), EDC (1.34, 7.0 mmol), tert-butanol (10 mL, 105 mmol) in dichloromethane (30 mL) was added 5-Bromo-2-thiophenecarboxylic acid (1.0g, 4.8 mmol). After stirring for 16 hr at room temperature, the solvent was removed. The mixture was then dissolved in dichloromethane and extracted 3x with 2M HCl (aq) followed by 3x with sat. $NaHCO_3$. The organic layer was dried with Na_2SO_4 and concentrated to yield 1.16 g (92%) of the desired product as a clear oil. ^{1}H NMR ($CDCl_3$, ppm): δ 7.47 (d, 1H, J = 4 Hz), 7.05 (d, 1H, J = 4 Hz), 1.57 (s, 9H). ^{13}C NMR ($CDCl_3$, ppm): δ 160.62, 137.12, 133.12, 130.92, 119.56, 82.55, 28. 41.

Ditertbutyl ester 3-methyl-quinquethiophene (3).

In a nitrogen atmosphere, tert-butyl 5-bromothiophene-2-carboxylate (0.69 g, 2.6 mmol) was added to a solution of **2** (0.84 g, 1.1mmol) in DMF (40 mL). The solution was sparged with N_2 for 20 minutes and tetrakistriphenylphosphine palladium(0) (57mg) was added. The reaction stirred at 100 °C for 16 hr. The reaction mixture was cooled to room temperature, diluted with chloroform, and extracted 3x with 5% citric acid (aq) to remove the DMF. After drying the organic layer over Na_2SO_4, the product was purified by column chromatography (silica gel; chloroform/hexanes, 65/35) to yield 0.62 g (90%) of the desired product as a red-orange powder. ^{1}H NMR ($CDCl_3$, ppm): δ 7.64 (d, 1H, J = 4 Hz), 7.63 (d, 1H, J = 4 Hz), 7.24 (d, 1H, J = 4 Hz), 7.18 (d, 1H, J = 3.5 Hz), 7.18 (d, 1H, J = 3.5 Hz), 7.14 (d, 1H, J = 3.5 Hz), 7.12 (d, 1H, J = 4 Hz), 7.09 (ad, 2H, J = 4 Hz), 7.01 (s, 1H), 2.43 (s, 3H), 1.61 (s, 18H). ^{13}C NMR ($CDCl_3$, ppm): δ 161.56, 161.54, 143.22, 143.20, 137.41, 136.87, 136.31, 135.64, 135.56, 134.91, 134.00,

133.82, 133.80, 130.42, 128.68, 126.36, 125.98, 125.63, 124.74, 123.94, 123.88, 82.21, 82. 20, 25.50, 16.05.

Dicarboxylic acid 3-methyl-quinquethiophene (5T-DCA) (4).

In a solution 25 mL solution of dichloromethane and TFA (5:1) **3** (50 mg, 0.79 mmol) was stirred at room temperature for 2 hours. The solvent was removed and the product was washed 3x with methanol and dried to yield 37 mg (92%) the desired product as a red solid. ^{1}H NMR ($CDCl_3$, ppm): δ 7.68 (d, 1H, J = 1.5), 7.67 (d, 1H, J = 1.5), 7.52 (d, 1H, J = 3.5), 7.48 (d, 1H, J = 4), 7.41 (d, 1H, J = 4), 7.39 (d, 1H, J = 4), 7.35 (d, 1H, J = 3.5), 7.31 (s, 1H), 7.28 (d, 1H, J = 4), 2.39 (s, 3H).

APPENDIX TWO

X-ray Data Analysis and Fitting

APPENDIX II. X-ray Data Analysis and Fitting

II.1. GIXS Conversion from Reciprocal Space Geometry to Direct Space.

Data files were collected as 2D CCD images in Fit2D, Version: V12.014 (Andy Hammersley, ESRF). The diffraction spot (*x*,*z*) positions are first converted from pixel units to mm units from the direction beam position (*x_dir_beam_pos, z_dir_beam_pos*) and the pixel length of the MAR camera (*pixel_length*) using the equations below derived from Figure II.1.

$$x(mm) = [(x\_dir\_beam\_pos) - (x\_pixel)] * (pixel\_length) \quad \text{(II.1)}$$

$$z(mm) = [(z\_pixel) - (z\_dir\_beam\_pos)] * (pixel\_length) \quad \text{(II.2)}$$

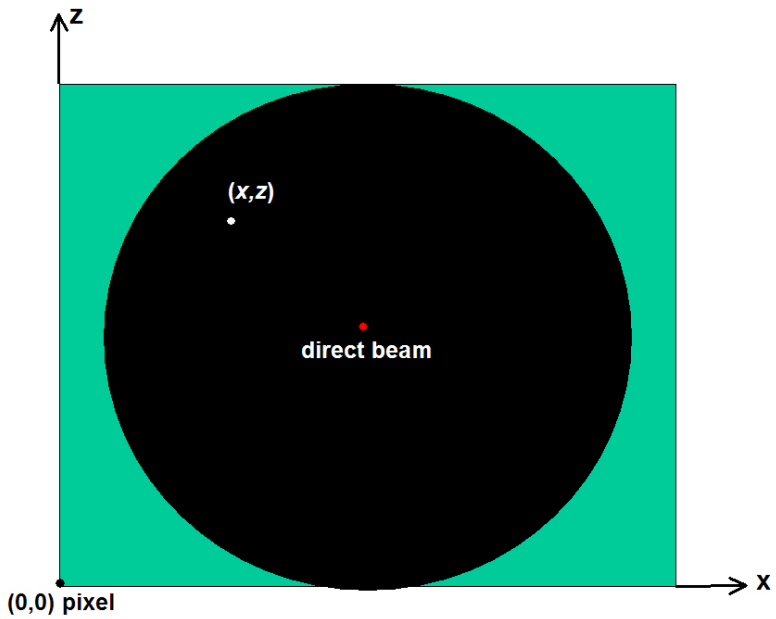

Figure II.1. Schematic of CCD frame of raw data used to convert from pixel distances to mm.

The center of the direct beam is corrected from the theoretical calculation of the AgBe powder standard. The plane of the CCD image is perpendicular to **y** and a distance *D* downstream from the sample/diffractometer. The incidence beam intersects at *x*=0, *y*=0. To convert from

reciprocal space to direct space, the scattering vectors Q_H and Q_v are calculated from the (x,z) position obtained. The equations below are derived from Figure II.2, which shows the left-hand quadrant of the CCD images. The same conversion is used for the right-hand quadrant where the position x is positive instead of negative.

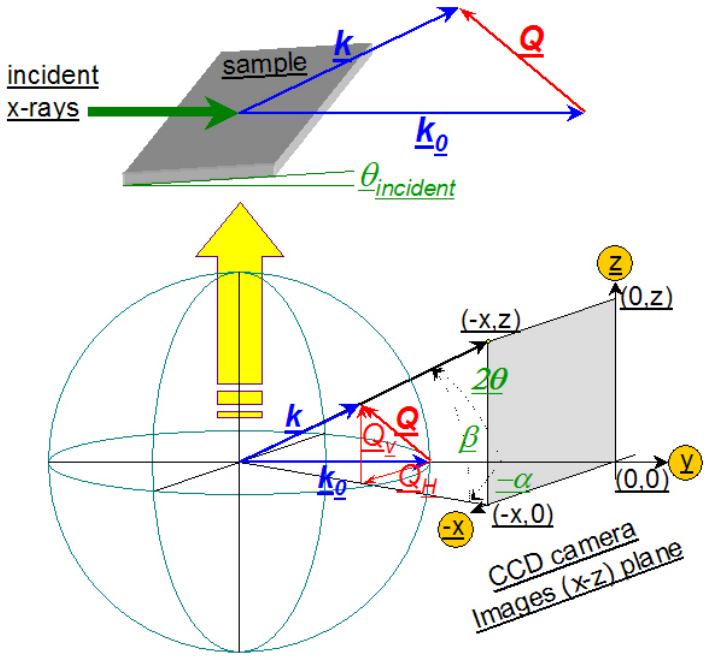

Figure II.2. Schematic of scattering vectors obtained from experimental set-up in reference to left-hand quadrant of CCD image.

$$Q_V(\text{Å}^{-1}) = 2\pi/\lambda \sin\beta \tag{II.2}$$

$$Q_H(\text{Å}^{-1}) = 2\pi/\lambda\left[2(1-\cos\alpha\cos\beta)-\sin^2\beta\right]^{1/2} \tag{II.3}$$

Q_H is composed of the vectors Q_{H_x} and Q_{H_y}, which are defined as:

$$Q_{H\_x}(\text{Å}^{-1}) = 2\pi/\lambda \sin\alpha\cos\beta \tag{II.4}$$

$$Q_{H\_y}(\text{Å}^{-1}) = -2\pi/\lambda [1 - \cos\alpha\cos\beta] \tag{II.5}$$

The angles α (incident) and β (exit) in radians are defined as:

$$\alpha(rad) = \tan^{-1}\left(x/D\right) \tag{II.6}$$

$$\beta(rad) = \tan^{-1}\left(z/\sqrt{x^2 + z^2}\right) \tag{II.7}$$

The *d*-spacings are finally calculated from the values of 2θ in degrees, obtained by:

$$2\theta(deg) = \cos^{-1}\left(\frac{D}{\sqrt{D^2 + x^2 + z^2}}\right) = \cos^{-1}(\cos\alpha\cos\beta) \tag{II.8}$$

$$d(\text{Å}) = \lambda/2\sin\theta \tag{II.9}$$

In the CCD images reported in Chapter 3, Q_H is labeled as the q_x axis and Q_v is labeled as the q_z axis.

II.2. Specular X-Ray Reflectivity Analysis and Fitting.

II.2.1 Specular X-ray Reflectivity Normalization

Specular XRR data are plotted as Log(R/R_F) vs. q_z(Å^{-1}).

$$R(q) = I(q)/I_o \tag{II.10}$$

where $I(q)$ = the total reflected intensity; I_o = the total incident beam intensity; and R_F = ideal Fresnel reflectivity for glass assuming constant electron density and no surface roughness.

$$q_z(\text{Å}^{-1}) = \sqrt{q^2 - q_{fc}^2} \tag{II.10}$$

$$q(\text{Å}^{-1}) = \frac{4\pi \sin\alpha}{\lambda} \tag{II.11}$$

Definitions: q= scalar momentum transfer vector; α = incident beam angle; $q_{fc} = 0.0275$ Å^{-1} is for the film refraction correction for the OPV; and λ is the energy wavelength.

$$q_c(\text{Å}^{-1}) = \frac{4\pi \sin\alpha_c}{\lambda} \tag{II.12}$$

$$Q = \frac{q}{q_c} = \frac{\alpha_i}{\alpha_c} \tag{II.13}$$

Definitions: $q_c = 0.032$ Å^{-1} for the Fresnel reflectivity for ideal float glass; $\alpha_c \approx \sqrt{2\delta}$.

where δ is the dispersion constant and β is the absorption constant of the refractive index.

$$n = 1 - \frac{\lambda^2}{2\pi} r_e \rho + i \frac{\lambda}{4\pi} \mu = 1 - \delta + i\beta \tag{II.14}$$

using glass substrates, $\beta/\delta = 0.0013$ for $\lambda = 1.54$ Å, and $\beta/\delta = 0.0058$ for $\lambda = 1.00$ Å.

$$R_F = \frac{\left(\alpha_i - p_+\right)^2 + p_-^2}{\left(\alpha_i + p_+\right)^2 + p_-^2} = \frac{\left[\left(Q - p_+ / \alpha_c\right)^2 + p_-^2 / \alpha_c^2\right]}{\left[\left(Q + p_+ / \alpha_c\right)^2 + p_-^2 / \alpha_c^2\right]} \tag{II.15}$$

$$\begin{aligned} p_+^2 &= \frac{1}{2}\left\{\sqrt{\left(\alpha_i^2 - \alpha_c^2\right)^2 + 4\beta^2} + \left(\alpha_i^2 - \alpha_c^2\right)\right\} \\ &= \frac{1}{2}a_c^2\left\{\sqrt{\left(Q^2 - 1\right)^2 + \left(\beta / \delta\right)^2} + \left(Q^2 - 1\right)\right\} \end{aligned} \tag{II.16}$$

$$\begin{aligned} p_-^2 &= \frac{1}{2}\left\{\sqrt{\left(\alpha_i^2 - \alpha_c^2\right)^2 + 4\beta^2} - \left(\alpha_i^2 - \alpha_c^2\right)\right\} \\ &= \frac{1}{2}a_c^2\left\{\sqrt{\left(Q^2 - 1\right)^2 + \left(\beta / \delta\right)^2} - \left(Q^2 - 1\right)\right\} \end{aligned} \tag{II.17}$$

The equations above were derived from the literature.[135]

II.2.2 Patterson Map

The patterson maps were obtained by using the following code in Matlab 7.1 (Mathworks, Inc.). A gaussian function was first used to extend the data of R/R_F to q_z(Å^{-1}) = 2, and then R/R_F was inputted as an ascii file in column form.

```
function patterson
R_N = load('filename.m', '-ascii');
% line(R_N(:,1),R_N(:,2),...
```

```
% 'LineStyle','none','color','r','Marker','o',...
% 'MarkerFaceColor','none','MarkerSize',6);
% set(gca, 'Yscale', 'log')
R_N_Y=R_N(:, 2);
FTR_N = ifft(R_N_Y);
Abs = FTR_N.* conj(FTR_N);
plot(Abs,'color','b','LineWidth',2)
%plot(real(FTR_N),'color','b','LineWidth',2)
ylabel('FFT','FontSize',12,'FontWeight','bold');
xlabel('Z','FontSize',12,'FontWeight','bold');
set(gca, 'Yscale', 'log')
save('FFT_filename', 'Abs', '-ascii')
```

VITA

Marina Sofos was born on July 19, 1980 in Minneapolis, Minnesota to Dr. John N. and Helen Sofos. Marina, who grew up in Fort Collins, Colorado, is the older sister of Elvera Sofos. She attended Fort Collins High School where she was Valedictorian of her graduating class in 1998. In the fall of 1998, Marina enrolled at Brown University in Providence, Rhode Island and pursued a course of study in Materials Engineering. While at Brown, she conducted undergraduate research in the laboratories of Prof. Clyde Briant and Prof. Eric Chason. She also performed research as part of NSF-sponsored REU programs at the IBM-Almaden Research Center under the guidance of Prof. Kenneth Carter in the summer of 2000 and at Stanford University under the guidance of Prof. Bruce Clemens in the summer of 2001. Upon completion of her Bachelor of Science degree from Brown in May of 2002, Marina began her graduate work at Northwestern University in Evanston, Illinois in the fall of 2002. She joined the research group of Prof. Samuel I. Stupp, where her doctoral thesis research focused on the self-assembly and mineralization of hybrid nanostructures using organic semiconducting amphiphiles, resulting in several publications and presentations at national meetings.